Title	Defect Control for Low Thermal Conductivity in Oxide Materials
Author(s)	Ok, Kyungmin
Citation	大阪大学, 2018, 博士論文
Version Type	VoR
URL	https://doi.org/10.18910/69595
rights	
Note	

Doctoral Dissertation

Defect Control for Low Thermal Conductivity in Oxide Materials

KYUNGMIN OK

January 2018

Division of Sustainable Energy and Environmental Engineering
Graduate School of Engineering
Osaka University

Abstract

Reduction of thermal conductivity has enabled significant advances in a wide variety of fields including thermal/environmental barrier coatings, thermoelectric, and refractory materials because low thermal conductivity is a primary issue in the improvement of efficiency in those applications. Utilized in many of these applications are a class of materials known as semiconductor and insulator. In these materials, thermal conductivity is mainly dominated by phonons (or lattice vibrations). Phonons-dominated thermal conductivity can be controlled by phonon scattering process. Alloying has been generally considered as phonon scattering sources in reducing thermal conductivity. The purpose of this study is to reduce thermal conductivity. Further reduction in thermal conductivity was studied by various scattering such as anharmonicity, vacancies, and ordering vacancies.

In the first chapter, I introduce the theoretical background of thermal transport together with the most important theoretical concepts used throughout this thesis.

The second chapter summarizes the experimental methods used to prepare and characterize the material investigated in this thesis. The first section describes the sintering techniques, namely solid state sintering and spark plasma sintering. In the second section, the measurement techniques applied to study the material properties are discussed.

In the third chapter, thermophysical properties of barium and bismuth doped lanthanum molybdate ($La_2Mo_2O_9$) were investigated. The first section introduced $La_2Mo_2O_9$ compound and provide thermal properties. In second section, thermophysical properties of Ba-doped $La_2Mo_2O_9$ was systematically evaluated and analyzed using empirical thermal conductivity model based on Klemens-Callaway model. The effect of Ba substitution on thermal properties was discussed focusing on vacancies. The thermal conductivity decreased by 9% with the Ba content, as compared to $La_2Mo_2O_9$. The third section evaluated and analyzed about thermophysical properties of Bi-doped $La_2Mo_2O_9$ by empirical thermal conductivity model. The effect of Bi substitution on thermal properties was discussed focusing on changes in lattice anharmonicity induced by lone pair electrons. The thermal conductivity decreased by 34% with respect to non-doped $La_2Mo_2O_9$.

In the fourth chapter, the correlation between the thermal conductivity and the defect type in TiO_{2-x} including point (randomly distributed oxygen vacancies) and planar defects (ordered oxygen vacancies) was studied as a function of the O/Ti ratio. Two series of the TiO_{2-x} samples having point or planar defects were prepared by different heat treatment procedures. The effects produced by the presence of point and planar defects on the properties of non-stoichiometric TiO_{2-x} was investigated. The thermal conductivity of TiO_{2-x} with planar defects was approximately 22% lower than TiO_{2-x} with point defects.

In summary, the effect of various scattering mechanisms (e.g., anharmonicity, oxygen vacancies (random or ordered)) on thermal conductivity was compared by frequency dependent relaxation time. The average reduction in thermal conductivity of each effect was calculated as compared to $La_2Mo_2O_9$. The effect of randomly distributed and ordered oxygen vacancies and enhancing the anharmonicity was 27-34% larger than alloying effect.

The results in each of the studies discussed will provide valuable insight into the role of reduction of thermal conductivity in their respective applications and can apply to environmental/thermal barrier coating, thermoelectric, and refractory designs for the development of high-performance materials.

TABLE OF CONTENTS

CHAPTER Page

I. Introduction

II. Experimental Methods

III. Effect of Ba Substitution on Thermophysical Properties Lanthanum Molybdate

IV. Effect of Bi Substitution on Thermophysical Properties Lanthanum Molybdate

IV. Effect of Oxygen Vacancy Arrangement on Thermophysical Properties TiO$_{2-x}$

CHAPTER I

Introduction

1.1 Background and Motivation

Recent years, the CO_x and NO_x pollution produced by fossil fuel combustion and global warming has been the focal point of discussion. Meanwhile, particular matter and hazardous gas emissions from transportation stationary power plants, vehicles, and heating and cooling systems are largely responsible for the unhealthy air quality of many mega cities. These grand challenges of the global society have to be addressed by aggressively pursuing both cleaner fossil fuel utilization technologies and a paradigm shift to renewable sources of energy such as solar and wind, clean transportation approaches including electric vehicles, and efficient energy utilization technologies. Since over 90% of the global energy use relies on thermal processes, one important objective of our current and future research efforts is to discover and invent materials, devices, and systems for sustainable thermal energy utilization, in order to make broad societal impacts in several technological areas including: Energy efficiency and thermal management of electronic devices, recovery of waste heat, which amounts to over 60% of fuel energy consumption of transportation vehicles and between 20 to 50% of industrial energy input; Efficient heating and cooling of vehicles and buildings, which consumes as much as 20% energy supply; Concentrated solar thermal power, which is receiving renewed interest because thermal energy storage is employed to address the intermittency of solar flux [1]. In recent years, about 95% of the energy humanity used involved processes of conversion of thermal energy. Developing materials with minimal thermal conductivity can improve conversion of energy because it allows the development of high performance refractory, thermoelectric conversion material, and environmental/thermal barrier coating materials such as those that insulate cylinder walls or turbine blades from the combustion gases in internal engine for combustion.

1.2 Application Field

1.2.1. Environmental/Thermal Barrier Coating Materials

Environmental barrier coating materials (EBCs) have been developed to protect ceramic components in engines of gas turbine for higher temperature environmental attack [2]. Advanced EBC systems should be designed for both environmental and thermal protections of the engine component parts in combustion environment of gas turbine. This is because that with increasing demands for considerably fuel efficiency, better engine reliability, and higher operating engine temperature. Especially, functions of thermal barrier for environmental barrier coatings become an important for reducing the rates of chemical reaction and thermal loads of engine component, thus maintaining required durability of those components and mechanical properties (see Fig. 1.1). The development of advanced environmental and thermal barrier coatings may directly affect the succeed use of various ceramic material components in next generation engine systems.

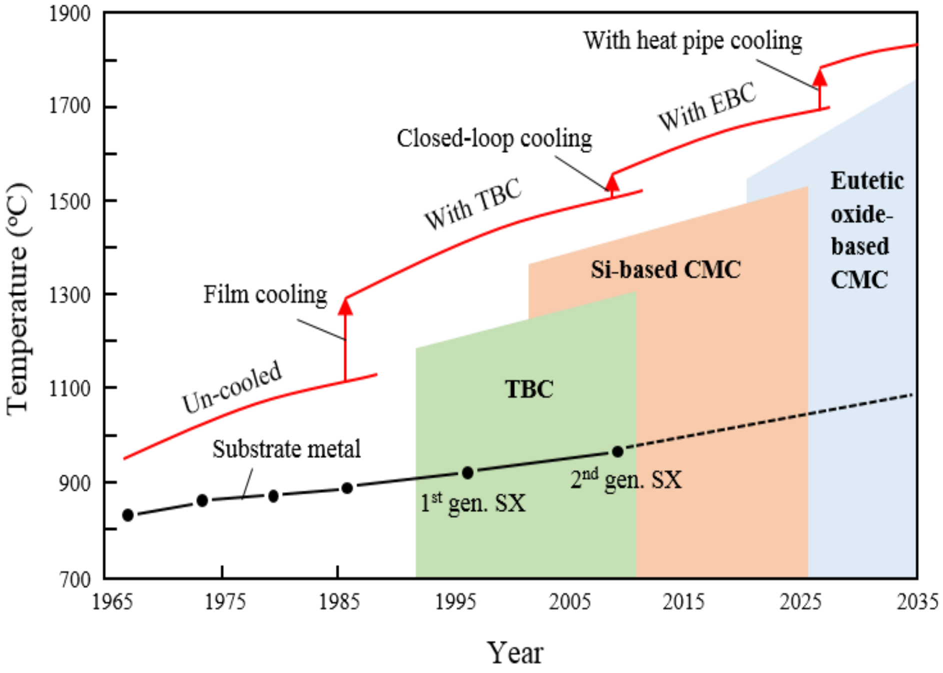

Figure 1.1 The evolution of EBC/TBC for substrate metallic components [3].

Gas turbine engines used to aircraft propel and to produce electricity. They are brayton engines where core power and efficiency are closely associated with the gas temperature entering the section of turbine (see Fig. 1.2 (a)). Additional improvement of the efficiency in energy for turbine engines will rely on additinoal improvements in thermal barrier coatings. At the same moment, since inlet gas temperatures are increased in the seeking higher efficiency of engine, there are new challenges to established thermal barrier coatings. The process of thermodynamic used in gas turbines engine is the Brayton cycle, changed in carnot cycle (see Fig. 1.2 (b)). Two significant factors for performance are the operating temperature and pressure ratio in turbine. The fuel-to-power engine efficiency is optimized by increasing the discrepancy between the pressure of air inlet and compressor discharge. The design determines compression ratio. The efficiency (η) of gas turbine engine can be expressed by

$$\eta = \frac{W}{Q_h} = 1 - \frac{T_c}{T_h} \tag{1.1}$$

where W is the work in system, Q_h is the heat put into the system, T_c is the cold reservoir temperature, and T_h is the hot reservoir temperature (operating tempeature). The temperature at which the operating temperature for turbine affects efficiency with higher temperatures resulting in higher efficiency. Thus, turbine engine with low thermal conductivity can be contributed to increase operating temperature. However, turbine inlet temperature is restricted by the heat condition that can be tolerated by metallic alloy turbine blade. Since the efficiency is improved with increasing the engine working temperature to a level at which the temperature of the uncoated metallic substrate is same as the temperature of the coated metallic substrate (see Fig. 1.2 (c)). The selection of the new thermal barrier coatings materials is satisfied with some requirements such as phase stability between room temperature and working temperature, excellent resistance to sintering at high temperatures, and low thermal conductivity. That is, there is significant interest in developing thermal barrier coatings with low thermal conductivity to provide additional improvements in performance of engine (see Fig. 1.3). Inlet gas temperatures at the turbine could be 1473 to 1673K, but some researcher have beyond turbine inlet temperatures as high as 1873K. Thus it can be protect metallurgical components from thermal damage by engineering blade coatings and cooling systems.

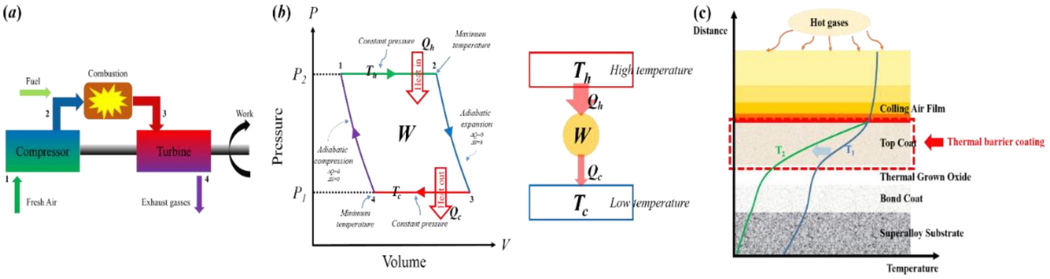

Figure 1.2 Schematic illustration of (a) a Brayton cycle, (b) P-V diagram, and (c) thermal barrier coating system.

Many factors of engineering design impact on the overall gas-turbine engines efficiency, but a key point in improving temperature of engine and efficiency of engine is the introduction of thermal barrier coatings. Thermal barrier coatings offer thermal insulation to the engine parts of superalloy/metallic component. The TBCs material in commercial use is typically made of 7~8wt% yttria stabilized zirconia (7~8YSZ) ceramics having thermal conductivity (2.0 $Wm^{-1}K^{-1}$ at 973 K) [4]. However, approximately 1473 K is regarded as the upper limit of the service temperature for a conventional YSZ thermal barrier coating because of the occurrence of a phase transformation. It is necessary to develop new thermal barrier coating materials replacing the present YSZ to further increase operating temperature in gas engine turbine. Higher operating temperatures can be realized by using TBCs with lower thermal conductivity. And to do that, we need to look for ways to reduce thermal conductivity.

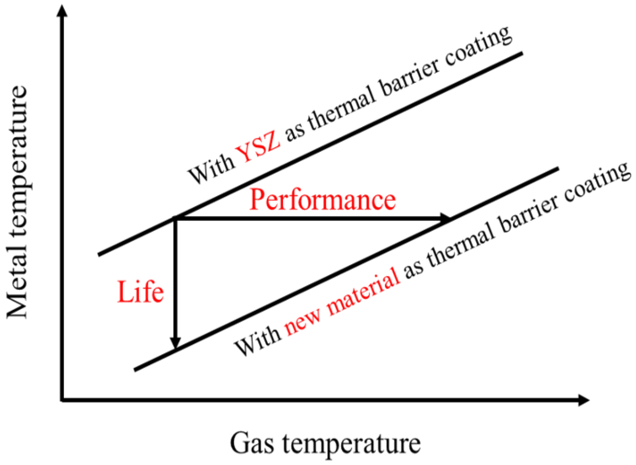

Figure 1.3 Schematic illustration of advantage TBCs as a function of gas temperature.

1.2.2. Thermoelectric Conversion Materials

CIA world facebook has been reported that if we conduct consumption the mineral and fossil fuels without any generate for additional population at present, the world is gradually running short of oil by 2051, and is gradually running short of gas and coal in 2059 and 2087 years, respectively [5]. Thus, we have to establish a long term strategy for the future. It is necessary to developing renewable energy sources and various technologies for energy transformation to replace an exhaustion of natural resources. Besides, a safe and renewable energy development receives attention as major issue in the world. A powerful energy source, nuclear energy faced a risk because the fuel rod meltdown of nuclear power plant induced by the tsunami in Japan. One of the alternative candidate for solving problems of energy is technology of thermoelectric (TE) energy conversion, which is able to transfer thermal directly into electricity by materials known as thermoelectric materials. Automotive exhaust, industrial processes, and home heating generate large amount of thermal waste that would be transfer to electricity using TE materials. Also, the technology of thermoelectric conversion is capable of acting as heat pumps or refrigerators which are not noisy, scalable, and reliable, leading to them for distributed and small power generation. For instances, currently used applications under study are harvesting a waste of thermal energy from the car exhaust. Other promising applications are used for improving the efficiency of thermoelectric property to defense combustion by wood stoves used in least developed among developing countries, reducing smoke output and decreasing large amount of wood necessary to cooking. Also thermoelectric can produce power from the sun through solar power to produce a different temperatures through material; known as conversion of sun's thermal energy. Even though thermoelectric transformation has such a good potential to apply in application extensively, devices of thermoelectric are not commonly used due to lower efficiency of conversion and economic.

The efficiency of the energy conversion is evaluated with a TE figure of merit *ZT*, which is defined by [6]

$$\eta = \left(\frac{T_H - T_C}{T_H}\right)\left[\frac{\sqrt{1+ZT}-1}{\sqrt{1+ZT}+(T_C/T_H)}\right] \tag{1.2}$$

$$ZT = \frac{S^2\sigma}{\kappa}T \tag{1.3}$$

where S, σ, and κ are the Seebeck coefficient, electrical conductivity, and thermal conductivity, respectively. $S^2\sigma$ is called the power factor. The product of figure of merit *ZT* is applied to estimate the performance of thermoelectric materials. A large Seebeck coefficient, lower thermal conductivity and higher electrical conductivity are required for a material with a higher ZT. However, relationship between these factors, the tradeoff correlation between the electrical conductivity and Seebeck coefficient, makes the hard to enhance the power factor. Thus control of thermal conductivity of materials is convenient and important to reach the maximization of the figure of merit.

1.2.3. Refractory Materials

Growing demand for structural ceramics for high temperature application with lower thermal conductivity for various fields of applications for heat insulation such as refractory materials. The usefulness of correct data in regard to the thermal conduction of those materials, which are used in the construction of building or metallurgical and industrial furnaces, is quite generally recognized. Insulating materials is used in process of manufacture to suppress thermal loss or thermal gain.

Heat insulation provides the many benefits: 1) provides fire protection and absorption vibration to equipment, 2) reduces over-all energy consumption, 3) prevents corrosion by keeping the exposed surface of a refrigerated system above dew point, 4) supply better process control by maintaining temperature in process. Thus, control of thermal conductivity of material is important to achieve the materials for more effectively contained within a furnace or kiln.

Refractories materials are able to design for use in furnaces and kilns. The refractory materials are as a major hot face of refractory lining in furnaces and kilns or in other areas needing insulation for high temperature. Also they are able to be used as secondary back-up insulation behind other hot face refractory linings. Refractory is a blend of high grade of refractory cements and aggregates, resulting in an exceptional castable product. The efficiency (η) of the furnace is evaluated with heat losses (Q_c) as following:

$$\eta = \frac{1-Q_c}{Q_c} \tag{1.4}$$

The properties of low thermal conductivity of insulating firebricks with refractory will allow to benefit from further reduction of energy usage such as heat losses and hence improved efficiencies of manufacturing as shown in Fig. 1.4.

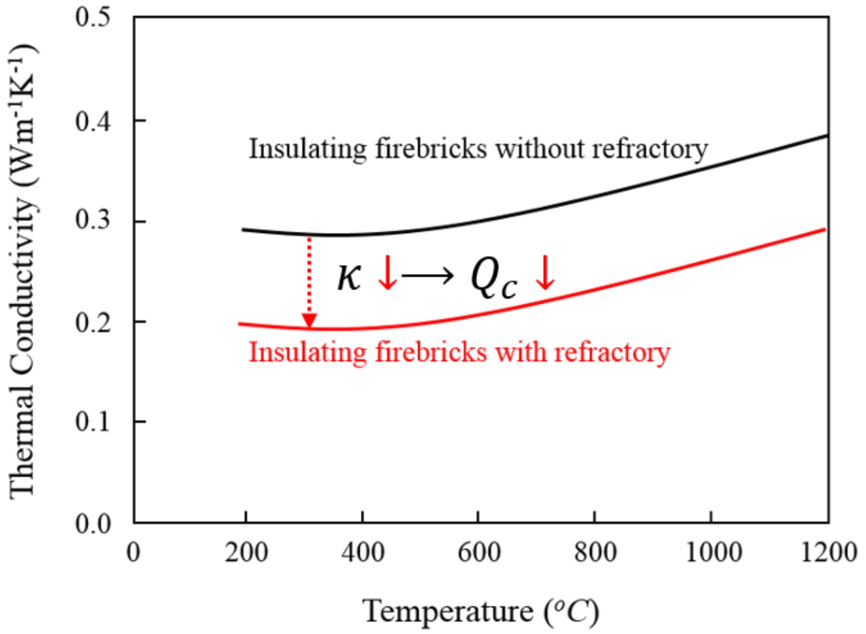

Figure 1.4 Thermal conductivity of insulating firebricks with or without refractory [7].

The low thermal conductivity of thermal insulation products such as refractory materials thus offer the complete solution to enable ceramic manufacturers and kiln builders to maximize thermal efficiencies and performance within kilns.

1.3 Thermal Conductivity in Solid Materials

Phonon scattering mechanism can be characterized by a relaxation time. Theoretical approaches to thermal transport include the mode-dependent thermal conductivity model which focuses on the contributions from each phonon mode along the respective directions and Boltzmann transport equation based model with relaxation time approximation. The empirical thermal conductivity model represents the phonon scattering processes by frequency dependent relaxation times with the Debye phonon spectrum and several other assumptions. This model can capture the heat transport in solid materials.

Assuming that all phonon-scattering processes can be represented by frequency-dependent relaxation times, the lattice thermal conductivity was expressed by the following equation [8]:

$$\kappa_l = \frac{k_B}{2\pi^2 v_B}\int_0^{k_B\theta_D/\hbar} \tau_{total}\left(\frac{\hbar\omega}{k_B T}\right)^2 \frac{exp(\hbar\omega/k_B T)}{[exp(\hbar\omega/k_B T)-1]^2}\,\omega^2 d\omega \qquad (1.5)$$

where $\hbar$ is the Planck constant divided by 2π, ω is the phonon frequency, v_B is the phonon velocity, θ_D is the Debye temperature, and τ_{total} is the total phonon-scattering relaxation time. Under this formulation, the phonon lifetimes corresponding to different scattering mechanisms can be given as a function of phonon frequency. If there are various scattering processes, the contribution of the each can be added together by Matthiessen rule such that:

$$\tau_{total}^{-1} = \sum_i \tau_i^{-1} = \tau_U^{-1} + \tau_B^{-1} + \tau_P^{-1} + \cdots \qquad (1.6)$$

The scattering processes mostly affected by contributions from phonon-phonon Umklapp (anharmonic) scattering (τ_U), phonon-boundary scattering (τ_B), and phonon-point defect scattering (τ_P) in bulk crystalline solid. Generally, the various scattering mechanisms i depend on both phonon frequency and temperature. Figure 1.5 shows the general features of the lattice thermal conductivity as a function of temperature in crystalline solids. There are four temperature regions. In region I and II, the thermal conductivity is mainly determined by the grain size, physical size, and dislocation spacing. The thermal conductivity increases in proportion to ~T^3 with a rise in temperature up to peaks and then decreases. Above the peak (region III), the thermal conductivity decreases in proportion to T^{-1} due to anharmonic scattering, which is the phonon-phonon Umklapp process. In region II and III, the thermal conductivity depends sensitively on the concentration of defects. In region IV, the thermal conductivity plateaus out and has temperature independent behavior. Also, thermal conductivity can be increased by radiative heat transport in this region.

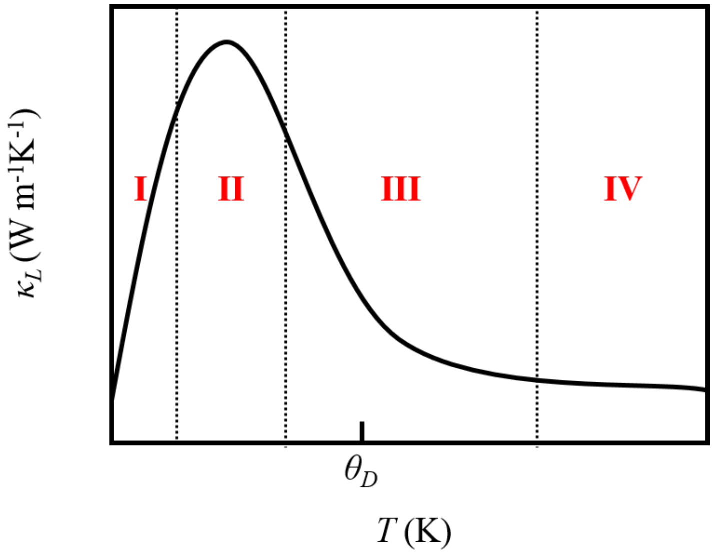

Figure 1.5 The temperature dependent lattice thermal conductivity of single crystal germanium [9].

1.4 Phonon Scattering Mechanisms

1.4.1 Phonon-Phonon Scattering

When phonons are scattered by interacting with other phonons, inelastic phonon scattering event is occurred. This scattering event is induced by anharmonicity in the interatomic forces. The anharmonicity is a consequence of deforming spring (bond) between two atoms exceed its range of elastic, which cause to change in the stiffness. Since phonons involve atomic displacements, when phonon travels, following phenomenon can be happened: the lattice is distorted and the spring (stiffness) is changed. Thus, the phonon may scatter because one phonon encounters a different spring constant.

The inelastic phonon scattering process can be classified as Normal process and Umklapp process. Figure 1.6 shows the scattering processes of two incoming phonons with wave-vector $\overrightarrow{k_1}$ and $\overrightarrow{k_2}$ creating one outgoing phonon with a wave-vector $\overrightarrow{k_3}$. In Normal scattering process, the phonon momentum is conserved because $\overrightarrow{k_3}$, which is the sum of the $\overrightarrow{k_1}$ and $\overrightarrow{k_2}$ stay inside the first Brillouin zone, $K=\pi/a$ (grey squares) where a is the spacing between atoms in Fig. 1.6 (left). As phonon momentum increases, larger wave-vector $\overrightarrow{k_1}$ and $\overrightarrow{k_2}$ might be exceed the maximum limit of the first Brillouin zone. This is because that it is impossible to produce a phonon with a vector greater than π/a because the wavelength of a crystal cannot be smaller than $2a$. So, when the sum of the the $\overrightarrow{k_1}$ and $\overrightarrow{k_2}$ is greater than the first Brillouin zone ($K=\pi/a$), addition of a reciprocal lattice vector $\vec{G}$ must be added as shown in Fig. 1.6 (right). In these processes, known as Umklapp process, the phonon momentum is not conserved. The Umklapp scattering process is dominant for thermal resistivity at high temperatures for low defect crystals. The thermal conductivity for an electrical insulating crystal where the Umklapp processes are dominant has T^{-1} dependence.

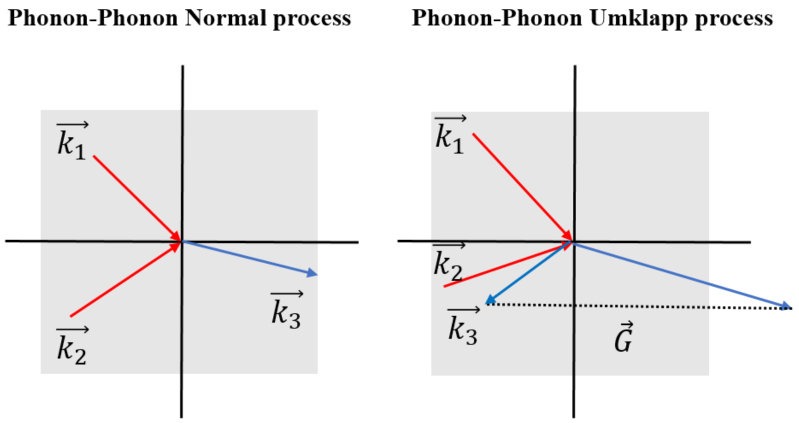

Phonon-Phonon Normal process **Phonon-Phonon Umklapp process**

Figure 1.6 Schematic illustration of possible phonon-phonon scattering processes.

The phonon-phonon Umklapp scattering should give rise to an exponential behavior of the lattice thermal conductivity at high temperatures was suggested by Slack et al. as following:

$$\tau_U{}^{-1}(\omega) = B_U \omega^2 T e^{-\frac{\theta_D}{3T}} \tag{1.7}$$

with

$$B_U = \frac{\hbar\gamma^2}{M v_B{}^2 \theta_D} \tag{1.8}$$

where γ is M is the average mass of an atom in the crystal and the Grüneisen parameter.

1.4.2 Alloying

Scattering by alloying can be viewed as elastic phonon scattering, where momentum is not conserved during the collision. These scattering events are occurred by defects. A perfect one-dimensional spring-mass system indicating atoms in crystal is shown in Fig. 1.7. Since a phonon is a quantized lattice vibration, those imperfections can be treated as a spring-mass system with unsystematic masses and/or spring stiffness.

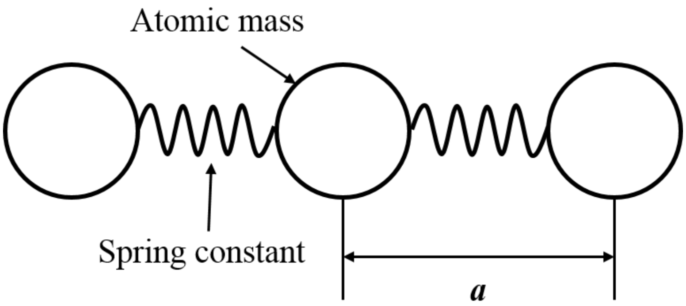

Figure 1.7 A one-dimensional spring-mass system where atoms are represented by point masses in a solid crystal that held by chemical bonds (springs).

Alloying have been generally considered as effective phonon scattering source in reducing thermal conductivity. In bulk materials, alloying scattering can be treated as point defects which is on the order of the atomic scale. Since point defects scatter phonons with a scattering cross section varying as ω^4, while other interaction processes vary more slowly with frequency, the thermal conductivity by phonon can be expressed in an algebraic form only in the limit of high temperatures, where the spectral contribution to the specific heat attains the classical limit. If point defects eliminate the contribution from the high temperature approximation should still be good at somewhat lower temperatures, when the highest frequencies but still holds at lower frequencies which make the major contribution to the thermal conductivity. For this reason, the high temperature approximation still be useful even at intermediate temperatures below the Debye temperature in which scattering due to point-defect is strong enough.

The point-defect is a substitution due to chemically different atom in which the force constants for all of the interatomic interactions and mass is changed. This case can be explained by perturbation theory and produces additional scattering with a relaxation time, known as Klemens-Callaway formulation, such that [10,11]:

$$\tau_p{}^{-1}(\omega) = \frac{V_a\omega^4}{4\pi v^3}\Gamma \tag{1.9}$$

where Γ is the scattering strength, V_a is the volume of atomic, v is the sound speed, and ω^4 is the Rayleigh type scattering. If the concentration is small and the defects are randomly distributed, the magnitude of thermal conductivity is inversely proportional to the concentration of defect. Klemens derived equation for the parameters of scattering that including the differences in the force constants between host atom and substitution atoms, effect of atomic size, and the effect of the strain field associated with substitution. There have been many instances of the success of this empirical approach. However, it should be noted that the effect of atomic size have usually been ignored in the majority of the analyses for lack of appropriate estimates. Thus, point defect scattering is sometimes called mass-difference and it can be enhanced by introducing atoms having a different mass. The scattering will depend on the magnitude of the difference in mass and the alloy composition. Such that:

$$\Gamma = \sum_i f_i \left(\frac{\Delta M}{M}\right)^2 \tag{1.10}$$

$$= \sum_i x_i(1-x_i)\left(\frac{M_i - M}{M}\right)^2 \tag{1.11}$$

where f_i is the atomic fraction, M is the average atomic mass, ΔM is the variation of atomic mass, x_i is the concentration of defects, and M_i is the mass fraction of defects.

An example study of the alloys scattering is shown in Fig. 1.8. SiGe alloys are referred as a prime example where thermal conductivity at room temperature is decreased from 146 $\mathrm{Wm^{-1}K^{-1}}$ in Si to about 7 $\mathrm{Wm^{-1}K^{-1}}$ in SiGe alloys by addition of Ge. Thermal conductivity is significantly decreased by scattering of high frequency (short-wavelength) phonons due to alloy atoms, i.e., the Rayleigh law.

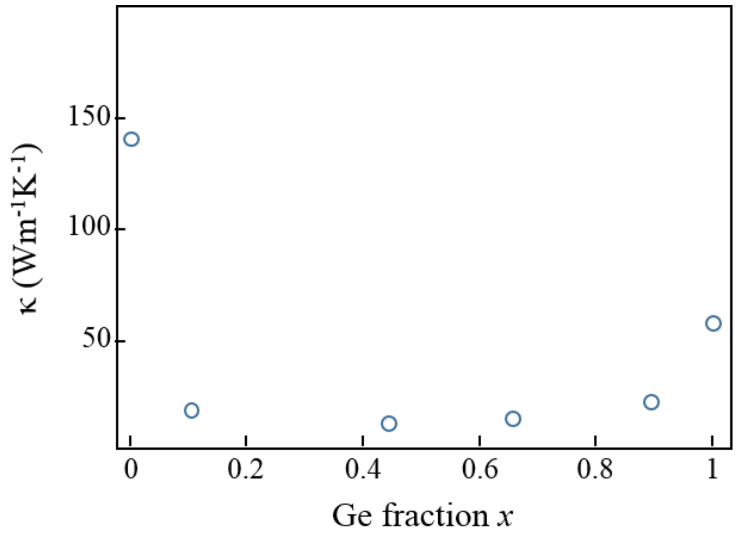

Figure 1.8 Germanium composition dependence of thermal conductivity for bulk $Si_{1-x}Ge_x$ [12].

1.4.3 Nanostructuring

A nanostructuring is more effective way of reducing thermal conductivity than alloying. The various forms of nanostructuring (e.g., embedded nanoparticles (precipitation and inclusion), boundaries (nanowires and nanograins), superlattices) can be quite effective in reduction thermal conductivity. The scattering will depend on boundary surface roughness and size.

Boundary scattering is defined as phonon scattering because of a crystal boundary. Scattering from boundaries in polycrystals restricts severely the contribution of long-wavelength phonons to thermal conductivity. The grain size effect can be modeled by introducing a relaxation time connected with grain boundary scattering. In this sense, the phonon-boundary scattering can be written by assuming independent of temperature and frequency:

$$\tau_B{}^{-1}(\omega) = \frac{v_B}{L} \tag{1.12}$$

where L is the grain size. The L can be adjusted for each crystal in order to fit the third power of T dependence of the thermal conductivity at the lowest temperatures.

1.4.3.1 Nano Sized Grains

The nanocrystalline silicon was studied to demonstrate the boundary effect. Thermal conductivity was reduced as the average grain size decrease from 550 nm to 76 nm at 30 ~ 310 K, as shown in Fig. 1.9. The thermal conductivities of nano-crystalline Si has a T^2 dependence behavior.

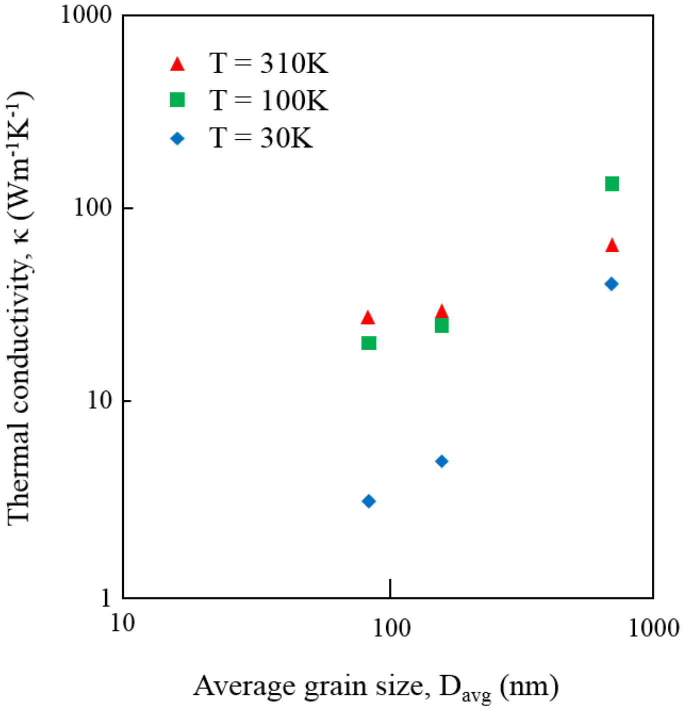

Figure 1.9 Thermal conductivity vs average grain size for un-doped nano-crystalline silicon with average grain sizes ranging from 550 to 64 nm [13].

1.4.3.2 Superlattice

As example study of the nanostructuring scattering is shown in Fig. 1.10. The Si/SiGe superlattices with alternating layers of few *nm* thick Si and SiGe alloy have been found to have thermal conductivity below bulk SiGe alloys, as low as 2 $Wm^{-1}K^{-1}$ which is almost two orders of magnitude below Si and close to the amorphous limit of SiO_2 (~1 $Wm^{-1}K^{-1}$).

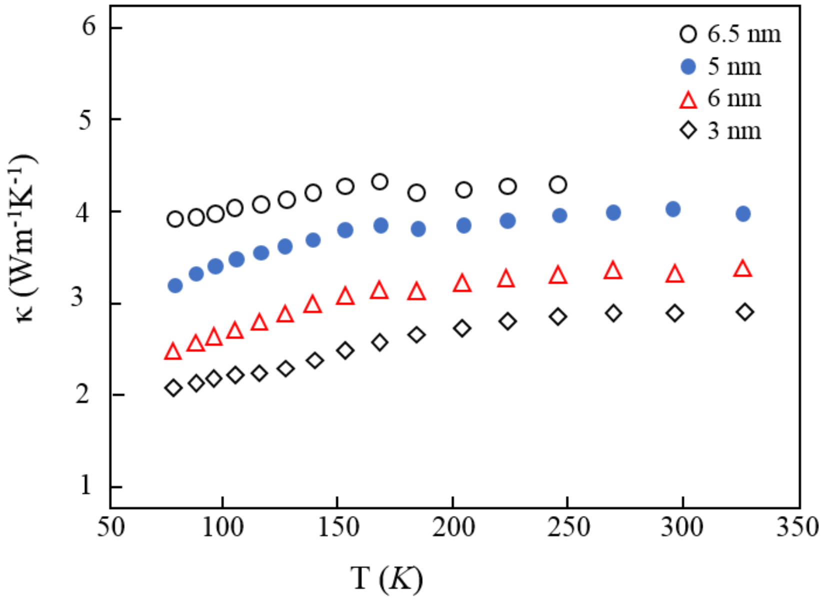

Figure 1.10 Cross-plane thermal conductivity of Si/Ge superlattices with periods ranging from 3 to 6.5 nm [14].

1.4.3.3 Nanowires

As example study of the nanostructuring scattering is shown in Fig. 1.11. The thermal conductivities of pristine 280 nm nanowire sample was lower than bulk sample. And the discrepancy between bulk and nanowire was increased as temperature goes down.

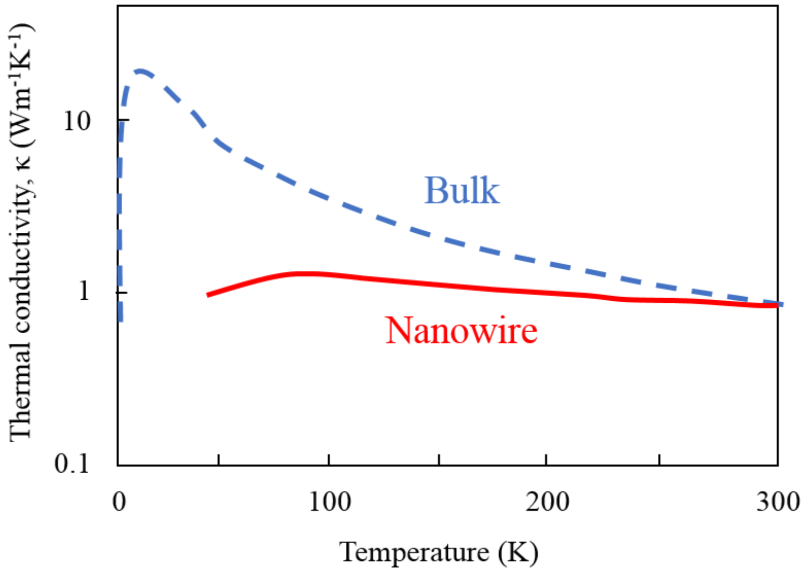

Figure 1.11 Thermal conductivity of pristine 280nm nanowire (solid line) and bulk (dash line) [15].

Kim et al. suggested that rough boundary surface scatter mid-frequency (min-wavelength) phonons [16]. They investigated the difference in thermal conductivity among bulk $Si_{0.96}Ge_{0.04}$, smooth $Si_{0.96}Ge_{0.04}$, and rough $Si_{0.96}Ge_{0.04}$ nanowire. So they found that reduction in thermal conductivity can be explained by the surface roughness scattering mid-frequency (med wavelength) phonons, whereas the high frequency (short-wavelength) phonons are scattered by alloy scattering, and the low frequency (long-wavelength) phonons are scattered by boundary scattering.

The nanostructuring scattering process is generally dominant for long-wavelength phonons and at low temperatures.

1.4.3.4 Nano Precipitation and Inclusion

The nanoscale precipitate and inclusions poses a certain challenge to understanding of effects of microstructural on thermal conductivity. Nano precipitation and inclusions can be considered as second phases with the majority of phonons interacting with interfaces as if they are locally planar, impacting on thermal conductivity by a volumetric factor. Nano precipitates and inclusions will scatter phonons in the same way as point defects, and the formula of Klemens-Callaway described those effect.

There are other feature of nano-sized particles that nano-sized precipitates formed by spinodal decomposition or precipitation are not present in dilute concentrations. Hence the overlap of strain fields cannot be ignored. So, it can be treated by two type model: Klemens-Callaway model or Abeles model. The Klemens-Callaway model treat the concentration effects by making the matrix material an effective medium. In case of Abeles model, it is described as virtual crystal, thus the center of phonon scattering is embedded. The relaxation time by nano-inclusions scattering can be expressed as:

$$\tau_D{}^{-1} = n_i v_B (2\pi R^2) \tag{1.13}$$

with

$$n_i = \frac{3x}{4\pi R^3} \tag{1.14}$$

where R is the radius of spherical inclusions, x is the volume fraction, and n_i is the concentration of inclusions.

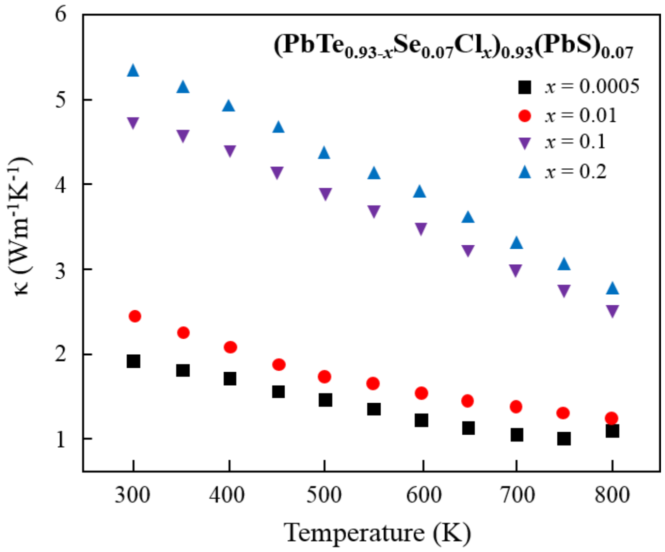

Figure 1.12 Thermal conductivity of $(PbTe_{0.93-x}Se_{0.07}Cl_x)_{0.93}(PbS)_{0.07}$ (x = 0.0005, 0.01, 0.1, and 0.2) compounds [17].

Ginting showed that the significant decrease in lattice thermal conductivity (~ 0.84 $Wm^{-1}K^{-1}$ at 750K) with Cclorine (Cl) dopant produced by phonon scattering at the interfaces of the nano-inclusions.

Although nanostructuring is an efficient way to reduce thermal conductivity, the nanostructured materials undergo significantly changes mechanical properties from the bulk values, leading to unexpected degrading characteristic. Also, nanostructured materials have a large stored energy because of their large grain boundary and thus tend to be unstable with regard to grain growth during high temperature annealing or deformation. That is, nanostructured materials is unstable at high temperature. This is a severe constraint in the high-temperature application.

1.4.4 Anharmonicity by Special Element Alloying

The alloy doping as guest atom on the host atomic site can generate lone pair electrons and suppresses the lattice thermal conductivity by introducing point defects as well as changing anharmonicity in inter-atomic bonding in the system.

As mentioned in section 1.3.4.1, phonon-phonon scattering event is a result of anharmonicity of the chemical bond. The phonon-phonon scattering is an intrinsic process, thus externally increasing the amount of scattering is not simple. So methods to change the phonon-phonon scattering have not been studied as much as those of the phonon-point defects and phonon-boundary scattering. There is a method that of phonon-scattering by lone-pair electrons.

Skoug and Morelli suggested that interaction of lone-pair electrons with neighboring atoms can reduce thermal conductivity because lone pair electrons induce anharmonicity in the crystal lattice [18]. Figure 1.13 shows the schematics of Cu_3SbSe_3 and $CuSbSe_2$. As shown in Fig. 1.13, the electrostatic repulsion between lone pair electrons and neighboring chalcogen ions produces increasing anharmonicity and Grüneisen parameter. In recent years, Nielsen et al. proposed an attractive fact that thermal conductivity of $AgSbSe_2$ reduces to the amorphous limit because the Grüneisen parameter of $AgSbSe_2$ (γ=3.7) is larger than PbTe (γ=1.4) [19].

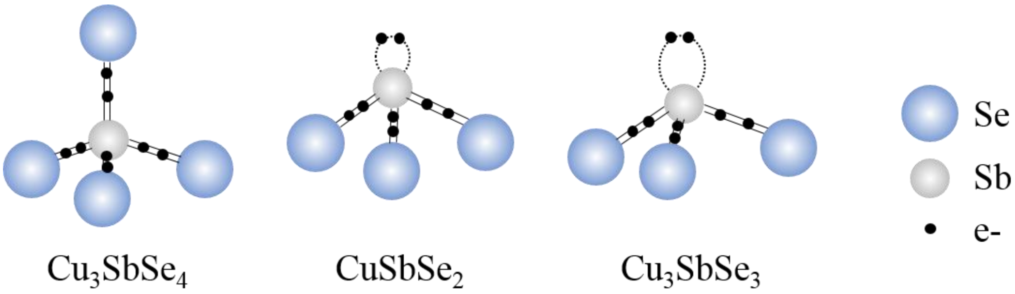

Figure 1.13 Schematic representation of the lone pair electron with illustration of the local atomic environment of Sb in Cu_3SbSe_4, $CuSbSe_2$, and Cu_3SbSe_3 [18].

Enhancing anharmonicity induced by lone pair electrons impacts on Umklapp scattering process and it can be expressed with frequency dependent relaxation time in terms of phonons of velocity and Gruneisen parameter using Slack's model, based on Peierls theory [14]. Such that:

$$\tau_{LPE}{}^{-1}(\omega) = B_{LPE}\omega^2 T e^{-\frac{\theta}{3T}} \tag{1.15}$$

$$B_{LPE} = \frac{\hbar\gamma^2}{M v_x{}^2 \theta} \tag{1.16}$$

$$\gamma = 3\alpha_l V_m / C_v \tag{1.17}$$

where V_m is the molar volume. Although this has attracted much attention, most effort has focused on finding materials with lone pair electrons, and little effort has focused on reducing the thermal conductivity of materials by substituting atoms with lone pair electrons into materials.

1.4.5 Vacancies

Missing atom from an atomic site is called a vacancy. Atoms around the vacancy displaced from their equilibrium positions as shown in Fig. 1.14. This gives rise to a stress field in the vicinity of the vacancy. Vacancy plays an important role in diffusion of substitutional atoms and in many other processes and effect, including some forms of creep and climb of edge dislocations. Non-equilibrium concentration of vacancy can be generated by: 1) plastic deformation, 2) off-stoichiometry in ordered compounds, 3) quenching from a higher temperature, 4) bombardment with high energy particles.

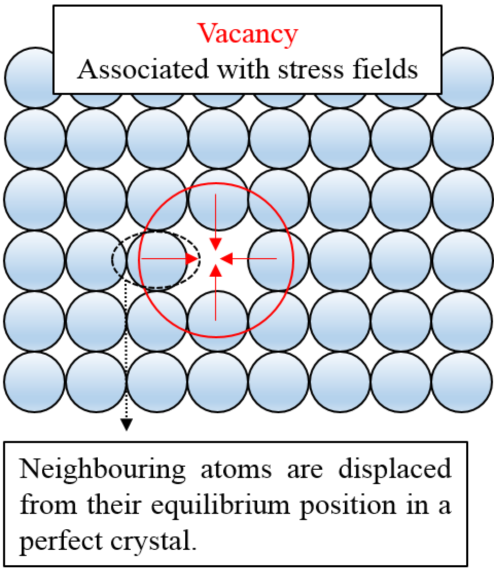

Figure 1.14 Schematic illustration of vacancy.

Vacancies can be classified by position such as randomly distributed vacancies or ordered vacancies. The ordered vacancies become part of the crystal structure and are no longer defects in the usual sense.

1.4.5.1 Randomly Distributed Vacancies

According to Klemens model, point defects, which are generally found in solid solutions, have been demonstrated to play an important role as phonon scattering sources results in much low thermal conductivity based on the strong phonon scattering by changing in the force constants for all of the interatomic interactions and mass. A vacancy is a special kind of lattice defect with a total absence of mass and a mismatch of volume on the crystalline sites as well as the surrounding chemical bonds, thus leading to the strongest phonon scattering and lattice distortion. When the dominant point defects are vacancies, this type of scattering can be maximized.

In $Pr_{0.1}Ce_{0.9}O_{2-\delta}$ system, created point defects of oxygen vacancies and reduced Pr cation produce strong phonon scattering leading to reducing thermal conductivity by ~50% (see Fig. 1.15).

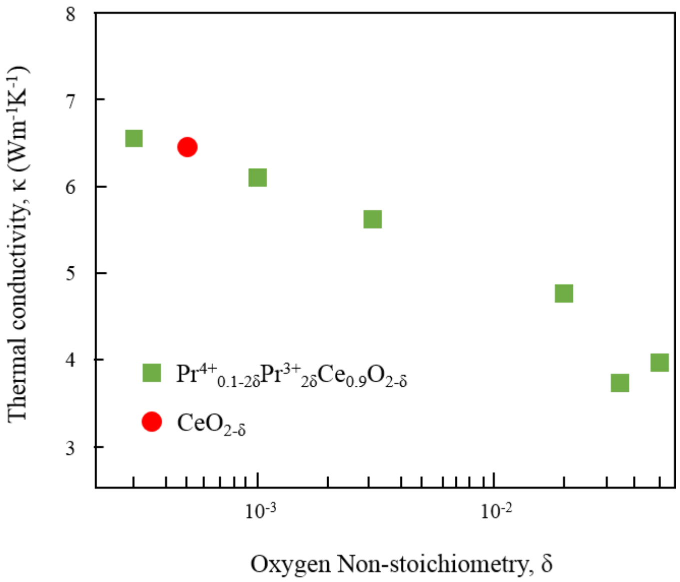

Figure 1.15 Thermal conductivity of $Pr_{0.1}Ce_{0.9}O_{2-\delta}$ films with different oxygen non-stoichiometries [20].

Since a vacancy is a strong local perturbation of the lattice, it is difficult to treat phonon scattering by vacancies. Klemens proposed that vacancy scatter in virtue of both missing mass and missing interatomic linkages [21]. The missing mass of atom implies the removal of kinetic energy equal to the kinetic energy residing in that atom. So a vacancy is equivalent to removing from the materials one atom and all the linkages between that atom and its neighbors. For impurity including vacancies, scattering parameter *Γ* can expressed as

$$\Gamma = \sum_i x_i(1 - x_i)\left(\frac{\Delta M}{M}\right)^2 \tag{1.18}$$

where x_i is the concentration of defects, M is the average atomic mass, and ΔM is the variation of atomic mass. The oxygen vacancies make an additional contribution to *A*. For each oxygen vacancy

$$\left(\frac{\Delta M}{M}\right)^2 = \left(\frac{2M+M_{oxygen\,vacancy}}{M}\right)^2 \tag{1.19}$$

where $M_{oxygen\ vacancy}$ is the average atomic mass of oxygen atom. In this expression, the term $2M$ represents the potential energy perturbation of the missing links at the vacancy and term $M_{oxygen\ vacancy}$ represents the missing kinetic energy of the missing atom. So that:

$$x_i(1-x_i)\left(\frac{\Delta M}{M}\right)^2 = x_i(1-x_i)\left(\frac{\Delta M_{cation}}{M}\right)^2 + m x_i\left(\frac{2M+M_{oxygen\,vacancy}}{M}\right)^2 \tag{1.20}$$

where M_{cation} is the atomic masses of cation, m is the number of oxygen vacancies per solute:1 for divalent solutes and 1/2 for trivalent solutes. This oxygen vacancies lead to effective phonon scattering at high temperatures.

1.4.5.2 Ordered Vacancies

Disordered vacancies can be changed to ordered form due to thermodynamic equilibrium and off-stoichiometry in a compound. Also, there is two type of ordered vacancies: cation vacancies and anion vacancies.

In Ga_2Se_3 (GS) with a zinc-blend structure has high concentration intrinsic cation vacancies, which lead to strong phonon scattering resulting in extremely low lattice thermal conductivity (~0.6 $Wm^{-1}K^{-1}$) as shown in Fig. 1.16. In TiO_{2-x}, off-stoichiometric samples create crystallographic shear planes, which is regularly introduced with the periodicity depending on the oxygen deficiency. These oxygen vacancies lead to strong phonon-vacancy scattering, resulting in lattice thermal conductivity (~2.04 $Wm^{-1}K^{-1}$) (see Fig. 1.17)

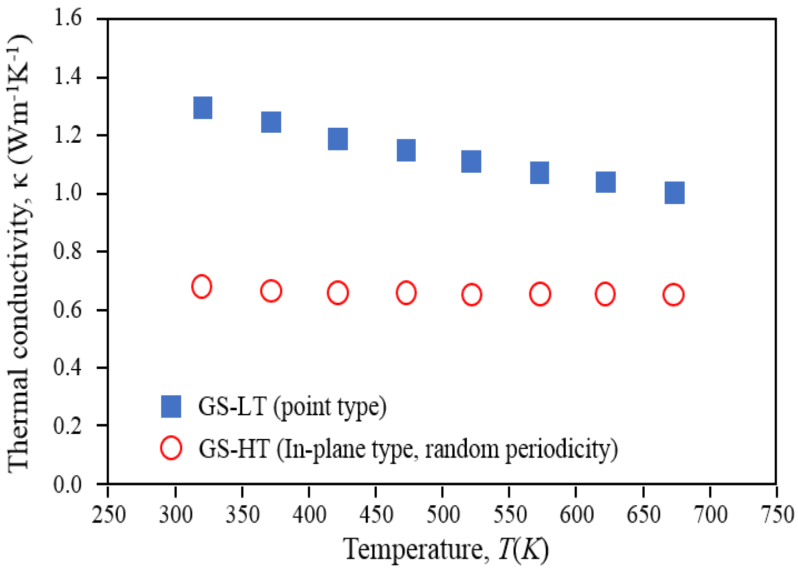

Figure 1.16 Temperature dependence of the thermal conductivity of the Ga_2Se_3samples [22].

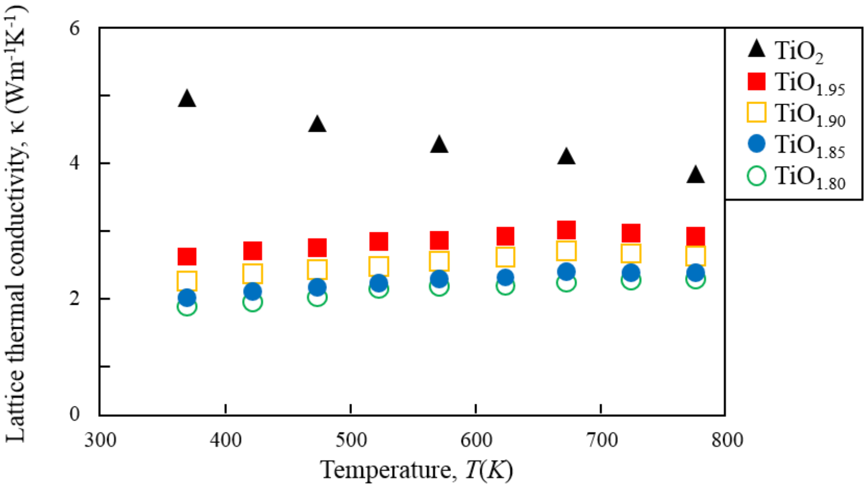

Figure 1.17 (Color online) Temperature dependence of thermal conductivity and lattice thermal conductivity for TiO_{2-x} [23].

The difference between randomly distributed vacancies and ordered vacancies is related to arrangement of vacancies. The arrangement of the vacant site produces a vacancy path within the domain and periodic vacancy planes within a single grain. The vacancy path will discontinue at the domain boundary. So there will be a new path starting in a new domain. This arrangement is related to introduction strong phonon scattering from low temperature region. Unfortunately, there is no expression with a relaxation time for planar defects scattering.

1.5 Purpose of the Present Study

Reduction of thermal conductivity can have a significant impact across a variety of technological areas, including thermal barrier coatings, thermoelectric energy conversion, and thermal insulation materials. Low thermal conductivity is a primary issue in the improvement of efficiency in those applications. Modification of oxides for applications required low thermal conductivity such as refractory, thermal barrier coating, and thermoelectric conversion. High performance can be achieved by making efforts to reduce thermal conductivity as much as possible. Theoretical minimum thermal conductivity (κ_{min}) can be used to model that heat transport in a wide variety of bulk materials with atomic-scale disorder. Thus, minimize the thermal conductivity offers possibilities for application of efficiency optimization.

The purpose of this study is to reduce thermal conductivity down to minimum thermal conductivity. Alloying have been generally considered as effective phonon scattering sources through substitution atom in reducing the thermal conductivity (see Fig. 1.18). Nanostructuring is another representative of an effective phonon scattering sources (see Fig. 1.18). However, nanostructured materials is unstable at high temperature. This is a severe constraint in the high-temperature application.

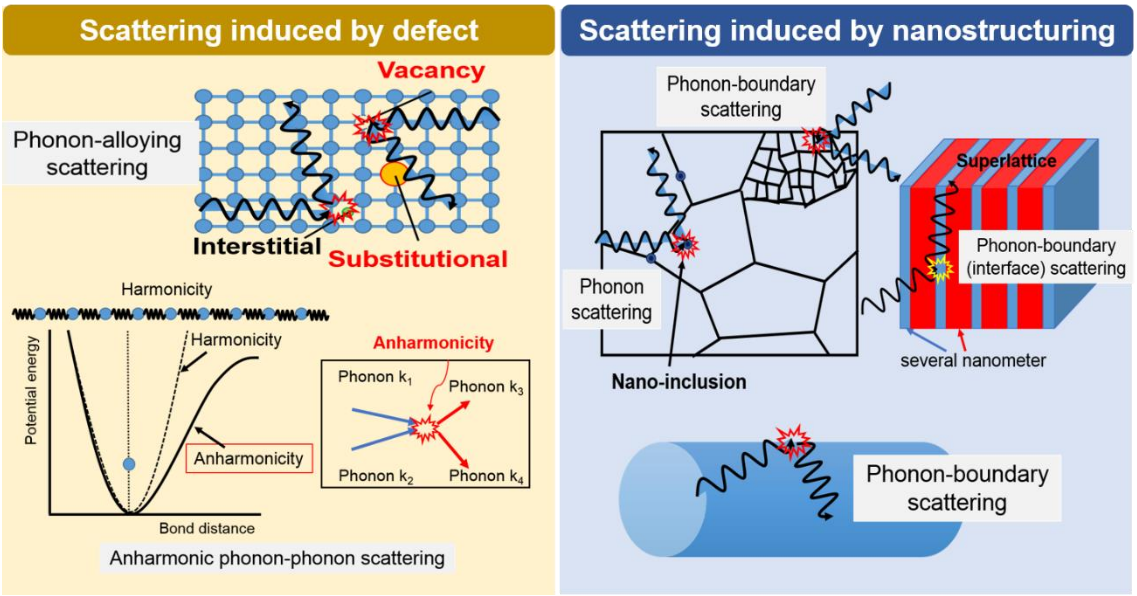

Figure 1.18 Schematic illustration of scattering induced by defects and nanostructuring.

In this dissertation, various phonon scattering mechanisms such as anharmonicity and oxygen vacancies (ordered or random) was studied to further reduction in thermal conductivity to approach the minimum thermal conductivity. The lanthanum molybdate ($La_2Mo_2O_9$) has the potential to be attractive materials for thermal insulators because of their low thermal conductivity. Also, the non-stoichiometric titanium oxides (TiO_{2-x}) has the promising and potential to be attractive functional candidate for thermoelectric materials because of its favorable characteristic for thermoelectric materials: it has significant effects on electron scattering unlike for phonon scattering.

In chapter III, oxygen vacancies has been considered as an effective strong phonon scattering source while maintaining the crystallinity of a material to ensure decent electrical conductivity. The oxygen vacancy concentration was controlled by Ba substitution on La site. The impact on thermal conductivity of varying the concentration of oxygen vacancies and reduced Ba cations in $(La_{1-x}Ba_x)_2Mo_2O_{9-\delta}$ was demonstrated by relaxation time approximation using Klemens-Callaway model (see Fig. 1.19).

In chapter IV, special alloy substitution with lone pair electrons have been reported to exhibit a high anharmonicity and extremely low thermal conductivity. Anharmonic vibrational property is intrinsic to material. Thus, it is not trivial to enhance the scattering through external properties. Although this has attracted much attention, most effort has focused on finding materials with lone pair electrons, and little effort has focused on reducing the thermal conductivity of materials by substituting atoms with lone pair electrons into materials. A precise cause and mechanisms of phonon scattering by lone pair electrons are still unknown. I tried to analyze the effect of lone pair electrons on enhanced phonon scattering by changing anharmonicity through Grüneisen parameter under relaxation time approximation.

In chapter V, vacancies can be disordered (randomly arranged) or ordered based on their position. Even though effect of oxygen vacancies on thermal conductivity has been reported, no studies focused on the effect of point defects (randomly distributed oxygen vacancies) and planar defects (ordered oxygen vacancies) on the thermal conductivity and electrical thermal conductivity. The effect of planar defects on phonon scattering was analyzed using new model by relaxation time approximation.

In chapter VI, the effects of diverse phonon scattering such as alloying, randomly distributed oxygen vacancies, ordered oxygen vacancies, and lattice anharmonicity induced by lone pair electrons on thermal conductivity of bulk compounds (e.g., Ba-doped $La_2Mo_2O_9$, TiO_{2-x}, Bi-doped $La_2Mo_2O_9$) were compared. In order to capture each scattering rate, I build empirical thermal conductivity model based on Klemens-Callaway model, which represents the phonon scattering processes by frequency-dependent relaxation times with the Debye phonon approximation and several other assumptions. Each of the scattering sources is represented by relaxation time. Captured scattering parameters (e.g., alloying, anharmonicity, randomly distributed oxygen vacancies, ordered vacancies) were applied to thermal conductivity of $La_2Mo_2O_9$ to compare each effect.

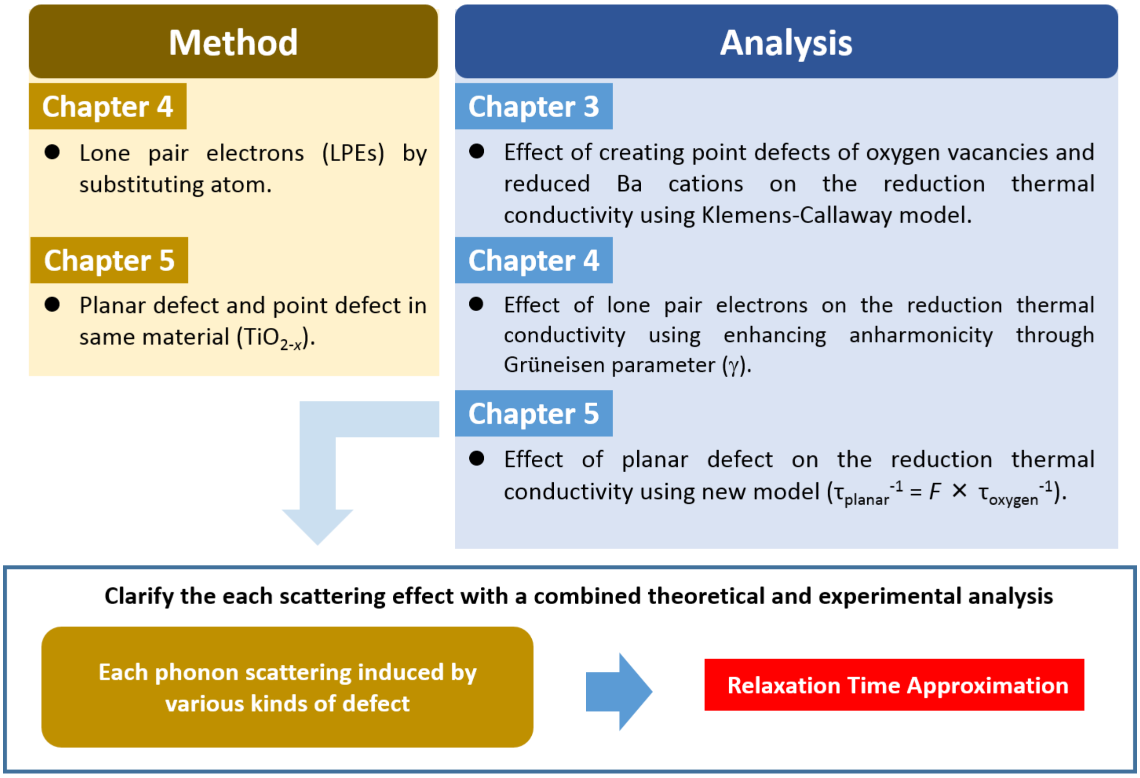

- Lone pair electrons (LPEs) by substituting atom.
- Planar defect and point defect in same material (TiO_{2-x}).
- Effect of creating point defects of oxygen vacancies and reduced Ba cations on the reduction thermal conductivity using Klemens-Callaway model.
- Effect of lone pair electrons on the reduction thermal conductivity using enhancing anharmonicity through Grüneisen parameter (γ).
- Effect of planar defect on the reduction thermal conductivity using new model ($\tau_{planar}^{-1} = F \times \tau_{oxygen}^{-1}$).

Clarify the each scattering effect with a combined theoretical and experimental analysis

Each phonon scattering induced by various kinds of defect

Relaxation Time Approximation

Figure 1.19 Schematic diagram of novelty and originality of this research.

1.6 References

[1] US DOE EIA Annual Energy Review (2006).

[2] D.M. Zhu. NASA/TM 211122 (National Aeronautics and Space Administration) (2001).

[3] Wadley Research Group, Univ. of Virginia.

[4] D.R. Clarke, M. Oechsner, N.P. Padture, *MRS Bull.* **37** 891 (2012).

[5] All fossil fuel reserve and consumption data from CIA World Facebook.

[6] D.M. Rowe, *CRC Handbook of Thermoelectric* (CRC Press, New York, 1995).

[7] *Mantec technical ceramics*, www.mantechtechnicalceramics.com

[8] P.G. Klemens, *Proc. Phys. Soc., London, Sect. A* **68** 1113 (1955).

[9] C.J. Glassbrenner, G.A. Slack, *Phys. Rev*. **134** 1058 (1964).

[10] P G Klemens, *Proc. Phys. Soc. A* **68** 1113 (1955).

[11] J. Callaway, *Phys. Rev*. **122** 787 (1960).

[12] Z. Aksamija, I. Knezevic, *Phys. Rev. B* **88** 155318 (2013).

[13] Z. Wang, J.E. Alaniz, W. Jang, J.E. Garay, C. Dames, *Nano Lett.* **11** 2206 (2011).

[14] G. A. Slack, *J. Phys. Chem. Solids* **34** 321 (1973).

[15] C.H. Chien, P.C. Lee. W.H. Tsai, C.H. Lin, C.H. Lee, Y.Y. Chen, *Sci. Rep.* **6** 23672 (2016).

[16] W.C. Kim, *J. Mater. Chem. C,* **3** 10336 (2015).

[17] D. Ginting, C.C. Lin, L. Rathnam, J.H. Yun, B.K. Yu, S.J. Kim, J.S. Rhyee, *J. Mater. Chem. A* **5** 13535 (2017).

[18] E. J. Skoug, D. T. Morelli, *Phys. Rev. Lett.* **107** 235901 (2011).

[19] M.D. Nielsen, V. Ozolins, J.P. Heremans, *Energy Environ. Sci.* **6** 570 (2013).

[20] M.N. Luckyanova, D. Chen, W. Ma, H.L. Tuller, G. Chen, B. Yildiz, *Appl. Phys. Lett.* **104** 061911 (2014).

[21] C.A. Ratsifaritana, P.G. Klemens, *Int. J. Thermophys.* **8** 737 (1987).

[22] C.E. Kim, K. Kurosaki, M. Ishimaru, H. Muta, S. Yamanaka, *J. Electron. Mater.* **40** 999 (2011).

[23] S. Harada, K. Tanaka, H. Inui, *J Appl Phys.* **108** 083703 (2010).

CHAPTER II

Experimental Methods

2.1 Sample Preparation

In my dissertation, the all of bulk samples were prepared in two ways: 1) the $La_2Mo_2O_9$ series powder samples were synthesized and compacted via conventional solid-state reaction method, 2) the TiO_{2-x} series bulk samples were compacted and fabricated via spark plasma sintering and oxidation reduction reaction. The basic principle of preparation (sysnthesis) and characterization methods will be described in this chapter.

2.1.1 Solid State Sintering

Solid state reaction method is the most widely used method for powders in the mixtures of solid. The reaction process takes place on the interfaces and diffuse between two solids. The rate of a solid-state reaction is affected by many factors (i.e., chemical composition, particle size, temperature, pressure, atmosphere, etc.). Those factors contribute the inner and outer diffusion of the reactant species. Thus, the activation energies of the diffusion for cations is crucial role in solid state reaction [1]. Similar with solid state reaction, the reduction in the surface free energy of a sintering compact provides the driving force for sintering. The driving force for sintering is defined in terms of a sintering stress that has the same effects on sintering as the curved surfaces of pore and grain boundaries [2,3].

A powder compact microstructure evolves during sintering process. In initial stage, sharply concave necks form between the individual particles in compact powders. The degree of densification is generally small in this stage. In the intermediate stage, the microstructure consists of a three-dimensional interpenetrating network of solid particles and continuous like channel pores. This stage covers most of densification. And grain growth starts to become significant in this stage. In final stage, the channel like pores break down into isolated and closed voids. And grain growth become more extensive and difficulties are encountered in the removal of the few percent of porosity [4].

Sintering of crystalline materials can occur by some mechanisms such as surface diffusion, vapor transport, lattice diffusion, and grain-boundary diffusion. Figure 2.1 shows a schematic of the sintering mechanisms for two adjacent spherical particles. Surface diffusion, vapor transport, and lattice diffusion from the particle surfaces to the neck bring about neck growth and coarsening of the particles without densification. Lattice diffusion and grain-boundary diffusion from the grain boundary to the neck are the most important mechanisms of densifying in polycrystalline ceramics. For M_xO_y, the effective diffusion coefficient (D_{eff}) can be expressed as [5]:

$$D_{eff} = \frac{(x+y)\left[D_l{}^M + \frac{\pi\delta_{gb}D_{gb}{}^M}{G}\right]\left[D_l{}^O + \frac{\pi\delta_{gb}D_{gb}{}^O}{G}\right]}{y\left[D_l{}^M + \frac{\pi\delta_{gb}D_{gb}{}^M}{G}\right] + x\left[D_l{}^O + \frac{\pi\delta_{gb}D_{gb}{}^O}{G}\right]} \tag{2.1}$$

where subscripts *l* and *gb* are lattice and grain boundary diffusion, respectively, subscripts M and O are the metal and oxygen ions, respectively, *D* is the diffusion coefficient, *G* is the grain size, and *δ* is the thickness of the grain boundary.

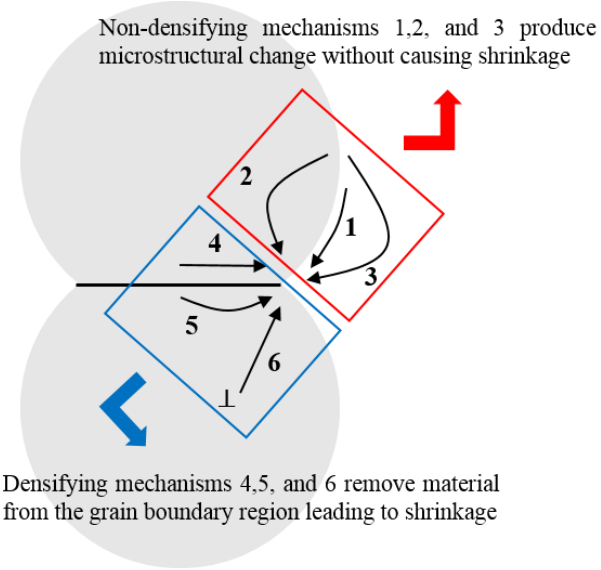

Figure 2.1 Densifying mechanisms: 1. Surface diffusion, 2. Lattice diffusion from the surface, 3. Vapor transport, 4. Grain boundary diffusion, 5. Lattice diffusion from the grain boundary, and 6. Plastic flow by dislocation motion.

2.1.2 Spark Plasma Sintering

A wide variety of techniques have been developed to obtain high densification with a desired microstructure and phase composition. Spark plasma sintering (SPS) process is effective for high heating rate with minimal grain growth [4]. A schematic of the method is shown in Fig. 2.2. The mechanism of the spark plasma sintering is based on the micro spark discharge in the gap between individual particles in compact powders. The spark plasma sintering proceeds through a three-stage process. In first stage, the surface of particle melt and fuse to each other forming "necks" between neighboring powder particles. In second stage, the joule heat, generated by pulsed DC electrical current, reacts between the necks connecting individual particles (see Fig. 2.3). The diffusion of the atoms in the necks was increased and enhanced their growth by joule heat. In third stage, the heated samples becomes softer and exerts plastic deformation under the uniaxial force, leading to the high densification of the powder compact of its theoretical density.

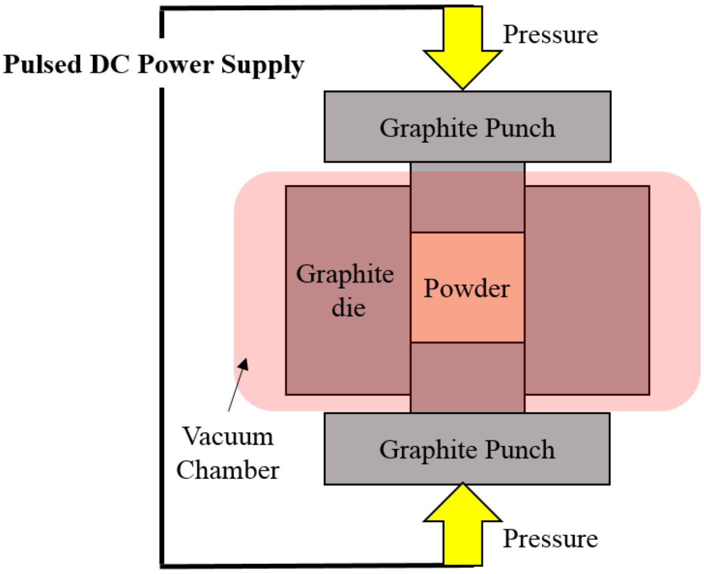

Figure 2.2 Schematic of spark plasma sintering technique.

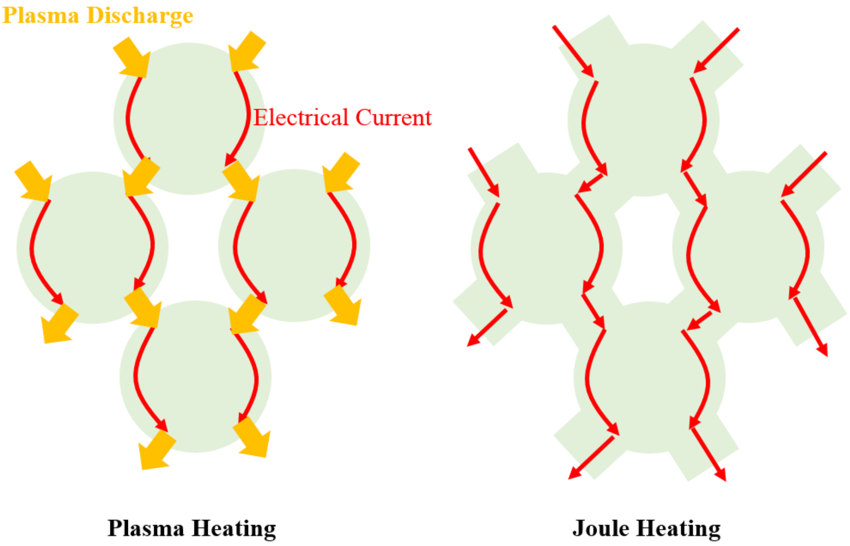

Figure 2.3 Schematic of spark plasma sintering mechanism.

2.2 Characterization Methods

2.2.1 X-ray Powder Diffraction

The crystal structures and phase compositions were determined by powder X-ray diffraction (XRD) (ULTIMA IV, Rigaku) using Cu-Kα radiation (λ = 1.5406 Å) with a scintillation or semiconductor detector. The lattice parameter, theoretical density, and thermal expansion coefficient were determined by the XRD results. The materials consisted of regular arrays of atoms can be identified by using a database of X-ray diffraction patterns because crystalline materials have unique diffraction patterns. Since X-ray is waves of electromagnetic radiation, the X-ray waves is scattered by atoms, primarily through the electrons of atoms. X-ray striking an electron produces secondary spherical waves originating from the electron. This phenomenon is because that energy of X-ray is much greater than that of a valence electron. The scattering known as elastic scattering can be modeled as Thomson scattering, which is the interaction of an electromagnetic ray with a free electron. Thus, the intensity of scattering can be expressed as [6]:

$$I_e = I_0 \left(\frac{e^4}{m^2c^4r^2}\right)\frac{1+cos^2 2\theta}{2} \tag{2.2}$$

where m is the electron mass, I_0 is the intensity of the incident X-ray beam, c is the light speed, r is the distance to observed position, and e is the electron charge.

The incident waves have wavelengths comparable to the spacing between atoms. Figure 2.4 shows geometry for interference of a wave scattered from two planes separated by an inter-planar spacing. From Fig. 2.4. Angle of incidence of the two parallel rays is considered as θ. The inter-planar spacing, d, is the difference in path for the X-ray scattered from the top plane and bottom plane. When the difference in path length for the top and bottom X-ray is equal to one wavelength, λ, the constructive wave interference was occurred by Bragg's law:

$$n\lambda = 2dsin\theta \tag{2.3}$$

where n is any integer. These specific directions appear as spots on the diffraction pattern, which called reflections. A reflections from a crystalline material contains many distinct peaks, corresponding to a different interplanar spacing. And they are to be indexed the records of Miller index of each reflection, (*hkl*).

A powder X-ray diffractometer consists of the X-ray tube, the sample stage, and the detector. The incident angle is defined between the X-ray beam source and the sample. The diffraction angle, 2θ, is defined between the incident beam and the detector. The incident angle is always one half of the detector angle 2θ. In a θ:2θ instrument of ULTIMA, the sample rotates at θ°/min and the detector rotates at 2θ°/min (see Fig. 2.5).

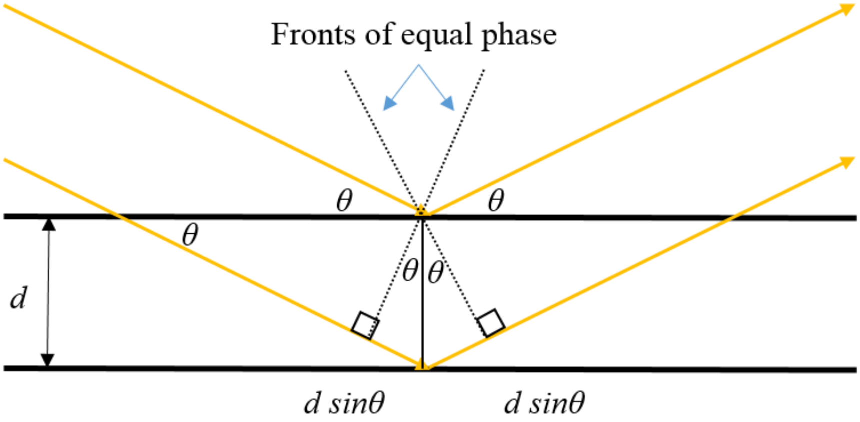

Figure 2.4 Schematic illustration of powder X-ray diffraction by atoms.

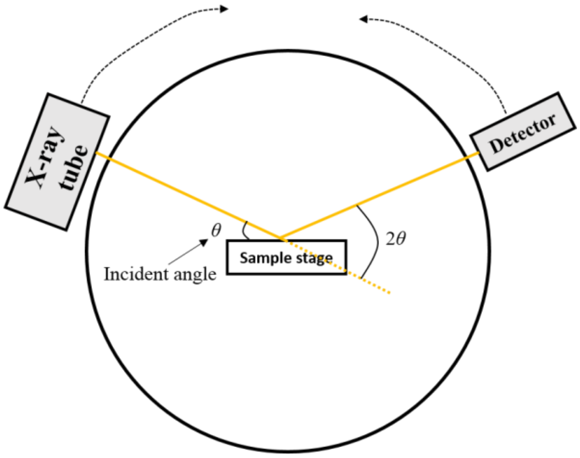

Figure 2.5 Schematic illustration of powder X-ray diffracting apparatus.

2.2.2 Elastic Moduli and Debye Temperature

In materials, sound waves can propagate based on the way the particles oscillate. The movement of particle responsible for the propagation of longitudinal and transverse waves is shown in the Fig. 2.6. The longitudinal and transverse waves are the two modes of propagation widely used in pulse-echo ultrasonic measurement. It consists of the pulser/receiver, transducer, and a display device. A pulser/receiver produce high voltage electrical pulses. The transducer generates high frequency ultrasonic energy due to driven by the pulser. The introduced sound energy propagates through the samples in the form of waves. If there is a discontinuity (e.g., crack, pore) in the wave path, part of the energy will be reflected back from the flaw surface. The signal of reflected wave is transformed into an electrical signal by the transducer and is displayed on a screen as shown in Fig. 2.7. The time of travel can be directly related to the distance that the signal traveled. The longitudinal and transverse sound velocity are expressed by:

$$v_L = \frac{2L}{t_2 - t_1} \tag{2.4}$$

and

$$v_S = \left[\left(\frac{t_3 - t_2}{D}\right)^{\frac{1}{2}} + \left(\frac{t_2 - t_1}{2L}\right)^{\frac{1}{2}}\right]^{-\frac{1}{2}} \tag{2.5}$$

where D is the sample diameter, L is the sample length, t_1 is the time of reflection for the longitudinal sound velocity from the lower face of the sample, t_2 is the time of reflection for the longitudinal sound velocity from the upper face of the sample, and t_3 is the time of reflection for the transverse sound velocity from the upper face of the sample. A 5 or 10 MHz longitudinal and 10MHz transverse wave pulse were used for obtaining the longitudinal and transverse sound velocity, respectively.

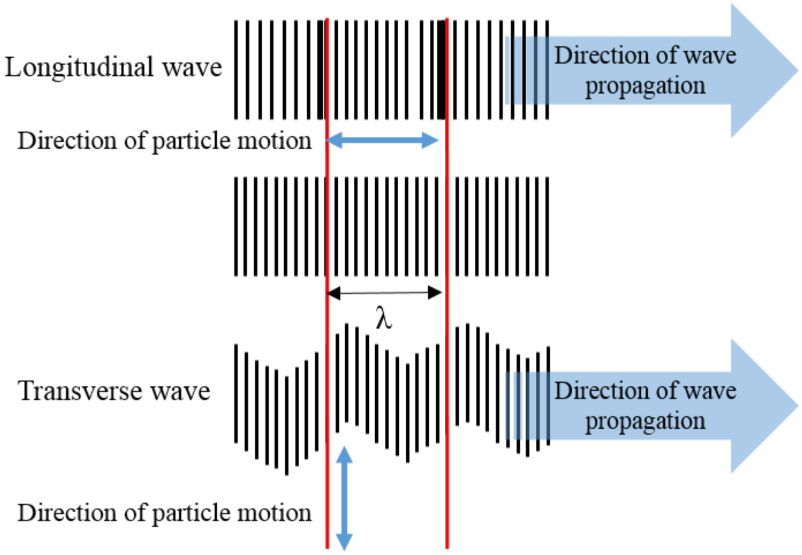

Figure 2.6 Schematic illustration of longitudinal and transverse wave.

The elastic moduli such as bulk modulus (*B*), shear modulus (*G*), Young's modulus (*E*), Compressibility (β), and Debye temperature (θ_D) were evaluated in terms of the longitudinal sound velocity (V_L) and transverse (shear) sound velocity (V_S) of samples as followed [7,8]:

$$G = \rho V_S^2 \tag{2.6}$$

$$E = \frac{G[3V_L^2-4V_S^2)}{V_L^2-V_S^2} \tag{2.7}$$

$$B = \rho\left(V_L^2 - \frac{4}{3}V_S^2\right) \tag{2.8}$$

$$\beta = \frac{1}{B} \tag{2.9}$$

$$\theta_D = \left(\frac{h}{k_B}\right)\left(\frac{9N}{4\pi V_C}\right)^{\frac{1}{3}}\left(\frac{1}{V_L^3}+\frac{2}{V_S^3}\right)^{-1/3} \tag{2.10}$$

where ρ is the sample density, k_B is the Boltzman constant, *h* is the Planck's constant, V_c is the unit cell volume, and *N* is the number of atoms in the unit cell.

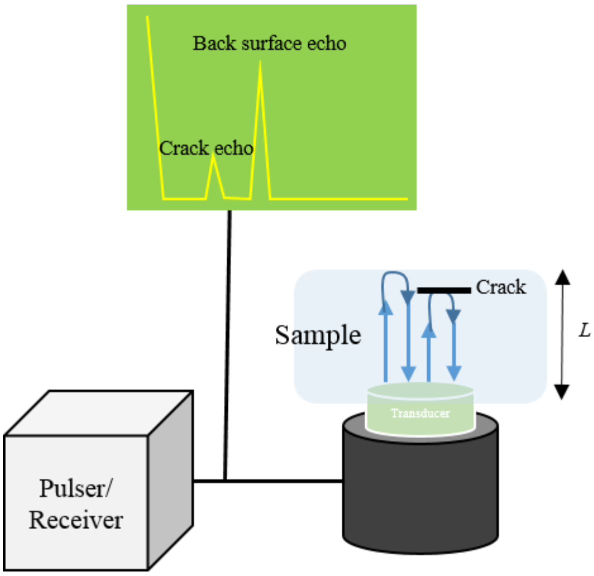

Figure 2.7 Schematic illustration of measurement of sound velocity.

2.2.3 Carrier Concentration and Mobility

Direct current Hall effect measurements were performed using a Toyo ResiTest 8340 system at an applied magnetic field of 0.5T in a van der Pauw geometry to determine the charge carrier density and mobility. The Hall mobility (μ_H) and Hall carrier concentration (n_H) were calculated from the observed Hall coefficient (R_H) assuming a single band model and Hall factor (γ_H) of 1 by the following equations:

$$\mu_H = \frac{R_H}{\rho} \tag{2.11}$$

and

$$n_H = \frac{1}{eR_H} \tag{2.12}$$

where ρ is the resistivity and e is the charge of an electron (1.602×10^{-19}C). The Hall coefficient is expressed by the followed equation using the Hall voltage (V), current (I), magnetic field (B), and the thickness of specimen (h_k).

$$R_H = \frac{|V_{23}|h_k}{I_{14}B} = \frac{h_k}{B}R_{12,34} \tag{2.13}$$

Here, subscript number represents proves as shown in Fig. 2.8. Two resistances is given by twice measurements:

$$R_{12,34} = \frac{|V_{23}|}{I_{14}} \tag{2.14}$$

and

$$R_{23,41} = \frac{|V_{41}|}{I_{23}} \tag{2.15}$$

The resistivity is calculated by:

$$\rho = \frac{\pi}{\ln 2} h_k \frac{R_{12,34} + R_{23,41}}{2} f \tag{2.16}$$

The factor f depends on the ratio of $R_{12,34}/R_{23,41}$ (see Fig. 2.8).

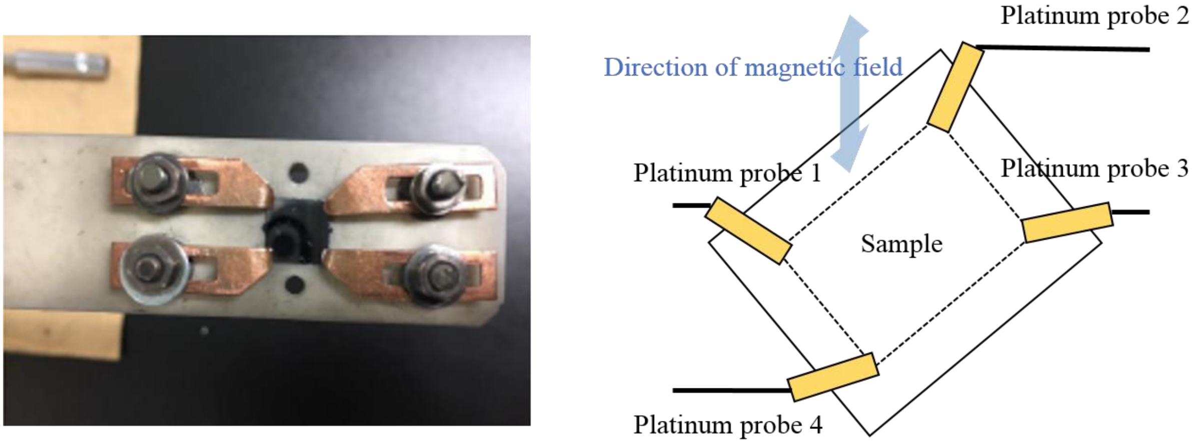

Figure 2.8 Schematic illustration of method of van der Pauw's.

2.2.4 Differential Scanning Calorimetry

The specific heat capacity was measured using a differential scanning calorimeter (DSC;Jupiter, NETZSCH). The instrument measures the difference between feat flows from the reference (empty) and sample sides of a sensor as a function of temperature. The measurement of specific heat capacity at constant pressure (C_p) was performed following the standard ASTM E-1269. This system consists of a blank (baseline), a sapphire (reference material), and the sample over the same temperature range at a fixed rate in a controlled atmosphere (high-purity argon flowing at 30 mL/min). The difference in heat flow between the blank and the sapphire or the sample is continuously recorded because of energy changes. The instrument provides corrected heat flows for the sapphire and for the sample. This value is obtained after subtracting the heat flow of the blank from the sapphire or sample. The corrected values of heat flow are used to calculate the sample's heat capacity by using the sapphire's (reference) heat capacity and the sapphire reference's weight and sample's weight as followed:

$$C_p = \frac{m_{reference}}{m_{sample}} \times \frac{HF_{sample}}{HF_{reference}} \times C_{p,reference} \tag{2.17}$$

where $C_{\text{p,reference}}$ is the heat capacity at constant pressure for sapphire reference material, m_{sample} is the weights of sample, $m_{\text{reference}}$ is the weights of sapphire reference material, HF_{sample} is the heat flows of the sample, and $HF_{\text{reference}}$ is the heat flows of the sapphire reference material.

2.2.5 Thermal Expansion Coefficient

The linear thermal expansion coefficient (LTEC) was determined using horizontal pushrod dilatometer. The coefficient of average linear thermal expansion (α_l) is obtained from the measured thermal expansion as follows:

$$\alpha_l = \frac{1}{l_0}\frac{dl}{dT} = \frac{1}{l_0}\frac{(l_f - l_0)}{(T_f - T_0)} \tag{2.18}$$

where l_0 is the original length of the sample with the temperature T_0 and l_f is the final length of the sample with the temperature T_f. The horizontal pushrod dilatometer consists of a cantilevered horizontal tube into a cavity of furnace as shown in Fig. 2.9. A pushrod is located at the center and parallel to the axis of the horizontal tube. The pushrod is affixed to a high sensitivity transducer of linear displacement. Both sample and alumina reference rods are fastened to the fixed holder, which is located against the sealed end of the horizontal tube and is held in place by a force sustained on the pushrod from the opposite site. The applied force through the pushrod has to be sufficient to sustain complete contact between the fixed tube, the specimen (and alumina reference) and pushrod. The difference in displacement from the two rods is recorded as the two specimen heat up simultaneously. The thermal expansion of the material is calculated from that of the alumina reference material and the relative displacement of the pull rods.

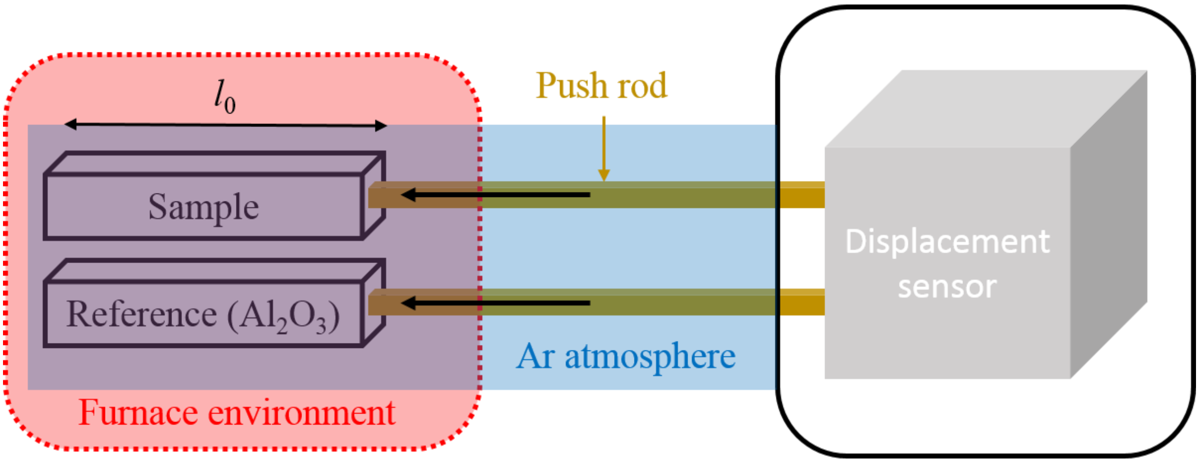

Figure 2.9 Schematic illustration of method of dilatometer.

2.2.6 Thermal Conductivity

The thermal conductivity (κ) was calculated from the thermal diffusivity (d) specific heat capacity at constant pressure (C_p), and density using the following equation:

$$\kappa = dC_p\rho \tag{2.19}$$

The thermal diffusivities were determined by a laser flash method using an LFA457 instrument. The laser flash method is illustrated as shown in Fig. 2.10. Prior to thermal diffusivity measurement, both faces of samples were coated by graphite using graphite spray to improve the laser absorption at the lower surface and to increase the intensity of the emissions of the upper surface. The theory of the method for thermal diffusivity is followed [9]:

If the distribution of initial temperature within a thermally insulated uniform thickness (h_k) of sample is T (x,0), the distribution of temperature at later time t is given by:

$$T(x,t) = \frac{1}{h_k}\int_0^{h_k} T(x,0)\,dx + \frac{2}{h_k}\sum_{n=1}^{\infty} exp\left(\frac{-n^2\pi^2 td}{{h_k}^2}\right) \times \cos\frac{n\pi x}{h_k}\int_0^{h_k} T(x,0)\cos\frac{n\pi x}{h_k}\,dx \tag{2.20}$$

If a radiant energy pulse (Q) is simultaneously and uniformly absorbed in the shallow depth g at the lower surface x = 0 of a thermally insulated material of uniform thickness (h_k) the distribution of temperature at that instant is expressed by:

$$T(x,0) = \frac{Q}{\rho C_p g} \quad (0 < x < g) \tag{2.21}$$

and

$$T(x,0) = 0 \quad (g < x < h_k) \tag{2.22}$$

Under the initial condition, Eq. (2.20) can be written by

$$T(x,t) = \frac{Q}{\rho C_p h_k}\left[1 + 2\sum_{n=1}^{\infty} \cos\frac{n\pi x}{h_k}\frac{\sin(n\pi g/h_k)}{(n\pi g/h_k)} \times exp\left(\frac{-n^2\pi^2}{{h_k}^2}td\right)\right] \tag{2.23}$$

It follows $\sin(n\pi g/h_k) \approx (n\pi g/h_k)$ because g is a quite small for opaque materials. At the upper surface where $x = h_k$, the temperature can be expressed as

$$T(h_k,t) = \frac{Q}{\rho C_p h_k}\left[1 + 2\sum_{n=1}^{\infty} (-1)^n\, exp\left(\frac{-n^2\pi^2}{{h_k}^2}td\right)\right] \tag{2.24}$$

Dimensionless terms, V and ω can be defined as

$$V(h_k,t) = \frac{T(h_k,t)}{T_M} \tag{2.25}$$

and

$$\omega = \frac{\pi^2 td}{{h_k}^2} \tag{2.26}$$

Here, T_M is the maximum temperature at the upper surface. The combination of Eq. (2.24), (2.25), and (2.26) produces

$$V = 1 + 2\sum_{n=1}^{\infty}(-1)^n exp(-n^2\omega) \tag{2.27}$$

The produced Eq. (2.27) is plotted as shown in Fig. 2.10. From Eq. (2.27) and Fig. 2.10, h_k have been deduced. When V is equal to 0.5, ω is equal to 1.38 as follows:

$$d = \frac{1.38{h_k}^2}{\pi^2 t_{1/2}} \tag{2.28}$$

where $t_{1/2}$ is the from the initiation of the pulse laser until the temperature rise of the upper face of the sample reaches to the half-maximum. The uncertainty for the thermal diffusivity measurements can be expressed by

$$d + \Delta d = \frac{1.38(h_k+\Delta h_k)^2}{\pi^2(t_{1/2}+\Delta t)} \tag{2.29}$$

where Δd, Δt, and Δh_k are uncertainty of d, $t_{1/2}$, and h_k, respectively. When the surface of the sample is covered by a carbon film, additional time is needed to reach heat from the lower to upper surface of the sample due to the thermal resistance of the carbon film. Thus, the variation in the thickness of the carbon is associated with Δt. Δh_k is associated with the variation in h_k or uncertainty in the measurements of h_k. Although the quantitative estimation of Δd must be done by error propagation law using Δt and Δh_k, Eq. (2.28) allows qualitative discussion about Δd. Eq. (2.28) shows that assuming Δt and Δh_k to be constant, Δd becomes small with increasing $t_{1/2}$. The value of $t_{1/2}$ becomes larger when a material has lower thermal conductivity, which indicates that the uncertainty in the thermal diffusivity measurements become small when the sample has very low thermal conductivity.

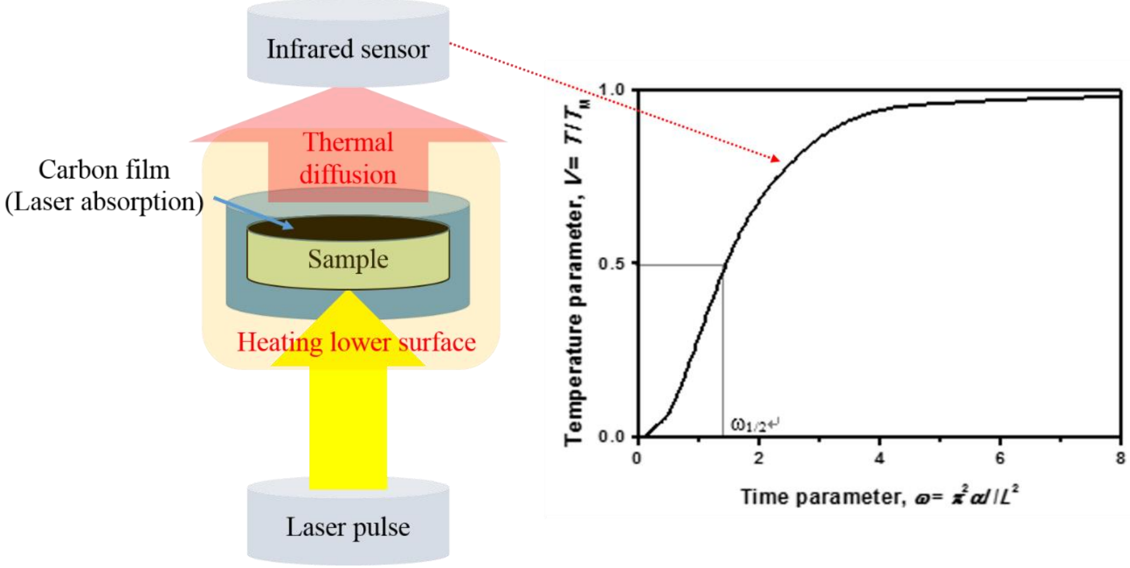

Figure 2.10 (Left) Schematic illustration for the laser flash measurement and (Right) Dimensionless plot of upper surface temperature history.

2.3 References

[1] X. Zhu, W. Yang, *Mixed conducting ceramic membranes* (Springer-Verlag GmbH, Berlin, 2017)

[2] L.C. De Jonghe, M.N. Rahaman, *Acta metall*. **36** 223 (1988).

[3] R. Raj, *J. Am. Ceram. Soc*. **70** C210 (1987).

[4] L.C. De Jonghe, M.N. Rahaman, *Sintering of ceramics*. In: S. Somiya, F. Aldinger, N. Claussen, eds. *Chapter 4 in Handbook of Advanced Ceramics* (Elsevier, New York, 2003), p.187.

[5] R.S. Gordon, *J. Am. Ceram. Soc*. **49** 366 (1966).

[6] G. Andre, *X-ray crystallographic technology* (Hilger and Watts LTD, London, 1952), p. 271.

[7] E. Schreiber, O.L. Anderson, N. Soga, *Elastic constants and their measurements* (McGraw-Hill, New York, 1973), p. 1.

[8] H. Inaba, T. Yamamoto, Netsu Sokutei *(J. Jpn. Soc. Cal. Therm. Anal.)***10** 132 (1983).

[9] W.J. Parker, R.J. Jenkins, C.P. Butler, G.L. Abbott, *J. Appl. Phys*. **32** 1679 (1961).

CHAPTER III

Effect of Ba Substitution on Thermophysical Properties of Lanthanum Molybdate

In this chapter, the author covers an effect of Ba substitution atom (alloying) and randomly distributed oxygen vacancies by separating Ba substitution atom and oxygen vacancies effects on the reduction thermal conductivity in polycrystalline bulk lanthanum molybdate. Each phonon scattering was clarified by combined theoretical and experimental analysis. The properties such as thermal expansion coefficient, heat capacity, elastic moduli, Debye temperature, and thermal conductivity of the compounds were studied to build empirical thermal conductivity model. The author incorporated the phonon scattering effect of substitution atom and oxygen vacancies into the relaxation time. The obtained results was used for comparison of the various phonon scattering effects on thermal conductivity.

3.1 Introduction

3.1.1 Crystal Structure of Lanthanum Molybdate

Lanthanum molybdate, $La_2Mo_2O_9$, is a recently discovered compound that has attracted considerable attention because is exhibits a quite low thermal conductivity ($0.95 Wm^{-1}K^{-1}$ at 1273K) [1]. The low thermal conductivity is closely related to crystal structure. $La_2Mo_2O_9$ has a pseudocubic monoclinic low temperature α from and cubic high temperature β form. The crystal structure of β form appears to be very close to that of β-$SnWO_4$ with extra oxygen atoms in statistical occupation. Figure 3.1 shows the schematic of cationic environments in β-$SnWO_4$ and β-$La_2Mo_2O_9$. It can be noted that cations occupy the same type of positions in both compounds, as well as most anions. In case of β-$La_2Mo_2O_9$, the extra oxygen atom partially occupies, the site normally occupied by the Sn^{2+} lone pair in β-$SnWO_4$. It is to be noted that O2 of the O3 sites of β-$La_2Mo_2O_9$ are partially occupied, which represent three quarter (3/4) of the total number of oxygen atoms, and as many vacancies.

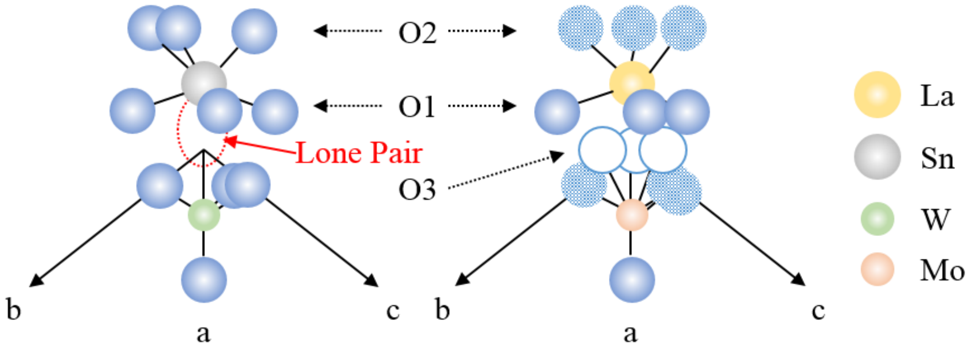

Figure 3.1 Environments of cationic in β-$SnWO_4$ (left) and β-$La_2Mo_2O_9$ (right). Hatched and open circle oxygen sites are partially occupied. For clarity, the environment of La is limited to the nearest neighbours [2].

3.1.2 Low Thermal Conductivity and High Anharmonicity in Lanthanum Molybdate

In $La_2Mo_2O_9$ system, the low thermal conductivity is happened for two reasons. First, $La_2Mo_2O_9$ has a highly complex structure with many atoms in its primitive cell (N=624) [3]: each atoms have different phonon modes and disorders, thus the $La_2Mo_2O_9$ compound with phonon dispersions are progressively complex. The complex phonon dispersions impact on changing the states available for Umklapp scattering and leading to highly frequency-dependent phonon velocities (see Fig. 3.2), preventing heat conduction. Second, $La_2Mo_2O_9$ has intrinsic oxygen vacancies from partially (78%) occupied oxygen sites: randomly distributed oxygen vacancies scatter phonons. In addition, the intrinsic oxygen vacancies influence electrostatic repulsive force surrounding them. The presence of additional repulsion of the lattice force can in turn contribute to a stronger lattice anharmonicity like electrostatic repulsion of lone pair electrons. For a normal lattice, anharmonic cubic term of the inter-atomic potential energy expansion favors expansion of lattice as if it generates a repulsive component of the force of lattice. Conversely, additional repulsion of the lattice force can contribute to a stronger lattice anharmonicity [4,5]. Wang and coworkers propose the electrostatic repulsive force of the exposed cations surrounding oxygen vacancies as the underlying reason for the high anharmonicity at oxygen vacancy sites. It is understandable that since the emergence of vacancies disrupts the alternation of cations and anions in the perfect ionic lattice and hence leads to anions/cations exposed to each other around cationic/anionic vacancies, oxygen vacancies arise from an electrostatic repulsion force of exposed cations surrounding them lead to increase of Grüneisen parameter and the decrease of Young's modulus (see Fig. 3.3) [6].

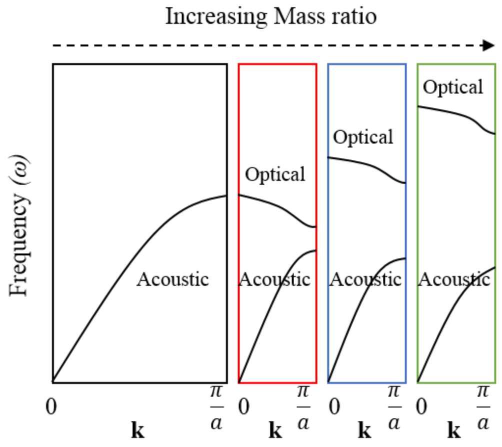

Figure 3.2 Schematic of illustration of BvK model for a 1D diatomic chain: as mass contrast increases the optical mode flattens and the gap increases [3].

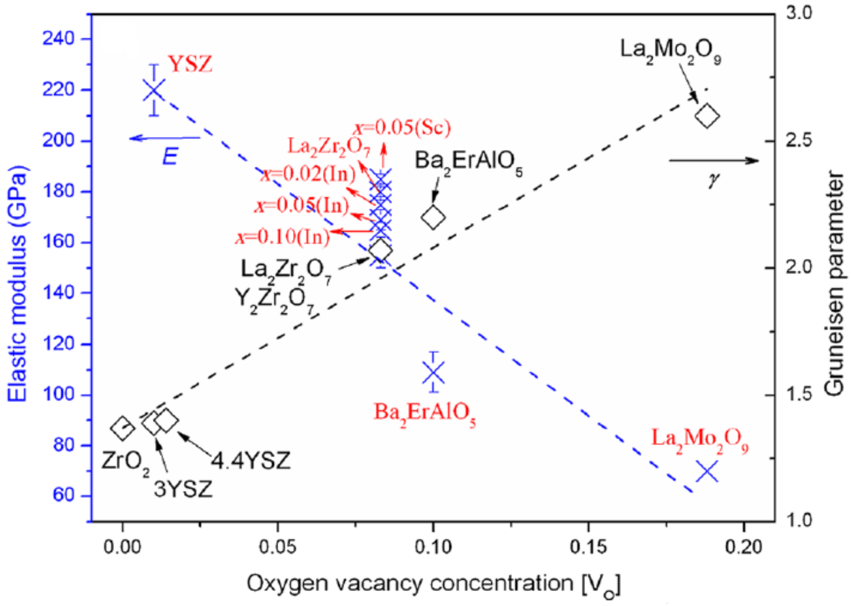

Figure 3.3 Oxygen vacancy concentration dependence of elastic modulus (Young's modulus) and Grüneisen parameter in various oxides [6].

3.1.3 The Substitution Effect in Lanthanum Molybdate

Even though $La_2Mo_2O_9$ has low thermal conductivity, it undergoes structural transition from the low-temperature monoclinic α-phase to the high-temperature cubic β-phase around

853K, which limits the practical use of $La_2Mo_2O_9$ as an application. In recent years, it has been reported that adequate substitutions of K^+, Rb^+, Dy^{2+}, Ca^{2+}, Sr^{2+}, Ba^{2+}, Bi^{3+}, Sm^{3+}, Gd^{3+}, Y^{3+}, and Er^{3+} at the La^{3+} site can suppress the α-β phase transition and stabilize the β-phase at room temperature [7-14].

It is worth noting that the elemental substitution is expected to reduce the thermal conductivity by phonon-defect scattering, resulting in improving efficiency of application. Based on Klemens's perturbation theory, the phonon-defect scattering rate is an increasing function of the difference in mass between the gest atoms (M_{guest}) and the host atoms (M_{host}); $|M_{host} - M_{guest}|$. Therefore, significant reduction of thermal conductivity can be expected in case the substituted atom has heavier (or lighter) mass and causing additional phonon scattering sources. Figure 3.4 shows the mass different between La atom (M_{La}) and various kinds of substitution atom (M_x) preventing phase transition versus solubility limit. As shown in Fig. 3.4. Phonon scattering rate due to point-defect is enhanced with increasing mass different and concentration of defects. On the other hands, phonon scattering rate is weakened by decreasing mass different between impurity atom and La atom. Instead, effect of other scattering process become clearer.

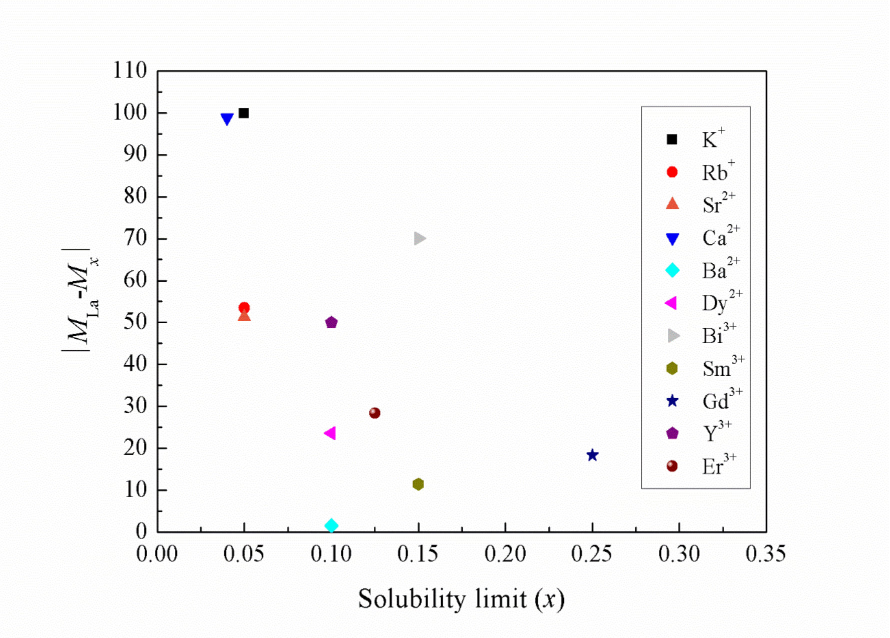

Figure 3.4 Mass difference between La atom and various kinds of substitution atom preventing phase transition – solubility limit relationship.

3.1.4 The Ba Substitution Effect in Lanthanum Molybdate

Vacancies is one of the most powerful phonon scattering sources due to the difference between the mass and nearest-neighbor force constants of the host ion and vacancy. If trivalent La^{3+} is substituted by a divalent cation, vacancies can be generated in $La_2Mo_2O_9$ to achieve charge balance. As shown in Fig. 3.4, substitution of La in $La_2Mo_2O_9$ by divalent cations such as Ca, Sr, and Ba is expected to suppress the phase transition and reduce the thermal conductivity. As long as mass difference of atomic small, effect of oxygen on reducing thermal conductivity can be easily captured. Thus, we selected Ba as a substitutional atom due to small mass difference comparing with La atom and its relatively high solubility limit. Additional reduction might be possible by adapting concepts of oxygen vacancies. The objective of this section is to reduce thermal conductivity down to minimum thermal conductivity (0.48 W/mK at 300K) (see Fig. 3.5). The detail about the calculation of lower limit of the thermal conductivity will be discussed later in chapter IV. The elastic properties and Debye temperature were also evaluated because those factors are closely related to the thermal properties. To assess the thermal conductivity, accurate thermodynamic data are required, including the specific heat capacity at constant pressure and thermal diffusivity. The specific heat capacity at constant pressure of $La_2Mo_2O_9$ was measured using differential scanning calorimetry. The thermal diffusivity was measured by laser flash method. The thermal conductivity was calculated from the measured thermal diffusivity, heat capacity, and sample density. The effect of impurity and oxygen vacancies induced by Ba substitution on thermal conductivity was analyzed using the Klemens-Callaway model.

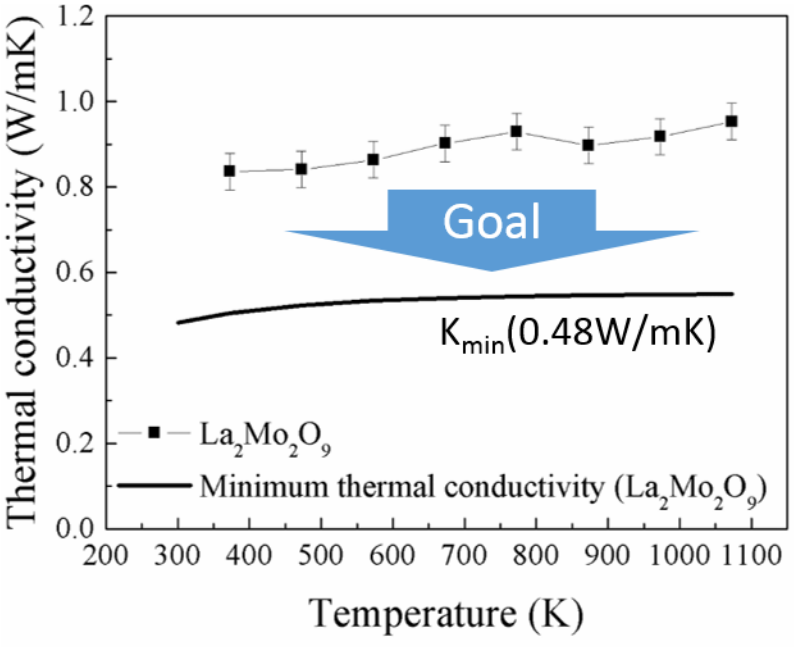

Fig. 3.5 Schematic illustration showing research objectives and major target.

3.2 Experimental Procedures

The Ba-doped $La_2Mo_2O_9$ polycrystalline materials were synthesized by conventional solid-state reactions. The powders of $(La_{1-x}Ba_x)Mo_2O_{9-\delta}$ (x= 0, 0.03, 0.06, 0.09, 0.1, and 0.12) were prepared by mixing the appropriate amounts of raw powdered materials, such as La_2O_3 (Kishida Chem., Co., 99.99%), MoO_3 (Mitsuwa Chem., Co., 99.9%), and $BaCO_3$ (Kojundo Chemical Co., 99.95%) followed by a reaction in air. The reaction will be occurred as following stoichiometrically balanced equation:

$$(1-x)La_2O_3 + 2xBaCO_3 + 2MoO_3 \longrightarrow (La_{1-x}Ba_x)_2Mo_2O_{9-\delta} + 2xCO_2 \ (x = 0-0.12) \quad (3.1)$$

To prepare the stoichiometric compounds, the raw materials were weighed, mixed and homogenized by wet ball milling and hand mixing in mortars. After homogenization, the mixed oxides were pressed into a form of discs with a die and two punches under a pressure of 100 MPa. The pellets were undermined allowed a two-step heating process: first heated to 773 K for 12 h, then reheated to 1173 K, and held at this temperature for 12 h in air. After making the single-phase powder, the powder samples were pressed into pellets under a pressure of 200 MPa, and sintered at 1373 K for 6 h in air.

The crystal structures and phase and phase compositions were evaluated by powder XRD analysis using Cu-Kα radiation and a semiconductor detector. In order to reduce thermally induced changes in the sample position, parallel beam optics was used. The measurements were carried out in the temperature range from room temperature to 1073 K by means of infrared heating under a hydrogen atmosphere. The condition of scan rate was 2^{o}/min with a step size of 0.02 degree. In order to reduce systematic error, NIST Si powder was used for angular calibration. The lattice parameters were obtained by diffraction peaks at 2θ values between 20^{o} and 80^{o} using the PDXL software. The temperature dependent lattice parameters were used to obtain thermal expansion coefficients. The bulk density of the samples was determined by the geometric measurement.

In order to evaluate the elastic moduli and Debye temperature. The longitudinal sound velocity (v_L) was measured by the ultrasonic pulse-echo method using the Nihon Matech Echometer 1062 at room temperature in air. The transverse sound velocity (v_S) was calculated as follows:

$$v_S = \frac{v_L}{\sqrt{3}} \tag{3.2}$$

The longitudinal sound velocity of iron was measured and compared with the literature [15]. The difference between was less than 0.4%. While changing the position of sample, the measurements were performed three times. The standard deviation of velocity was within 34 m/s.

The specific heat capacity at constant pressure was measured by a differential scanning calorimeter (DSC; Jupiter, NETZSCH) in the temperature range from 300 to 1073 K under high-purity argon flowing at 30 mL/min. The measurement condition for samples were held isothermally for 40 min at 313 K (initial temperature) and then heated at a rate of 10 K/min up to 1073 K. The uncertainty for experimental was estimated by the standard deviation of three measurements at a given temperature. The maximum standard deviation was less than 4%. The thermal diffusivity was measured three times at each temperature from 300 to 1073 K by the laser-flash method using LFA 457 MicroFlash instrument (NETZSCH). The thermal diffusivity of a standard graphite sample was measured as a function of temperature and compared with NMIJ RM 1201-a. The deviations between these values were less than 3%. The thermal conductivity was calculated from the results of the heat capacity, thermal diffusivity, and sample density. The uncertainty of the thermal conductivity was obtained from the uncertainty of the heat capacity, thermal diffusivity, and sample density.

3.3 Results and Discussion

As mentioned in section 3.1.3, Pure $La_2Mo_2O_9$ has two phases: a low-temperature monoclinic α-phase and a high temperature cubic β-phase. The phase transition occurs at approximately 853 K. The crystal structure of α-$La_2Mo_2O_9$ is a slightly distorted β-phase; the additional reflections caused by this distortion are small deviation within 0.5°. Thus, all XRD patterns of $La_2Mo_2O_9$ were compared to the literature peak positions of the β-phase (JSPDS #0-028-0509).

Figure 3.6 shows the powder XRD patterns of $(La_{1-x}Ba_x)_2Mo_2O_{9-\delta}$ with barium contents of x = 0, 0.03, 0.06, 0.09, 0.1, and 0.12. As shown in Fig. 3.6, single phase (β-phase) compounds were obtained for $(La_{1-x}Ba_x)_2Mo_2O_{9-\delta}$ for $0 \leq x \leq 0.09$ and correspond to the literature peak position of $La_2Mo_2O_9$ (JSPDS #0-028-0509). In contrast, $(La_{1-x}Ba_x)_2Mo_2O_{9-\delta}$ with $0.1 \leq x \leq 0.12$ exhibits a small peak at $2\theta = 26.68^\circ$, corresponding to $BaMoO_4$ (JCPDS #29-0193), indicating that the solubility limit of Ba is between 0.09 and 0.1. This result indicates that the maximum solubility of Ba^{2+} doping in the sub-lattice of La^{3+} in $La_2Mo_2O_9$ is between 9 and 10mol%, which agrees well with the published data [8].

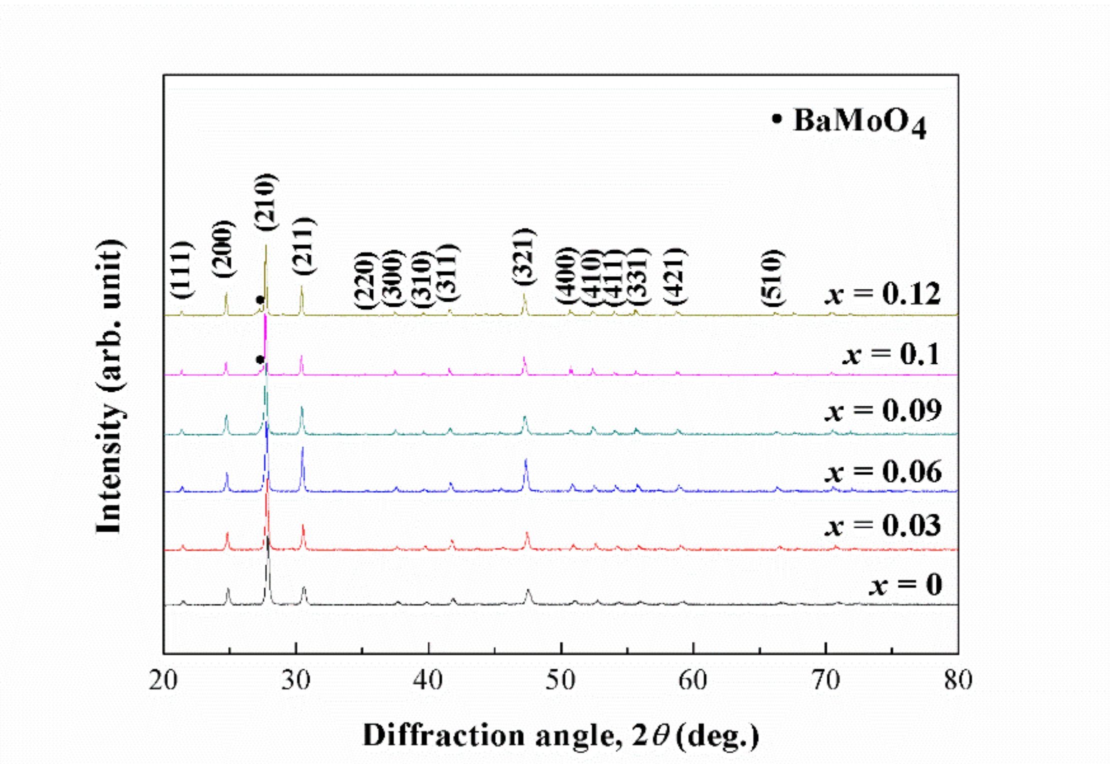

Figure 3.6 Room temperature XRD patterns of $(La_{1-x}Ba_x)_2Mo_2O_{9-\delta}$,

Figure 3.6 shows XRD patterns of Ba doped $La_2Mo_2O_9$ compound as a function of temperature. There are no impurity peaks in the high-temperature XRD patterns of any of the samples. This results is different as compared to Selmi et al [16]. They observed that Ba-doped $La_2Mo_2O_9$ compounds are likely to decompose upon heating. And they showed that $(La_{1-x}Ba_x)_2Mo_2O_{9-\delta}$ with x = 0.075 decomposed above 1173 K and that with x = 0.1 decomposed above 973 K, which suggests that the decomposition temperature was decreased as Ba content increase. On the other hand, in this work, the maximum Ba composition, x, was 0.09 and the maximum measurement temperature was 1073 K. This is because that maximum observed temperature is different between reported value [16] and present study: the present experimental temperature seems to be slightly lower than the decomposition temperature.

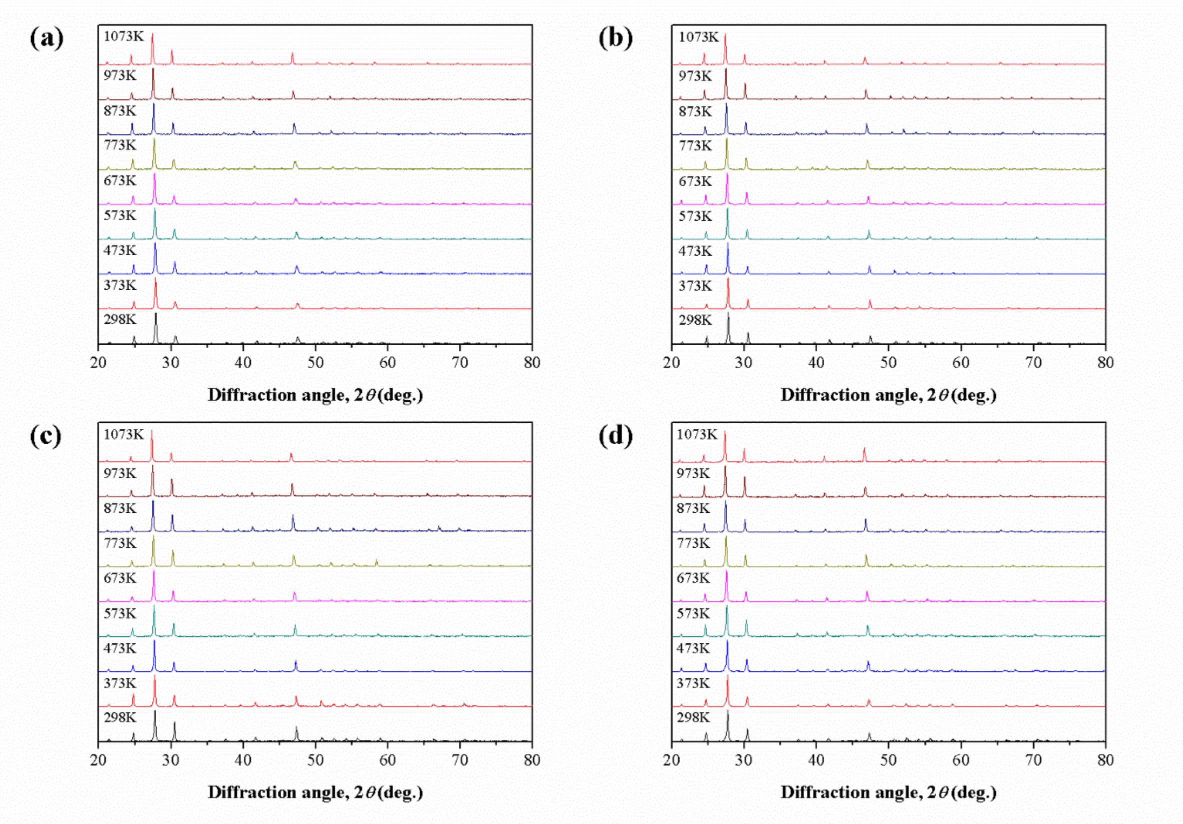

Figure 3.7 High temperature XRD patterns of $(La_{1-x}Ba_x)_2Mo_2O_{9-\delta}$ with (a) $x = 0$ (b) $x = 0.03$ (c) $x = 0.06$, and (d) $x = 0.09$.

Figure 3.7 shows the lattice constants depending on Ba content obtained at room temperature. The lattice constant (a) of non-doped $La_2Mo_2O_9$ was 0.715742(3) *nm*, which is agree well with the published data (0.71579 *nm*) [17-22]. This data is somewhat higher than those of Goutenoire and Georges [14], which were refined by considering a monoclinic structure for the low temperature α-phase via neutron diffraction. This is because that the cubic crystal structure was assumed for obtaining the lattice constant of the low temperature α-phase, in the same manner used Yan [18], due to the similarity in the crystal structure of the α- and β-phase and the limited observed resolution. The lattice constant was increased as Ba content increased up to $x = 0.1$. This tendency can be ascribed to the difference between the ionic radii of Ba^{2+} (1.47Å) and La^{3+} (1.22Å) [23]: The substitution of La^{3+} sub-lattice by Ba^{2+} results in lattice expansion. The variation of the lattice parameter by the Ba content in this work is similar to that published by Yan [18] in the case of the specimens prepared by solid state reaction, versus those published by Khaled [19] and Lopez [22], which were obtained by the sol-gel method.

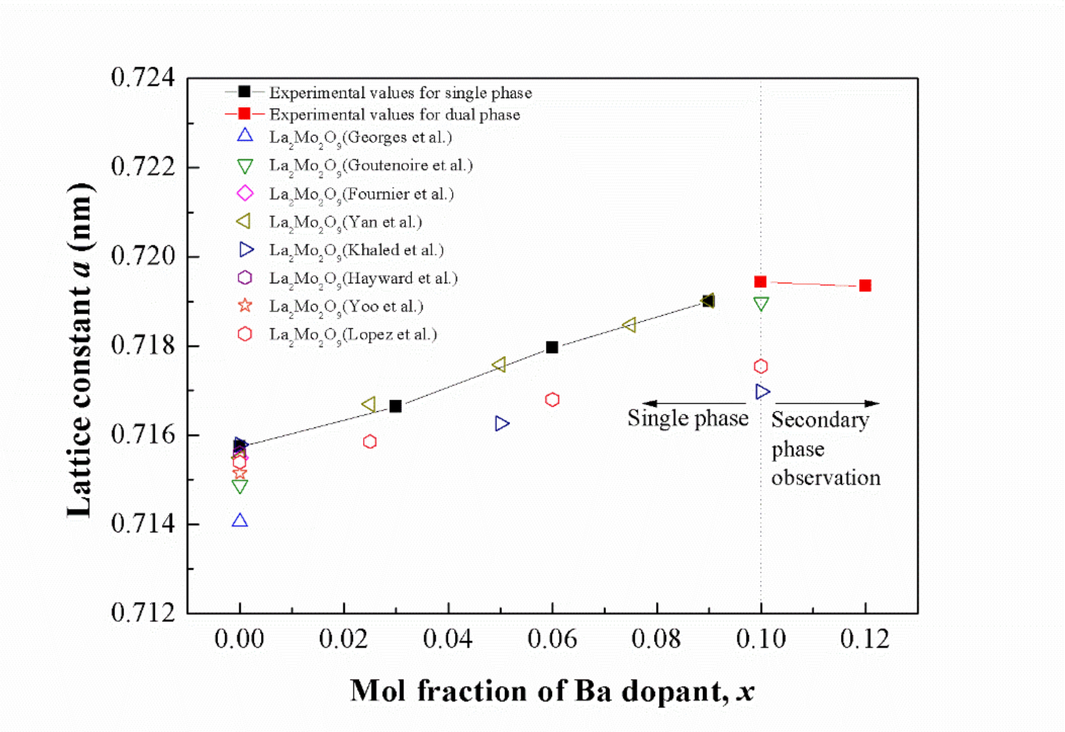

Figure 3.8 Lattice constants of $(La_{1-x}Ba_x)_2Mo_2O_{9-\delta}$ compounds as a function of Ba dopant.

Figure 3.8 shows the temperature dependence of the lattice constants of $(La_{1-x}Ba_x)_2Mo_2O_{9-\delta}$ compounds. The lattice constants of $(La_{1-x}Ba_x)_2Mo_2O_{9-\delta}$ were fitted by linear equations by the weighted least-squares method. The temperature dependent lattice constants of $La_2Mo_2O_9$ was slightly more pronounced than published by Hayward [20] on the basis of the pseudocubic phase at all temperatures. This is because that an error in 2θ for the indexed peaks, used to obtain the lattice constant as a function of temperature, resulting in an error in the lattice constant. Within the uncertainties of the value, the results in this work agrees well with reported data by Corbel [14] and Yan [18]. The lattice constant of the $La_2Mo_2O_9$ sample was changed suddenly near 850 K. This tendency is due to phase transformation (α to β phase). Data fitting has to be performed separately in the two temperature ranges from 298 to 773K and from 873 to 1073 K to evaluate the temperature dependence of the lattice constant of the $La_2Mo_2O_9$. The empirical equations for the temperature dependent lattice constant are expressed as:

$$a_{Ba:0}(T) = 7.123\ (2) \times 10^{-1} + 1.10\ (4) \times 10^{-5}\mathrm{T}\ \ \text{(nm) (298K < T < 773 K)} \qquad (3.3)$$

$$a_{Ba:0}(T) = 7.074\ (3) \times 10^{-1} + 1.79\ (3) \times 10^{-5}\mathrm{T}\ \ \text{(nm) (873K < T < 1073 K)} \qquad (3.4)$$

$$a_{Ba:0.03}(T) = 7.120\ (3) \times 10^{-1} + 1.41\ (5) \times 10^{-5}\mathrm{T}\ \ \text{(nm) (298K < T < 1073 K)} \qquad (3.5)$$

$$a_{Ba:0.06}(T) = 7.135\ (3) \times 10^{-1} + 1.37\ (5) \times 10^{-5}\mathrm{T}\ \ \text{(nm) (298K < T < 1073 K)} \qquad (3.6)$$

$$a_{Ba:0.09}(T) = 7.149\ (2) \times 10^{-1} + 1.30\ (3) \times 10^{-5}\mathrm{T}\ \ \text{(nm) (298K < T < 1073 K)} \qquad (3.7)$$

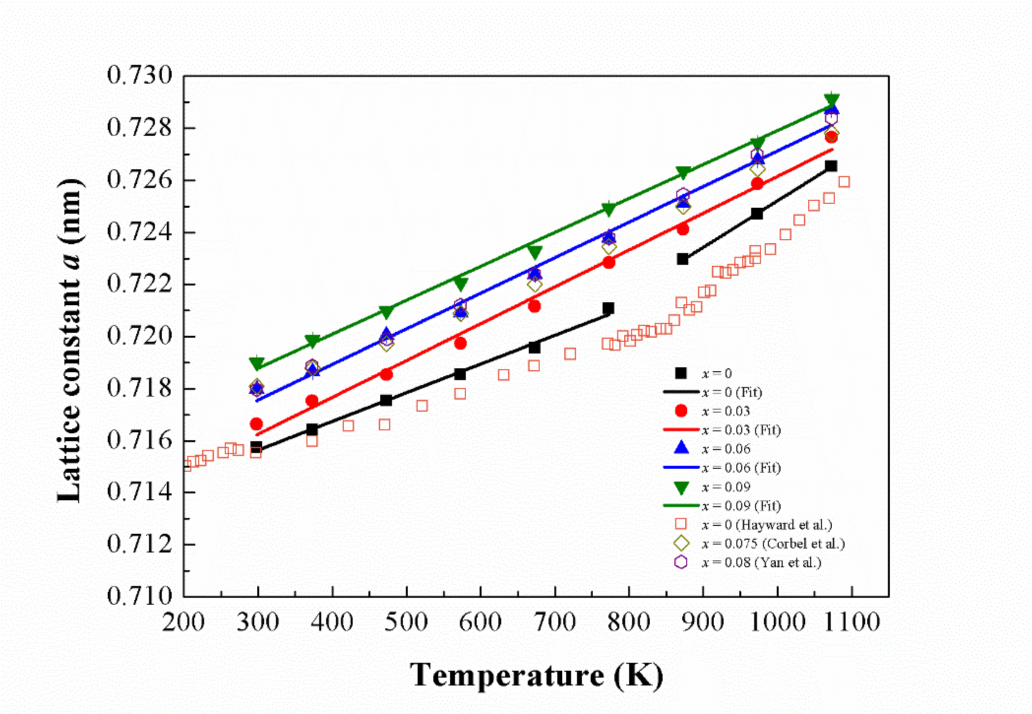

Figure 3.9 Lattice constants of $(La_{1-x}Ba_x)_2Mo_2O_{9-\delta}$ as a function of temperature.

Figure 3.9 shows the linear thermal expansion coefficient of $(La_{1-x}Ba_x)_2Mo_2O_{9-\delta}$ determined by Eq. (3.3-3.7). The linear thermal expansion coefficient (α_l) of a given lattice constant (a) can be expressed by

$$\alpha_l = (1/a_0)\frac{da}{dT} \tag{3.8}$$

where a_0 is the lattice constant at room temperature. The α_l of α-$La_2Mo_2O_9$ is 15.36 (11) × 10^{-6} K^{-1} over the temperature range from room temperature to 773 K as shown in Fig. 3.10. This value is in agreement with reported values [9,24]. The α_l of β-$La_2Mo_2O_9$ is 24.71 (12) × 10^{-6} K^{-1} in the temperature range from 873 to 1073 K. This value is within the range expected for the high-temperature β-phase form [9,20,24], which is range from 14.1 × 10^{-6} K^{-1} to 31.0 × 10^{-6} K^{-1} in different temperature ranges. The α_l of β-$La_2Mo_2O_9$ is similar with reported value by Hayward [20]. The α_l of Ba-doped $La_2Mo_2O_9$ were somewhat higher than that of non-doped $La_2Mo_2O_9$. According to Lopez [22] and Yan [18], the α_l of Ba-doped $La_2Mo_2O_9$ was increased with Ba content. The α_l of Ba-doped $La_2Mo_2O_9$ in present study are close to that published by Yan [18].

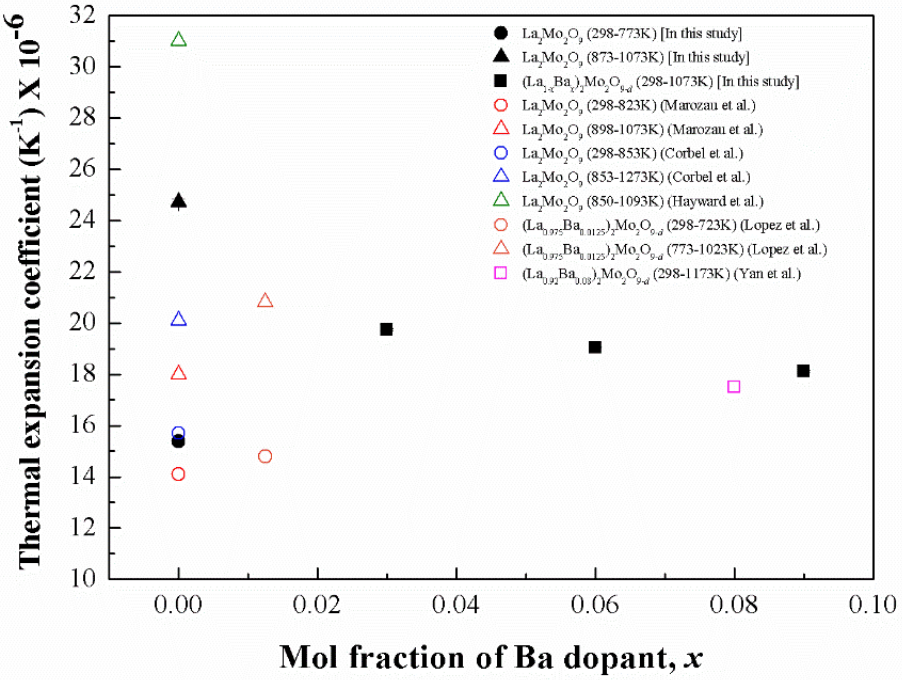

Figure 3.10 Average thermal expansion coefficient of $(La_{1-x}Ba_x)_2Mo_2O_{9-\delta}$ as a function of Ba dopant.

3.3.1 Elastic properties

The elastic properties such as bulk modulus (B), shear modulus (G), Young's modulus (E), compressibility (β), and Debye temperature (θ_D) were calculated by obtained longitudinal sound velocity (v_L) and shear sound velocity (v_S) as following:

$$G = \rho V_S^2 \tag{3.9}$$

$$E = \frac{G[3V_L^2-4V_S^2)}{V_L^2-V_S^2} \tag{3.10}$$

$$B = \rho\left(V_L^2 - \frac{4}{3}V_S^2\right) \tag{3.11}$$

$$\beta = \frac{1}{B} \tag{3.12}$$

$$\theta_D = \left(\frac{h}{k_B}\right)\left(\frac{9N}{4\pi V_C}\right)^{\frac{1}{3}}\left(\frac{1}{V_L^3}+\frac{2}{V_S^3}\right)^{-1/3} \tag{3.13}$$

The obtained sound velocities and elastic properties are summarized in Table 3.1. The measured sound velocities and calculated elastic properties was decreased monotonically as Ba content increase except for compressibility (β), which is increased with increasing Ba content. When $x = 0.09$, values of B, G, and E were decreased by 10% and value of θ_D was decreased by 3%. However, the β was increased by 3%. This tendency is related to lattice expansion because the elastic moduli is inversely proportional to the interatomic distance. According to references [25-27], elastic moduli of ceramic compounds (e.g., ZnO, CeO_2, hydroxyapatite) can reduced due to the formation of defects and they contribute to expand lattice. Thus the reduction in the elastic moduli can be ascribed to lattice expansion by Ba content. The obtained values were used for calculation of the heat capacity and thermal conductivity.

Table 3.1 Physical properties of sintered Ba-doped $La_2Mo_2O_9$.

Ba doping level, (mol%)	Longitudinal sound velocity, V_L (m/s)	Shear sound velocity, V_S (m/s)	Bulk modulus, B (GPa)	Shear modulus, G (GPa)	Young's modulus, E (GPa)	Compressibility, β (GPa^{-1})	Debye temperature, θ_D (K)
0	4447±34	2567	55.69±0.86	33.41±0.52	83.54±1.30	0.0180±0.0003	351.8±2.7
3	4426±15	2555	54.33±0.36	32.60±0.22	81.49±0.54	0.0184±0.0001	349.2±1.2
6	4403±22	2542	52.63±0.52	31.58±0.31	78.94±0.78	0.0190±0.0002	346.7±1.7
9	4340±12	2506	50.63±0.27	30.38±0.16	75.95±0.41	0.0192±0.0001	341.3±0.9

3.3.2 Thermal properties

Figure 3.11 shows the temperature dependent specific heat capacity of $(La_{1-x}Ba_x)_2Mo_2O_{9-\delta}$ at constant pressure (C_p) in the temperature range from room temperature to 1073 K. The C_p of $La_2Mo_2O_9$ was slightly higher than the published value [28]. As shown in Fig. 3.11, when $x = 0$, a sharp peak was observed at 850 K. This result represents the phase transformation (α to β-phase). On the contrary, there is no evident endothermic peak in the sample with $0.03 \leq x \leq 0.09$. These results indicate that phase transition was prevented by Ba content and Ba^{2+} dopant is suitable for β-cubic phase at room temperature. This can be demonstrated by lattice degrees of freedom at La site, indicated as the values of the average cation-oxygen distance: <La-O>. In Fig. 3.12(a), the oxygen coordination around La is schematically presented for β-phase: La is surrounded by 15 oxygens and the value of average <La-O> interatomic distance is 2.66 Å (see Fig. 3.12(c)) [29]. On the other hand, in Fig. 3.12(b), La has a coordination shell including between 6 and 12 oxygen atoms, with 30 out of the 48 independent La being 9-coordinate [30]. The value of average <La-O> interatomic distance should be smaller than 2.61 Å in α-phase. This is because that unit cell volume of α-phase (366.5 $Å^3$) is ~2% smaller than that of β-phase (373.5 $Å^3$). Thus, the La-O polyhedral volume of α-phase is ~2% smaller than that of β-phase because La-O polyhedral volume is dependent upon the unit cell volume. For this reason, the value of average <La-O> interatomic distance in α-phase would be 1.21 Å (see Fig. 3.12(d)). This value is almost similar with ionic size of La^{3+} (1.22 Å) with a coordination number of 9, which means La^{3+}

is suitable for α-phase stabilized foam at room temperature. On the contrary, the value of average <La-O> interatomic distance (1.26 Å) in β-phase is larger than ionic size of La^{3+} (1.22 Å). Hence, a bigger ion ought to occupy more space than a La^{3+} (1.22 Å) and consequently replacement of Ba^{2+} (1.47 Å) with a coordination number of 9 for smaller one results in stable lattice. This result suggests that LM structure due to barium substitution results in the stabilization of the β-cubic phase.

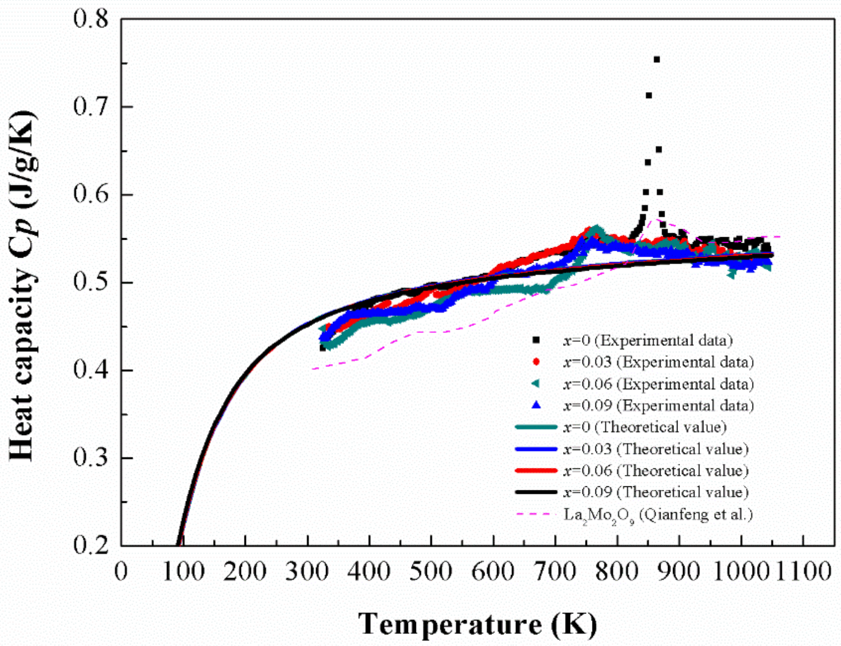

Figure 3.11 Specific heat capacity at constant pressure of $(La_{1-x}Ba_x)_2Mo_2O_{9-\delta}$ as a function of temperature.

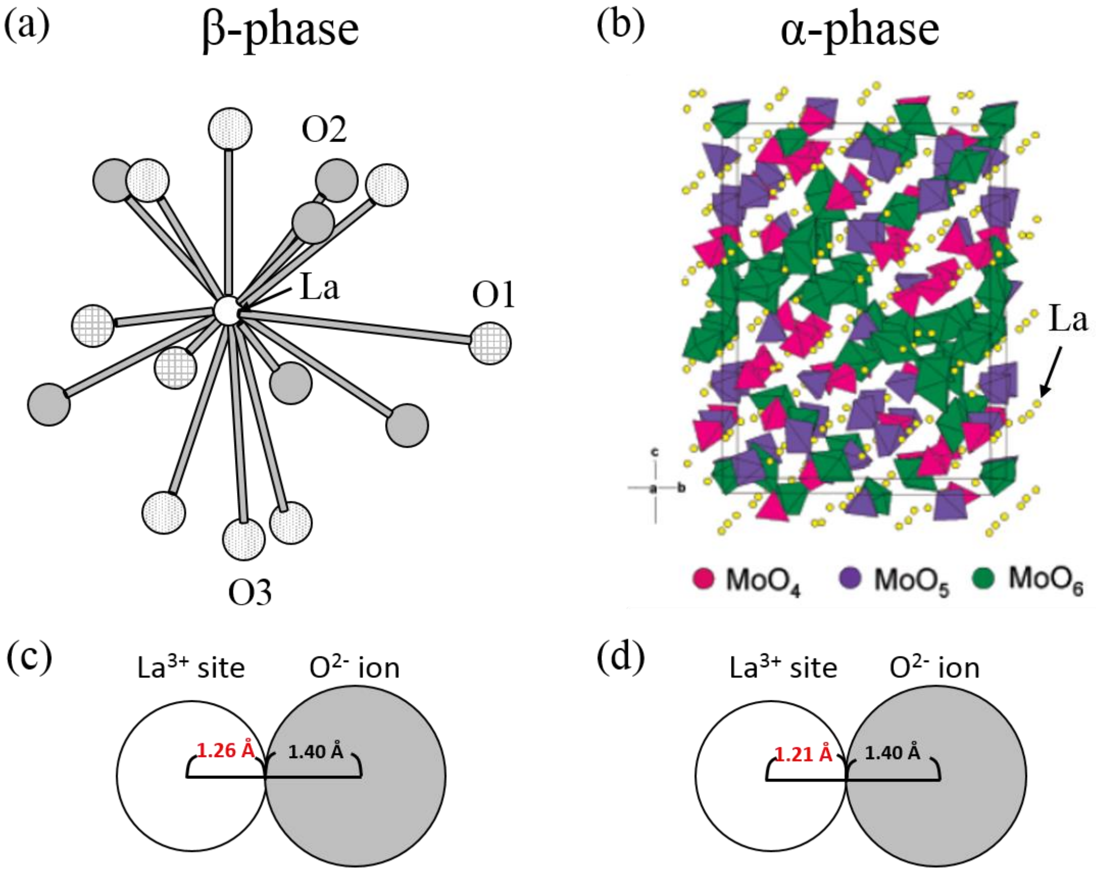

Figure 3.12 (a) Oxygen coordination around La in β-phase [29], (b) Polyhedral representation of α-phase: tetrahedral groups (pink), trigonal bipyramidal (purple), octahedral (green) [30], (c) estimated average La-O interatomic distance for α-phase, and (d) average La-O interatomic distance β-phase.

Theoretical calculations were performed to examine the validity of the measured C_p using obtained values (e.g., α_l, β, θ_D). The temperature dependent C_p of $(La_{1-x}Ba_x)_2Mo_2O_{9-\delta}$ were calculated by the following equations:

$$C_P = C_V + C_d \tag{3.14}$$

$$C_V = 9nk_B \left(\frac{T}{\theta_D}\right)^3 \int_0^{\theta_D/T} \frac{x^4 e^x}{(e^x - 1)^2}\, dx \tag{3.15}$$

$$C_d = \frac{(3\alpha_l)^2 V_m T}{\beta} \tag{3.16}$$

where C_v is the lattice vibrational component of the specific heat at constant volume, Cd is the dilatational term, n is the number of atoms per molecule, and V_m is the molar volume. The calculated C_p values of $(La_{1-x}Ba_x)_2Mo_2O_{9-\delta}$ agree well with the experimental values, indicating that the measured data are reasonable.

Figure 3.13 shows the thermal conductivity of fully dense $(La_{1-x}Ba_x)_2Mo_2O_{9-\delta}$ as a function of temperature. The thermal conductivity was corrected to 100% of the theoretical density by the Maxwell relation because the density of each sample was different: relative densities of the samples were 92, 90, 89, and 88% of the theoretical density for the sample with x = 0, 0.03, 0.06, and 0.09, respectively. Such that:

$$\kappa_{dense} = \kappa_{measured} \frac{1}{(1-1.5\emptyset)} \tag{3.17}$$

where ϕ is the porosity in sample, κ_{dense} is the corrected thermal conductivity, and κ_{dense} is the measured thermal conductivity. The measured thermal conductivity of $La_2Mo_2O_9$ is in agreement with published values [1,31]. The thermal conductivity has almost temperature independent behavior over the entire temperature range from 373 to 1073 K.

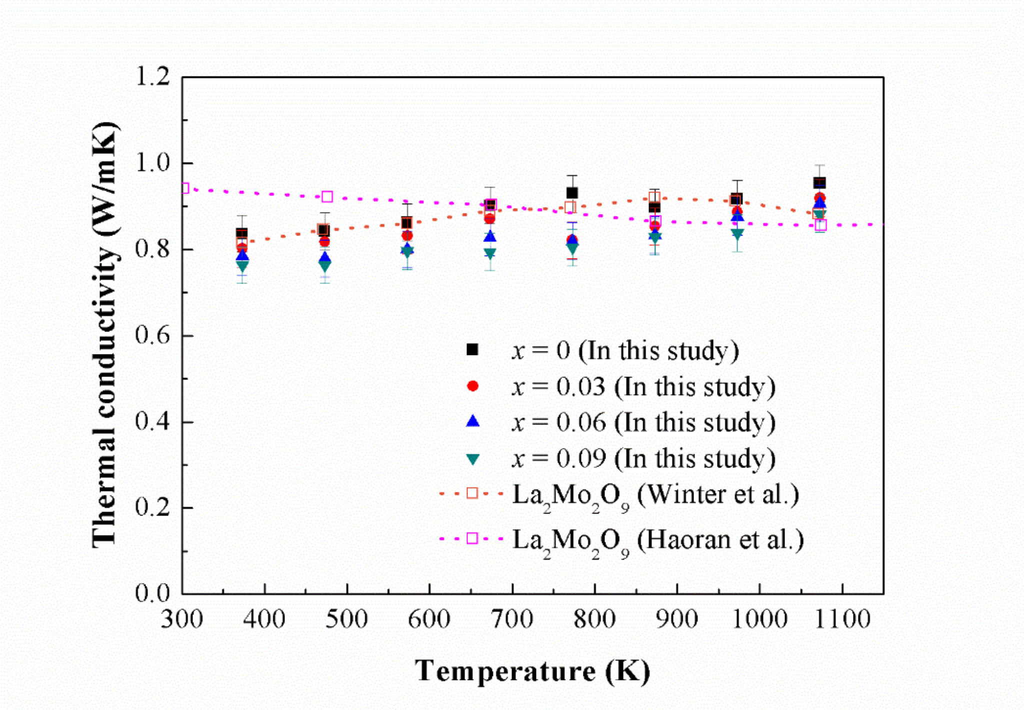

Figure 3.13 Temperature dependence of the thermal conductivity of the $(La_{1-x}Ba_x)_2Mo_2O_{9-\delta}$.(The error bars reflect an experimental uncertainty of ±5% in the thermal conductivity).

Figure 3.14 shows the compositional dependent thermal conductivity of $(La_{1-x}Ba_x)_2Mo_2O_{9-\delta}$. The thermal conductivity was decreased as Ba substitution increases in the measurement temperature range. The thermal conductivity at 373 K declined to 0.76 W $m^{-1}K^{-1}$ at x = 0.09. This value is 9% lower than that of $La_2Mo_2O_9$ (0.84 W $m^{-1}K^{-1}$). The reduction in thermal conductivity is considered to be caused by enhanced phonon scattering by point defects; Ba^{2+} atoms and oxygen vacancies. In order to evaluate the effect of these point defects on thermal conductivity, we build the empirical thermal conductivity model based on Klemens-Callaway model. Assuming that all phonon scattering processes are represented by frequency dependent relaxation times, thermal conductivity by phonon was expressed as following equations:

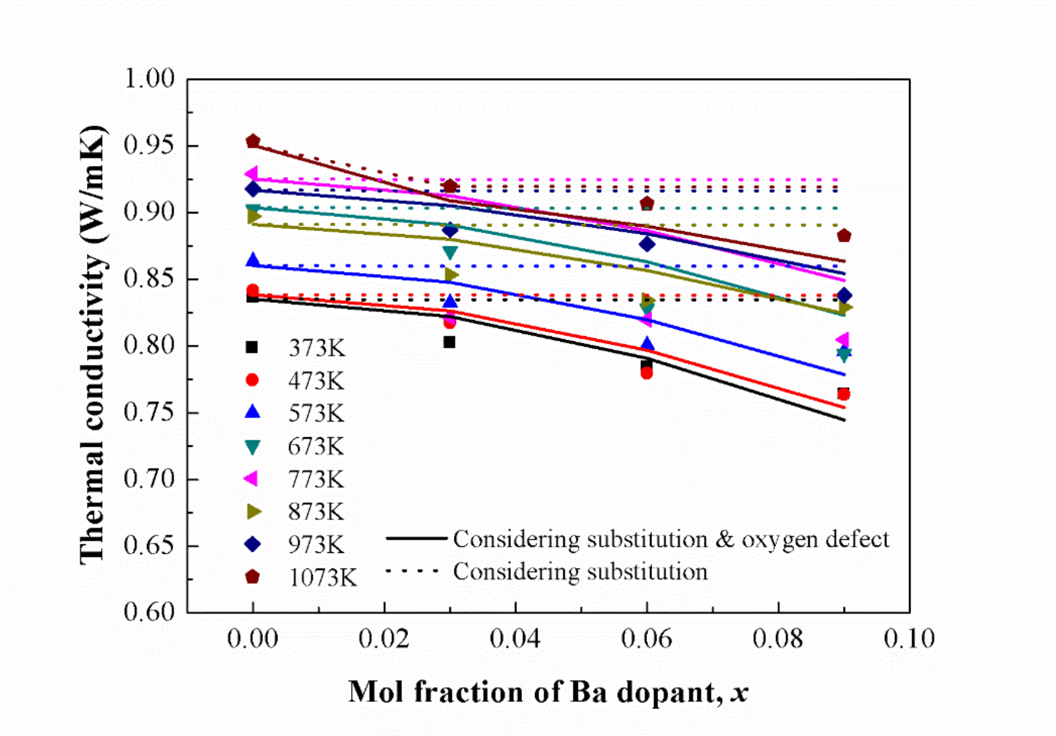

Figure 3.14 Estimated and measured thermal conductivity of $(La_{1-x}Ba_x)_2Mo_2O_{9-\delta}$ as a function of the Ba dopant at various temperature.

$$\kappa = \frac{k_B}{2\pi^2 v_B}\int_0^{k_B\theta/\hbar} \tau_{total}\left(\frac{\hbar\omega}{k_B T}\right)^2 \frac{exp(\hbar\omega/k_B T)}{[exp(\hbar\omega/k_B T)-1]^2}\omega^2 d\omega \tag{3.18}$$

where $\hbar$ is the Planck constant divided by 2π, ω is the phonon frequency, v_B is the phonon velocity, and θ is the cut-off temperature. The parameter, θ is derived from the angular frequency at the boundary of the first Brillouin zone, ω_{max}, by:

$$\theta = \frac{\hbar\omega_{max}}{k_B} \tag{3.19}$$

Under the Debye approximation, ω_{max} is given by:

$$\omega_{max} = v_B \frac{\pi}{d} \tag{3.20}$$

where *d* is the equivalent atomic separation of an isotropic medium, which can be determined from $d = \pi(6\pi^2/V)^{-1/3}$ in the Debye model. The parameter *V* represents the volume of a $La_2Mo_2O_9$ molecule.

The combined relaxation time, τ_{total}, is defined by:

$$\tau_{total}{}^{-1} = \tau_P{}^{-1} + \tau_U{}^{-1} \tag{3.21}$$

$$\tau_P{}^{-1} = A\omega^4 \tag{3.22}$$

$$\tau_U{}^{-1} = BT\omega^2 \exp(-\theta/3T) \tag{3.23}$$

where *A* and *B* are parameters described below; τ_P and τ_U are the relaxation times of phonon-point-defect scattering and phonon-phonon Umklapp scattering, respectively. The *B* term is given by

$$B = \hbar\gamma^2/Mv_B^2\theta \tag{3.24}$$

where γ is the Grüneisen parameter and *M* is the average mass of an atom in the crystal, respectively. In present study, the *B* term is treated as a temperature dependent parameter because relating properties (e.g., γ, v_B) generally vary depending on temperature, and obtained the *B* parameter by fitting to the thermal conductivity of the non-doped $La_2Mo_2O_9$ at each temperature. The *A* parameter is independent of temperature and can be expressed as:

$$A = \frac{\Omega_0}{4\pi v_B^3}\Gamma \tag{3.25}$$

where Ω_0 is the average atomic volume, Γ the scattering coefficient, and x_i is the explicit concentration of defects. For a compound composed of a single sublattice and vacancies, Γcan be expressed based on Klemens theory:

$$\Gamma = \sum_i x_i\,(1 - x_i)\left[\left(\frac{M_i - M}{M}\right)^2 + \left(\frac{2M + M_{oxygen}}{M}\right)^2\right] \tag{3.26}$$

where M_i is the atomic mass of the Ba atoms, M is the average atomic mass, M_{oxygen} is the atomic mass of oxygen atom, and *m* is the number of oxygen vacancies per solute. This equation means that the point-defect scattering arises from differences in atomic mass. The terms 2*M* and M_{oxygen} in the numerator describe the potential energy perturbation of the missing links at the vacancy and missing kinetic energy of the missing atom.

The calculation of the scattering coefficient for a compound composed of several sublattices is more complicated. For a ternary compound composed of three sublattices $U_{x_1}, V_{y_1}, W_{z_1}$, which corresponds to $(La_{1-x}Ba_x)_2Mo_2O_{9-\delta}$, Γ is given by [32]:

$$\Gamma = \frac{x_1}{(x_1+y_1+z_1)}\left(\frac{\bar{M}_U}{\bar{M}}\right)^2 \Gamma_M(U) + \frac{y_1}{(x_1+y_1+z_1)}\left(\frac{\bar{M}_V}{\bar{M}}\right)^2 \Gamma_M(V) + \frac{z_1}{(x_1+y_1+z_1)}\left(\frac{\bar{M}_W}{\bar{M}}\right)^2 \Gamma_M(W) \quad (3.27)$$

where $\overline{M_U}$, $\overline{M_V}$, and $\overline{M_W}$ are average masses at the U-, V-, and W-sites, respectively. $\bar{M}$ is the total average atomic mass. Γ_M represents the scattering strength caused by the mass for each site and can be written as:

$$\Gamma_M = \frac{\sum_i f_i(M_i-\overline{M_J})^2}{\left(\overline{M_J}\right)^2} \quad (3.28)$$

where f_i is the fractional concentration of the corresponding defect type and j is the index of U-, V-, or W- for the different lattice sites. In the calculation of $(La_{1-x}Ba_x)_2Mo_2O_{9-\delta}$, two types of defects were considered: oxygen vacancies and substituted Ba^{2+}. Since the oxygen defects are generated for charge balance and *Mo* cannot adopt a higher oxidation state than 6+, we assume that δ is equal to x. The theoretical thermal conductivities conform well to the trend of measured thermal conductivity. The difference between estimated and measured values is within 11%.

In Fig. 3.14, the solid lines and dotted lines represent the effect of oxygen vacancies and changes in mass perturbation due to Ba substitution, respectively. The reduction in the thermal conductivity due to Ba doping effect is quite small as compared to oxygen vacancies effect, suggesting that the reduction of the thermal conductivity by Ba substitution is mainly attributed to the phonon-oxygen vacancies scattering while changes in mass perturbation due to Ba substation can be neglected.

3.4 Conclusions

The effect of Ba doping on the thermal and elastic properties of $La_2Mo_2O_9$ was studied. Dense samples of Ba-substituted $La_2Mo_2O_9$ ($(La_{1-x}Ba_x)_2Mo_2O_{9-\delta}$, x = 0–0.12) were prepared by a conventional solid-state reaction. XRD measurements indicate that the solubility limit was slightly above x = 0.09. The α_l was evaluated by high-temperature XRD measurements, and the results showed that Ba substitution reduced the α_l. DSC measurements demonstrated that the phase transition from the α- to β-phase was suppressed even in the case where the Ba content was as low as x = 0.03. The measured v_L, v_s, and calculated elastic properties, such as B, G, E, and θ_D decreased monotonically as Ba content increase. With increasing Ba concentration, the thermal conductivity of Ba-doped $La_2Mo_2O_9$ was decreased. To satisfy the charge balance, oxygen vacancies are generated in $La_2Mo_2O_9$ when trivalent La^{3+} is substituted by divalent Ba^{2+}. Phonon scattering by the oxygen vacancies was estimated via perturbation theory on the basis of the missing mass and linkages. Theoretical estimations based on the Klemens–Callaway model revealed that the reduction of the thermal conductivity is mainly attributed to enhanced phonon scattering caused by oxygen vacancies.

3.5 References

[1] N.R. Winter, D.R. Clarke, *J. Am. Ceram. Soc.* **90** 533 (2007).

[2] F. Goutenoire, O. Isnard, R. Retoux, P. Lacorre, *Chem. Mater.* **12**, 2575 (2000).

[3] E.S. Toberer, A. Zevalkink, G.J. Snyder, *J. Mater. Chem.* **21** 15843 (2011).

[4] D.T. Morelli, V. Jovovic, J.P. Heremans, *Phys. Rev. Lett*. **101** 035901 (2008).

[5] E.J. Skoug, D.T. Morelli, *Phys. Rev. Lett*. **107** 235901 (2011).

[6] Y. Wang, F. Yang, P. Xiao, *Appl. Phys. Lett*. **102** 141902 (2013).

[7] S. Georges, F. Goutenoire, F. Altorfer, D. Sheptyakov, F. Fauth, E. Suad, P. Lacorre, *Solid State Ionics* **161** 231 (2003).

[8] R. Subasri, D. Matusch, H. Nafe, F. Aldinger, *J. Eur. Ceram. Soc.* **24** 129 (2004).

[9] I.P. Marozau, D.M. López, A.L. Shaula, V.V. Kharton, E.V. Tsipis, P. Núñez, J.R. Frade, *Electrochim. Acta.* **49** 3517 (2004).

[10] C. Tealdi, G. Chiodelli, L. Malavasi, G. Flor, *J. Mater. Chem.***14** 3553 (2004).

[11] F. Goutenoire, O. Isnard, E. Suard, O. Bohnke, Y. Laligant, R. Retoux, P. Lacorre, *J. Mater. Chem.***11** 119 (2001).

[12] T. He, Y. Huang, Q. He, Y. Ji, L. Pei, J. Liu, Z. Lu, *J. Alloys Compd.* **338** 145 (2005).

[13] J. Yang, Z. Gu, Z. Wen, D. Yan, *Solid State Ionics* **176** 523 (2005).

[14] G. Corbel, Y. Laligant, F. Goutenoire, E. Suard, P. Lacorre, *Chem. Mater.* **17** 4678 (2005).

[15] D.R. Lide, *CRC Handbook of Chemistry and Physics*, 71 ed. Boston, CRC Press, pp. 1990-1.

[16] A. Selmi, C. Galven, G. Corbel, P. Lacorre, *Dalton Trans*. **39** 93 (2010).

[17] J.P. Fournier, J. Fournier, R. Kohlmuller, *Bull. Soc. Chim. Fr.* **12** 4277 (1970).

[18] B. Yan, M. Li, J. Zhang, K.C. Chou, *Res. Bull.* **45** 382 (2010).

[19] A. Khaled, J.J. Pireaux, S. Khelili, *Acta Chim. Slov.* **59** 766 (2012).

[20] S.A. Hayward, S.A.T. Redfern, *J. Phys. Condens. Matter.* **16** 3571 (2004).

[21] K.S. Yoo, A.J. Jacobson, *J. Mater. Sci.* **40** 4431 (2005).

[22] D.M. López, D.P. Coll, J.C.R Morales, J.C. Vázquez, M.C.M Sedeño, P. Núñez, *J. Electrochim. Acta.* **52** 5219 (2007).

[23] R.D. Shannon, *Acta Cryst.* **A32** 751 (1976).

[24] G. Corbel, *Solid State Sci.* **7** 1216 (2005).

[25] K.L. Duncan, Y. Wang, S.R. Bishop, F. Ebrahimi, E.D. Wachsman, *J. Am. Ceram. Soc.* **89** 3162 (2006).

[26] B. Viswanath, V.V. Shastry, U. Ramamurty, N. Ravishankar, *Acta Mater.* **58** 4841 (2010).

[27] S.S. Bhat, U.V. Waghmare, U. Ramamurty, *Comp. Mater. Sci.* **99** 133 (2015).

[28] F. Qianfeng, W. Xianping, C. Zhijun, Z. Geoguang, *Front. Mater. Sci. China* **1** 7 (2007).

[29] C. Tealdi, L. Malavasi, C. Ritter, G. Flor, G. Costa, *J. Solid State Chem*. **181** 603 (2008).

[30] I.R. Evans, J.A.K. Howard, J.S.O. Evans, *Chem. Mater.* **17** 4074 (2005).

[31] L. Haoran, W.C. An, *J. Am. Ceram. Soc*. **98** 1385 (2015).

[32] G.A. Slack, *Phys. Rev.* **126** 427 (1962).

CHAPTER IV

Effect of Bi Substitution on Thermophysical Properties of Lanthanum Molybdate

In this chapter, the author covers an effect of substitution atom (alloying) and enhancing anharmonicity induced by lone pair electrons on the thermal conductivity in polycrystalline bulk lanthanum molybdate. The lone pair electrons were induced by Bi substituting atom. The effect of lone pair electrons on the reduction thermal conductivity was expressed using relaxation time for phonon-umklapp scattering by enhancing anharmonicity through Grüneisen parameter (γ). Each phonon scattering was clarified by combined theoretical and experimental analysis. The properties such as thermal expansion coefficient, heat capacity, elastic moduli, Debye temperature, and thermal conductivity of the compounds were studied to build empirical thermal conductivity model. The author incorporated the phonon scattering effect of substitution atom and enhancement of anharmonicity into the relaxation time. The obtained results was used for comparison of the various phonon scattering effects on thermal conductivity.

4.1 Introduction

Elemental substitution is expected to be promising to achieve a lower thermal conductivity because phonons would be scattered by additional scattering sources. In previous chapter, we investigated the effect of the partial substitution of La by Ba in $La_2Mo_2O_9$ compounds. The substituted Ba atoms induced additional phonon scattering sources: alloys and oxygen vacancies. The oxygen-vacancies were generated to compensate for the charge difference between substituted Ba^{2+} and host La^{3+}. The thermal conductivity at 300 K declined to 0.76 W m^{-1} K^{-1} at a Ba content of 9 mol%. However, further reduction in the thermal conductivity could occur because the value is higher than the lowest limit of the lattice thermal conductivity (0.48 W m^{-1} K^{-1} at 300 K), based on Cahill's model [1]. In previous chapter, since the mass difference is quite small, the phonon scattering by alloys had very little effect on reducing thermal conductivity.

To further reduce the thermal conductivity in the $La_2Mo_2O_9$ system, we focused on the anharmonicity of the bonds and lone pair electrons (LPEs), which are non-bonding valence electron pairs. Compounds with LPEs exhibit a high anharmonicity and extremely low thermal conductivity [2,3]. The high anharmonicity causes a high phonon-phonon Umklapp scattering rate, leading to a low thermal conductivity. High anharmonicity is introduced by the LPEs because the bond pair electrons and LPEs repel each other.

In the present study, we substituted Bi^{3+} dopant ions into the La^{3+} sub-lattice in $La_2Mo_2O_9$ to introduce LPEs because Bi^{3+} has $6s^2$ LPEs. To evaluate the anharmonicity in Bi-doped $La_2Mo_2O_9$, we calculated the Grüneisen parameter (γ). We measured the linear thermal expansion and sound velocity of the $(La_{1-x}Bi_x)_2Mo_2O_9$ samples to obtain the Grüneisen parameter. The thermal conductivity was evaluated using the measured thermal diffusivity, heat capacity, and density, and the results were analyzed using a modified Klemens-Callaway model with the experimentally observed Grüneisen parameter to understand the effect of anharmonicity induced by Bi doping on the thermal conductivity.

4.2 Experimental Procedures

The $(La_{1-x}Bi_x)_2Mo_2O_9$ (x=0.02-0.2) powders were synthesized via a solid-state reaction. Powders of La_2O_3 (Kishida Chemical Co., 99.99%), MoO_3 (Mitsuwa Chemical Co., 99.9%), and Bi_2O_3 (Kishida Chemical Co., 99.9%) were used as raw materials. The weighed powders were mixed by wet ball milling and subsequently pressed into pellets under 100 MPa. The pellets were heated to 773 K for 12 h, then reheated to 1173 K and held at this temperature for 24 h in air, and then naturally cooled to room temperature. To obtain dense specimens, the mixtures were ground, pressed into pellets under 200 MPa, and sintered at 1373 K for 6 h in air.

The crystal structures and phase compositions were determined by powder X-ray diffraction (XRD; ULTIMA IV, Rigaku) using Cu-Kα radiation and a scintillation detector. The data were collected in the 2θ range of 20–80° at a scan rate of 2° min^{-1} and step size of 0.02°. We used NIST Si powder (NIST SRM 640c) for angular calibration. The lattice constants of the samples were determined from the positions of the diffraction peaks based on the whole-powder-pattern decomposition method using the PDXL software package. The bulk sample density, ρ, was determined by the weight and geometric volume, and the theoretical density of each solid solution was calculated using the lattice constants obtained from the XRD measurements (see Table 4.1).

Table 4.1 Densities of theoretical, experimental, and relative and porosity for the $(La_{1-x}Bi_x)_2Mo_2O_9$ solid solutions.

Sample composition	Theoretical density (T.D.) (g cm^{-3})	Sample density (g cm^{-3})	Relative density (% T.D.)	Porosity (%)
$La_2Mo_2O_9$	5.56	5.15±0.01	92.2	7.8
$(La_{0.98}Bi_{0.02})_2Mo_2O_9$	5.57	5.01±0.04	89.9	10.1
$(La_{0.96}Bi_{0.04})_2Mo_2O_9$	5.59	4.95±0.01	88.6	11.4
$(La_{0.95}Bi_{0.05})_2Mo_2O_9$	5.60	4.95±0.01	88.4	11.6
$(La_{0.94}Bi_{0.06})_2Mo_2O_9$	5.60	4.98±0.01	88.9	11.1
$(La_{0.92}Bi_{0.08})_2Mo_2O_9$	5.62	5.10±0.01	90.8	9.2
$(La_{0.90}Bi_{0.1})_2Mo_2O_9$	5.63	5.07±0.01	90.1	9.9
$(La_{0.85}Bi_{0.15})_2Mo_2O_9$	5.69	5.03±0.01	88.4	11.6

The longitudinal (v_L) and shear (v_S) sound velocities were measured at room temperature using an ultrasonic pulse-echo method with a digital storage oscilloscope (TDS2002C, Tektronix). The systematic errors for measuring the v_L and v_S values were estimated by measuring a standard sample (iron) and comparing the obtained data with the literature values; the errors do not exceed 0.4%. Three measurements were performed for each sample at different sample positions, and the data are listed Table 4.2. The standard error is shown as an uncertainty. The values of the average sound velocity (v_B), B, and Debye temperature (θ_D) were calculated using the measured v_L and v_S values from $v_B = [(1/3)(1/v_L^3 + 2/v_S^3)]^{-1/3}$, $B = \rho[v_L^2 - (4/3)v_S^2]$, and $\theta_D = (h/k_B)(9N/4\pi \mathrm{V}_c)^{1/3}(1/v_L^3 + 2/v_S^3)^{-1/3}$, where k_B is the Boltzmann constant, h is Planck's constant, N is the number of atoms in the unit cell, and V_c is the volume of the unit cell.

Table 4.2 Physical properties of the $(La_{1-x}Bi_x)_2Mo_2O_9$ solid solutions.

x	Longitudinal sound velocity, v_S (m s^{-1})	Shear sound velocity, v_S (m s^{-1})	Bulk modulus, B (GPa)	Debye temperature, θ_D (K)
0	4399±41	2530±29	54.81±1.34	346.9±4.2
0.02	4161±15	2363±12	49.21±0.02	323.2±1.5
0.04	4101±8	2242±3	48.74±0.04	307.4±0.4
0.05	4102±3	2273±16	48.52±0.05	311.2±2.0
0.06	4095±55	2363±25	48.57±1.78	323.0±5.9
0.08	4118±3	2288±58	48.49±0.17	313.4±7.1
0.1	4142±12	2391±25	48.36±0.12	326.3±3.1
0.15	3986±3	2231±1	48.04±0.01	305.1±0.2

The LTEC was determined using a horizontal pushrod dilatometer from 300 to 1073 K with a heating rate of 5 K min^{-1} in an Ar gas flow at 100 mL min^{-1}. The LTEC was calculated from:

$$\alpha_l(T) = \frac{1}{l(T)}\frac{dl}{dT} \tag{4.1}$$

where T is the absolute temperature and l is the absolute length of the samples.

The specific heat capacity was measured using a differential scanning calorimeter (DSC; Jupiter, NETZSCH) from 300 to 1073 K in a high-purity Ar flowing at 30 mL min^{-1}. The samples were held isothermally for 40 min at 300 K and then heated at 10 K min^{-1} to 1073 K. The experimental uncertainty was estimated as the standard error of three measurements at each temperature. The maximum standard error was 4%.

Thermal diffusivities were measured using a laser flash method with an LFA 457 MicroFlash instrument (NETZSCH) from 300 to 1073 K. The thermal diffusivity of a standard graphite sample was measured as a function of temperature and compared with literature values (NMIJ RM 1201-a). The deviations between the literature and measured values did not exceed 3%. Prior to measuring the thermal diffusivity of the $(La_{1-x}Bi_x)_2Mo_2O_9$ samples, both faces of the samples were coated using a graphite spray to improve laser absorption at the front surface and to increase the emission intensity at the back surface. The measurement was performed three times at each temperature, and the uncertainty was evaluated from the standard error.

κ was calculated from the thermal diffusivity (d), heat capacity (C_p), and ρ according to $\kappa = dC_p\rho$, and its uncertainty was evaluated from the uncertainty in the density, thermal diffusivity, and heat capacity.

4.3 Results and Discussion

Pure $La_2Mo_2O_9$ has two phases: a low-temperature monoclinic α-phase and a high-temperature cubic β-phase. The phase transition occurs at approximately 853 K. The crystal structure of α-$La_2Mo_2O_9$ is a slightly distorted β-phase; the additional reflections caused by this distortion are small because of a small deviation (≤0.5°). Thus, we compared all XRD patterns of $La_2Mo_2O_9$ to the literature peak positions of the β-phase (JCPDS #0-028-0509). Figure 4.1 shows the powder XRD patterns of $(La_{1-x}Bi_x)_2Mo_2O_9$ with bismuth contents of x = 0, 0.02, 0.04, 0.05, 0.06, 0.08, 0.1, 0.15, and 0.2. Single phase (β-phase) materials are obtained for $(La_{1-x}Bi_x)_2Mo_2O_9$ for $0 \leq x \leq 0.15$ and correspond to the literature peak position of $La_2Mo_2O_9$ (JCPDS #0-028-0509). In contrast, $(La_{1-x}Bi_x)_2Mo_2O_9$ with $x = 0.2$ exhibits a small peak, 2θ = 27.3°, corresponding to Bi_2O_3 (JCPDS #01-070-8244), indicating that the solubility limit of Bi is between x = 0.15 and 0.2.

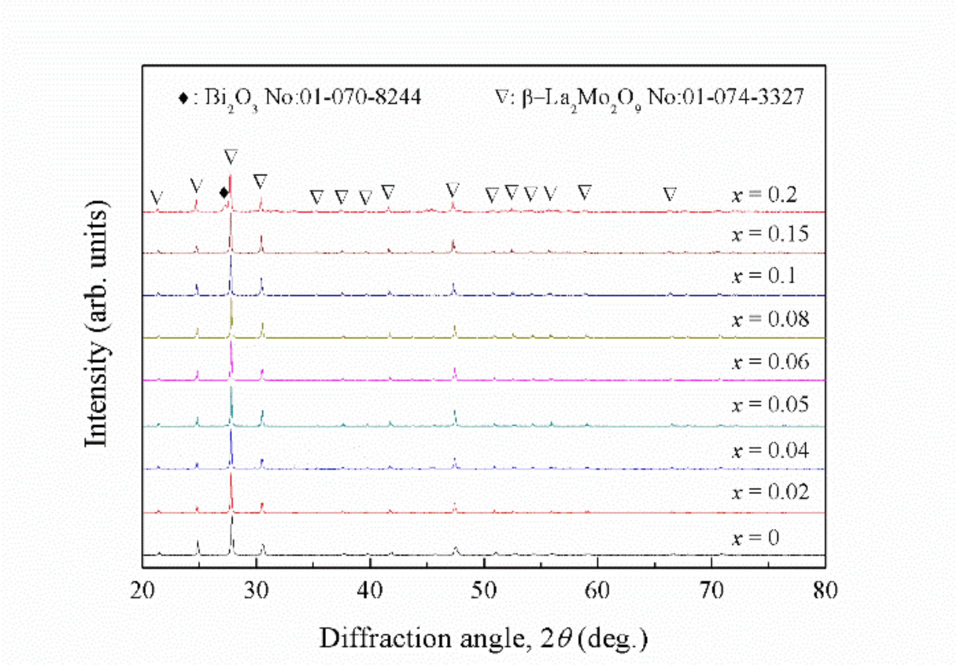

Figure 4.1 X-ray diffraction patterns of $(La_{1-x}Bi_x)_2Mo_2O_9$ powders ($0 \leq x \leq 0.2$).

The room-temperature lattice constants are shown in Fig. 4.2 as a function of the Bi content, together with the reported data [4,5]. Figure 4.2 shows that the lattice constant increases linearly to $x = 0.15$ with respect to the Bi content, suggesting behavior according to Vegard's law. This result is consistent with the value of the solubility limit estimated from the XRD patterns. Although the ionic radii of Bi^{3+} (1.24 Å) and La^{3+} (1.22 Å) with a coordination number of 9 are nearly equal [6], the lattice parameter increases with Bi substitution. Substitution of Bi at the La site creates an intrinsic vacancy from the interactions between the lone pair and oxygen atoms, which causes lattice expansion [5]. The variation of the lattice parameter with the Bi content is similar to that documented by Paul [4] and Goutenoire [5]. Consequently, the $(La_{1-x}Bi_x)_2Mo_2O_9$ solid solution is successfully synthesized below $x = 0.15$, which agrees with the published values [7].

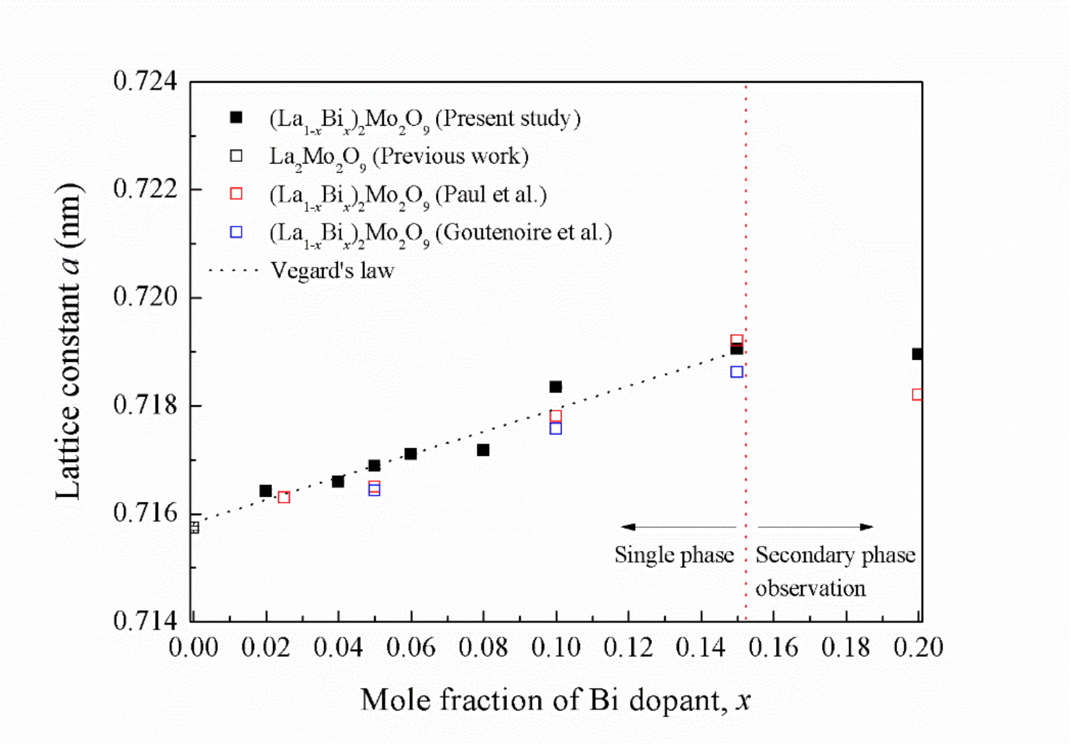

Figure 4.2 Lattice constant of $(La_{1-x}Bi_x)_2Mo_2O_9$ as a function of Bi dopant.

Figure 4.3 shows the LTECs of $(La_{1-x}Bi_x)_2Mo_2O_9$ ($0 \leq x \leq 0.15$) upon heating. The LTEC of non-doped $La_2Mo_2O_9$ rapidly changes by 10% (from 16.6×10^{-6} to 18.3×10^{-6} K^{-1}) between 798 and 823 K. This sudden change is caused by the $\alpha \rightarrow \beta$ phase transition. No sudden change is observed for the Bi-doped $La_2Mo_2O_9$ samples, suggesting that the β-phase is stabilized by

Bi substitution. This result means that Bi substitution suppresses the α-β phase transition. This behavior is consistent with adequate substitution of the La and Mo sites, which can suppress the α-β phase transition and stabilize the β-phase [7]. Figure 4.4 displays the average LTECs of $(La_{1-x}Bi_x)_2Mo_2O_9$ ($0 \le x \le 0.15$) as a function of the amount of Bi dopant. From Fig. 4.4, the LTEC of α-$La_2Mo_2O_9$ is 15.2 × 10^{-6} K^{-1} in the low temperature region (323-773 K), and it increases to 19.5 × 10^{-6} K^{-1} in the high temperature region (873-1073 K). These values are within the expected range for the low-temperature α-phase and high temperature β-phase [8]. The overall LTECs of $La_2Mo_2O_9$ with the Bi dopant are higher than the LTEC of non-doped $La_2Mo_2O_9$. Based on Eq. (1.15), increased LTEC suggests an increased Grüneisen parameter, which represents enhanced anharmonicity. Thus, the increased LTEC implies increased anharmonicity from Bi substitution. The obtained LTEC was used to calculate the Grüneisen parameter and lattice thermal conductivities (κ_L).

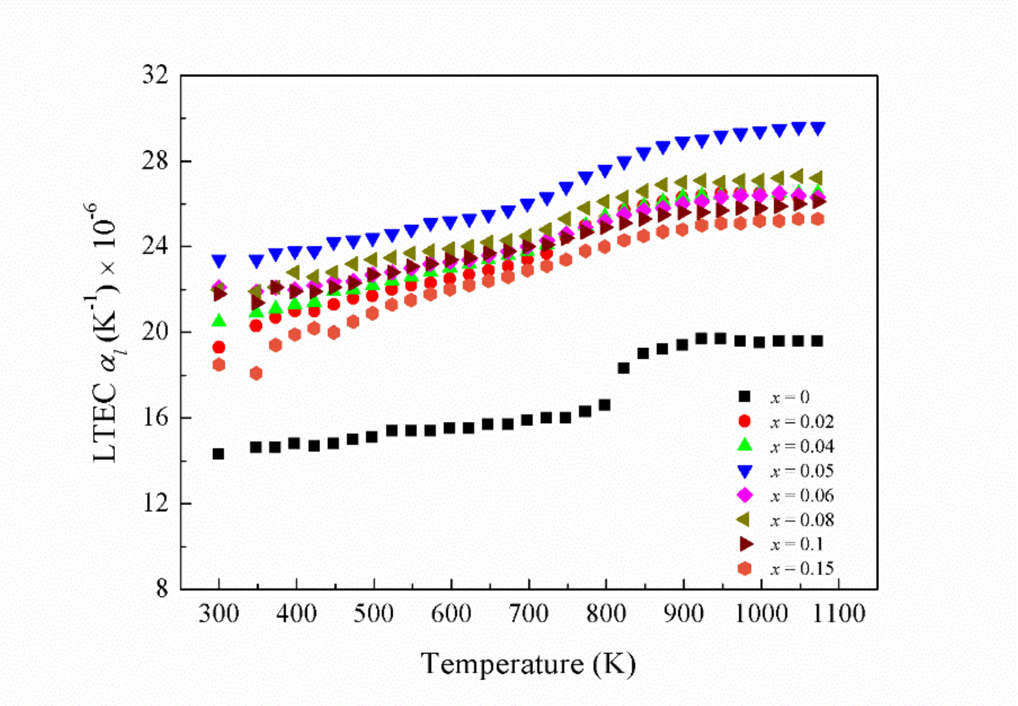

Figure 4.3 Linear thermal expansion coefficient of $(La_{1-x}Bi_x)_2Mo_2O_9$ ($0 \le x \le 0.15$) on heating.

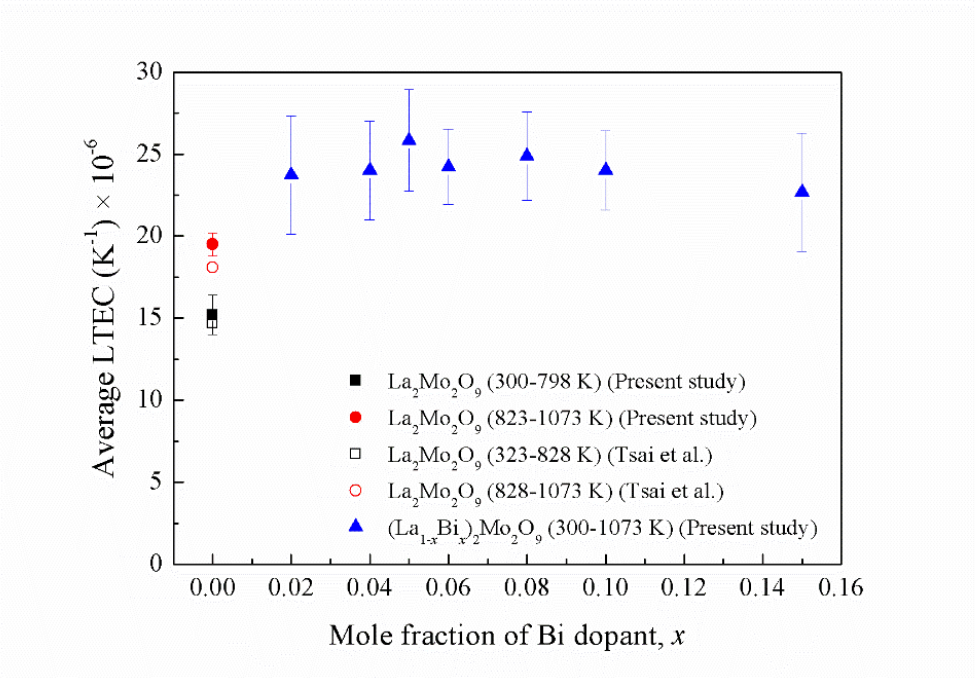

Figure 4.4 Average thermal expansion coefficient of $(La_{1-x}Bi_x)_2Mo_2O_9$ ($0 \leq x \leq 0.15$) as a function of Bi dopant.

Figure 4.5 shows the temperature dependence of C_p from room temperature to 1073 K for all samples. Our previous data ($x = 0$) included a sharp endothermic peak around 850 K, corresponding to the α-β phase transition, which agreed well with the data reported by Lacorre et al. [7]. For the $(La_{1-x}Bi_x)_2Mo_2O_9$ samples, a small endothermic peak is observed at approximately 730 K at $x = 0.02$. In contrast, no endothermal peak is observed in the DSC curves of the samples with $0.04 \leq x \leq 0.15$. This result indicates that the α-β phase transition is fully suppressed when the Bi content (x) is larger than 0.04, which agrees with that evaluated from the thermal expansion measurements and the literature [9], where the threshold composition is around $x = 0.02$. These results indicate that phase transition was prevented by Bi^{3+} and Bi^{3+} dopant is suitable for β-cubic phase at room temperature. This is demonstrated by lattice degrees of freedom at La site, indicated as the values of the average cation-oxygen distance: <La-O>. In β-phase, the oxygen coordination around La is schematically presented: La is surrounded by 15 oxygens and the value of average <La-O> interatomic distance is 2.66 Å (see Fig. 4.6 (a) and (c)) [10]. On the other hands, La has a coordination shell including between 6 and 12 oxygen atoms, with 30 out of the 48 independent La being 9-coordinate (see Fig. 4.6 (b)) [11] and the value of average <La-O>

interatomic distance is smaller than 2.61 Å in α-phase. This is because that unit cell volume of α-phase (366.5 Å^3) is ~2% smaller than that of β-phase (373.5 Å^3). Thus, the La-O polyhedral volume of α-phase is ~2% smaller than that of β-phase because La-O polyhedral volume is dependent upon the unit cell volume. For this reason, the value of average <La-O> interatomic distance in α-phase would be 1.21 Å (see Fig. 4.6 (d)). This value is almost similar with ionic size of La^{3+} (1.22 Å) with a coordination number of 9, which means La^{3+} is suitable for α-phase stabilized foam at room temperature. On the contrary, the value of average <La-O> interatomic distance (1.26 Å) in β-phase is larger than ionic size of La^{3+} (1.22 Å). Hence, a bigger ion ought to occupy more space than a La^{3+} (1.22 Å) and consequently replacement of Bi^{3+} (1.24 Å) with a coordination number of 9 for smaller one results in stable lattice. However, ionic radii of Bi^{3+} is still somewhat smaller than required ionic La-site for stabilization (1.26 Å). This result suggests that phase transition would be completely suppressed by certain amount of Bi^{3+} for La^{3+} site.

The C_p values of Bi-doped $La_2Mo_2O_9$ are almost identical from 323 to 1073 K. C_p was calculated using θ_D, α_l, and B (see Table 4.2 and Fig. 4.4) for comparison with the experimental value. The calculated C_p values of $(La_{1-x}Bi_x)_2Mo_2O_9$ agree with the experimental data, suggesting that the measured data are reasonable.

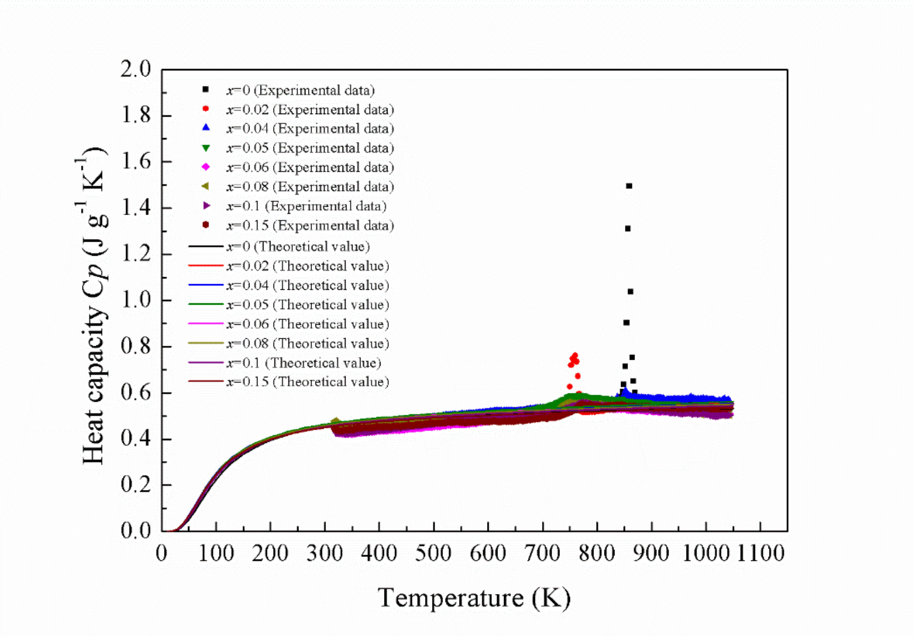

Figure 4.5 Specific heat capacity at constant pressure of $(La_{1-x}Bi_x)_2Mo_2O_9$ ($0 \leq x \leq 0.15$) as a function of temperature.

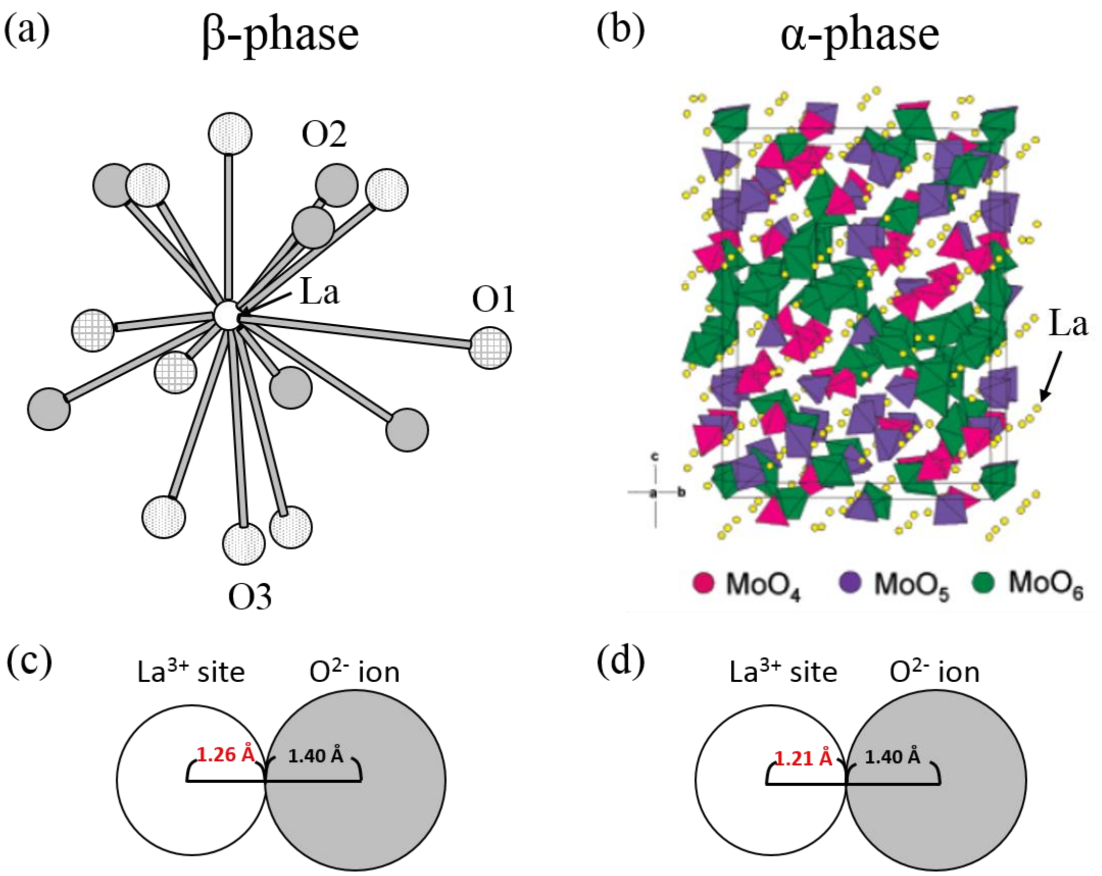

Figure 4.6 (a) Oxygen coordination around La in β-phase [10], (b) Polyhedral representation of α-phase: tetrahedral groups (pink), trigonal bipyramidal (purple), octahedral (green) [11], (c) estimated average La-O interatomic distance for α-phase, and (d) average La-O interatomic distance β-phase.

Figure 4.7 shows the thermal conductivity as a function of temperature for fully dense $(La_{1-x}Bi_x)_2Mo_2O_9$ ($0 \leq x \leq 0.15$). Because the relative densities of the studied samples are different (see Table 4.1), the thermal conductivity was corrected to 100% of the theoretical density using the Maxwell relation. Figure 4.7 shows that the thermal conductivities for all samples are temperature independent over the entire temperature range. The temperature independent behavior of the thermal conductivity is a characteristic of amorphous materials.

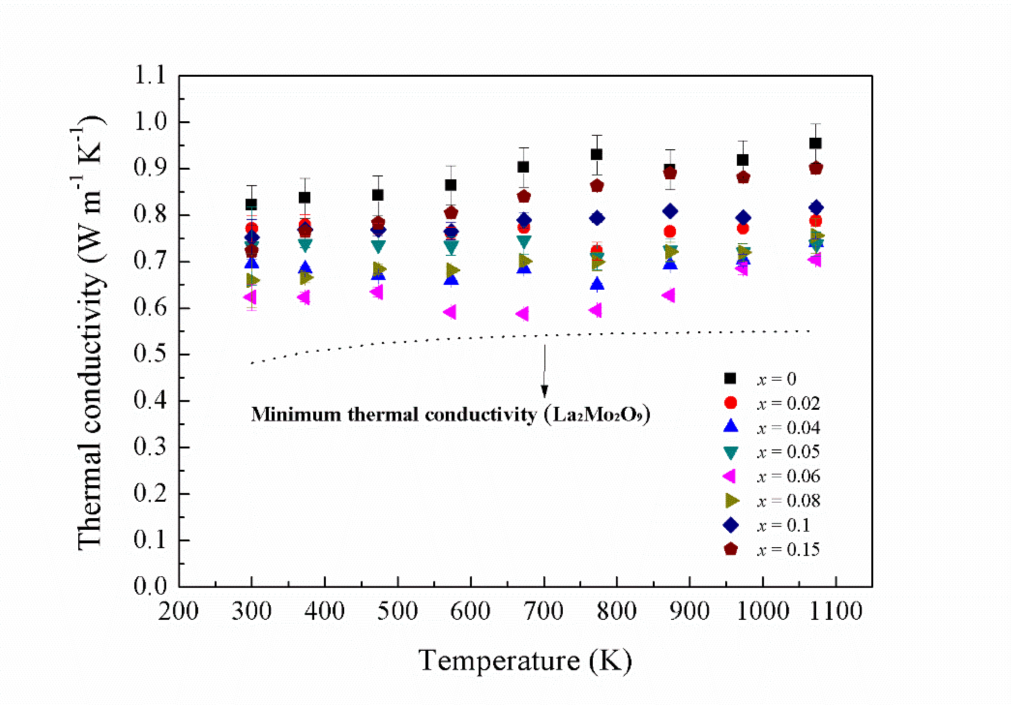

Figure 4.7 Thermal conductivity of (La$_{1-x}$Bi$_x$)$_2$Mo$_2$O$_9$ ($0 \le x \le 0.15$) as a function of temperature.

To understand the temperature independent behavior of the thermal conductivity of La$_2$Mo$_2$O$_9$, we calculated the minimum thermal conductivity, κ_{min}, for La$_2$Mo$_2$O$_9$ based on a model proposed by Cahill et al. [1]. This model properly describes the thermal conductivity of amorphous materials. In this model, the relaxation time, τ, of each phonon is one half of the period of vibration, $\tau = \pi/\omega$,

$$\kappa_{min} = \left(\frac{\pi}{6}\right)^{1/3} k_B n^{2/3} \sum_i v_i \left(\frac{T}{\theta_i}\right)^2 \int_0^{\theta_i/T} \frac{x^3 e^x}{(e^x-1)^2} dx \tag{4.2}$$

where θ_i and v_i are the Debye cut-off frequency and phonon velocity, respectively ($\theta_i = v_i(\hbar k_B)(6\pi^2 n)^{1/3}$), and n is the number of atoms in a primitive cell. The subscript *i* represents the phonon branches: two transverse branches and one longitudinal branch. The value of κ_{min} for La$_2$Mo$_2$O$_9$ is shown in Fig. 4.7 as a dotted line. The value of κ_{min} is 0.48 W m^{-1} K^{-1} at room temperature and almost independent of temperature. As shown in Fig. 4.7, the magnitude of the thermal conductivity for the (La$_{1-x}$Bi$_x$)$_2$Mo$_2$O$_9$ solid solution is similar to that of κ_{min}. This result suggests that the phonon mean free path is very short and consequently temperature independent, like that for an amorphous material.

The composition dependence of the thermal conductivity is shown in Fig. 4.8. The overall thermal conductivities of (La$_{1-x}$Bi$_x$)$_2$Mo$_2$O$_9$ are lower than the thermal conductivity of non-doped $La_2Mo_2O_9$. The thermal conductivity shows a convex downward shape for $x = 0$-0.1 and minimized at $x = 0.06$. At $x = 0.06$, the thermal conductivity at 300 K declines to 0.62 W m^{-1} K^{-1}. This value is 24% lower than that of non-doped $La_2Mo_2O_9$ (0.82 W m^{-1} K^{-1} at 300 K). Further substitution of bismuth ($x = 0.1$-0.15) produces a downward sloping curve for the thermal conductivity and reduces κ. The convex downward behavior near $x = 0.06$ is contradictory to the alloy scattering model, where κ reduces monotonically with increasing impurity content. This result suggests that a phonon scattering mechanism other than impurity scattering becomes dominant for x near 0.06.

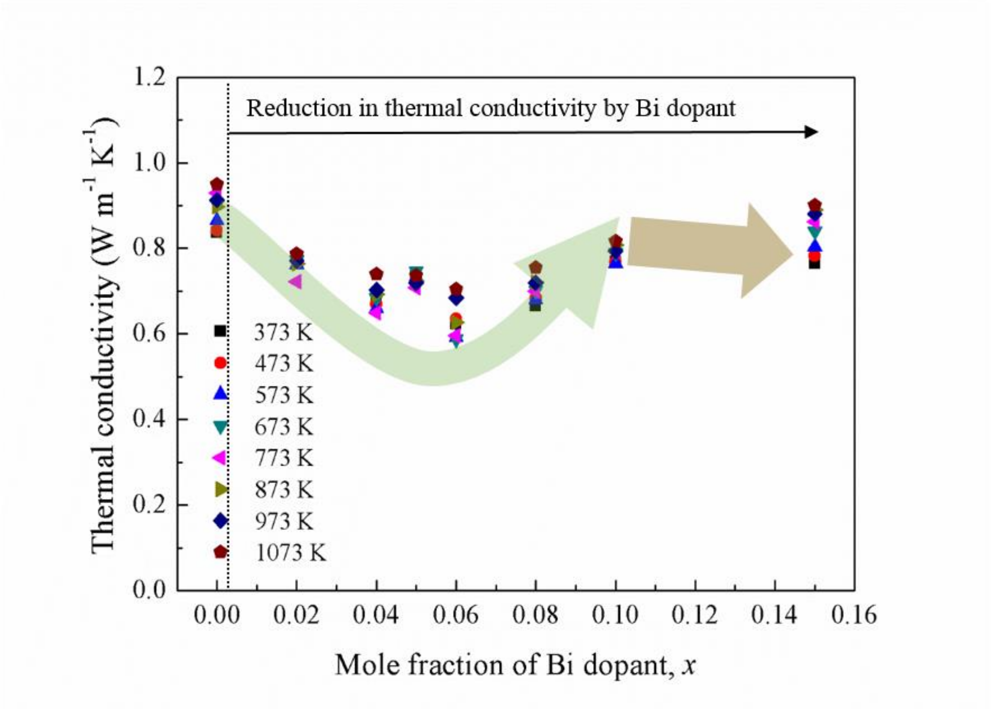

Figure 4.8 Thermal conductivity of $(La_{1-x}Bi_x)_2Mo_2O_9$ ($0 \leq x \leq 0.15$) as a function of Bi dopant.

The composition-dependent average Grüneisen parameter was calculated using Eq. 1.15 from the experimentally obtained values of α_l, C_v, and B. When $x = 0$, the value of γ is 2.6. The large γ is due to intrinsic oxygen vacancies from partially (78%) occupied O2 and O3 sites arise from an electrostatic repulsive force of cations surrounding oxygen vacancies. This is because the creation of vacancies disrupts the alternation of cations and anions in the perfect ionic lattice and therefore leads to anions/cations to each other around cationic/anionic vacancies. For a normal lattice, anharmonic term of the interatomic potential energy expansion favors expansion of lattice as if it generates a repulsive component of the force of lattice. Inversely, the presence of additional repulsive lattice force can contribute to a high lattice anharmonicity. Thus, we believe that electrostatic repulsive force induced by intrinsic oxygen vacancies as the underlying reason for the high Grüneisen parameter. As shown in Fig. 4.9, γ is convex upward and maximized at $x = 0.05$. There is a correlation between the behaviors of κ and γ: convex downward with minima at $x = 0.06$ for κ and convex upward with maxima at $x = 0.05$ for γ. This suggests that the enhanced anharmonicity affects κ near $x = 0.06$. The reason for the convex upward behavior of γ is still being explored. While the introduction of LPEs enhances the anharmonicity, the relationship between the number of LPEs and the anharmonicity might not be proportional.

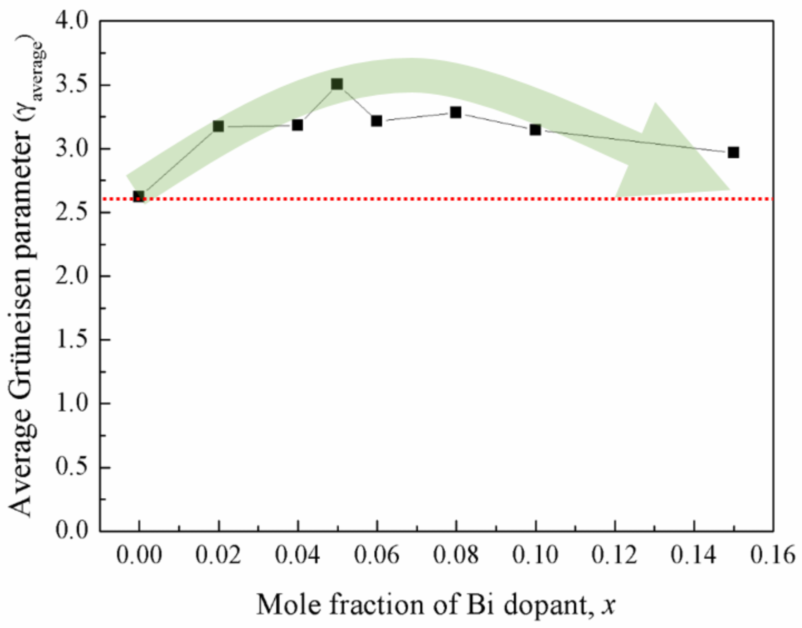

Figure 4.9 Average Grüneisen parameter of $(La_{1-x}Bi_x)_2Mo_2O_9$ ($0 \leq x \leq 0.15$) as a function of Bi.

To clarify the effect of anharmonicity induced by Bi substitution on κ in $(La_{1-x}Bi_x)_2Mo_2O_9$ solid solutions, we calculated the thermal conductivity based on the Klemens-Callaway model. The anharmonicity, γ, contributes phonon-phonon Umklapp scattering (the equation of which is provided later). The total relaxation time can be expressed as ${\tau_{total}}^{-1} = {\tau_P}^{-1} + {\tau_U}^{-1}$, where τ_p and τ_U are the relaxation times of phonon-point defect scattering and Umklapp phonon-phonon scattering, respectively. The relaxation time of point defects scattering is ${\tau_p}^{-1} = A\omega^4$. Parameter A is described by:

$$A = \frac{\Omega_0}{4\pi v_B^3}\Gamma \tag{4.3}$$

where Ω_0 is the atomic volume and Γ is the phonon scattering parameter. The scattering parameter, Γ, is related to the mass fluctuation, Γ_M, and strain field fluctuation, Γ_S, by $\Gamma = \Gamma_M + \Gamma_S$ [12,13].

The strength of the strain field fluctuation effect depends on the size difference in the matrix and the substituted ions [14]. We neglect the effect of the strain field fluctuation scattering because the ionic size difference between Bi^{3+} and La^{3+} is only 1.6%. Then, the scattering parameter can be written as:

$$\Gamma \approx \Gamma_M = \frac{2}{13}\left(\frac{\bar{M}_{La-site}}{\bar{M}}\right)^2 x(1-x)\left[\left(\frac{M_{Bi}-M_{La}}{\bar{M}_{La-site}}\right)^2\right] \tag{4.4}$$

where $\bar{M}$ is the average atomic mass of the compound, $\bar{M}_{La-site}$ is the average atomic mass on the La-sublattice, x is the concentration of Bi, M_{La} is the atomic mass of La, and M_{Bi} is the atomic mass of Bi. The relaxation time of Umklapp scattering is given by

$$\tau_U{}^{-1} = B_U T \omega^2 \exp(-\theta/3T) \tag{4.5}$$

$$B_U \approx \frac{\hbar\gamma^2}{M v_B^2 \theta} \tag{4.6}$$

$$\gamma = \frac{3\alpha_l V_m B}{C_v} \tag{4.7}$$

where M is the average mass of all atoms. The experimentally obtained γ was used in the calculation. We calculated κ in two ways: (1) considering that γ changes, and (2) considering that γ is constant ($\gamma = 2.6$).

Figure 4.10 shows the estimated thermal conductivity of $(La_{1-x}Bi_x)_2Mo_2O_9$ ($0 \leq x \leq 0.15$) together with the measured thermal conductivity. As shown in Fig. 4.10, the estimated thermal conductivity for x = 0, which considers only phonon-phonon Umklapp scattering mechanisms, roughly agrees with the measured thermal conductivity, even though we did not use any fitting parameters. The calculation curves, including the effect of point defect scattering without considering the enhanced anharmonicity induced by Bi substitution, are shown in Fig. 4.10 as dotted lines. The thermal conductivity slightly decreases monotonically with respect to increasing Bi composition. In contrast, the calculated results considering the change in γ capture the tendency of the experimental data: convex downward with minima near x = 0.06. These results clearly indicate that the enhanced anharmonicity reduces the thermal conductivity near x = 0.06.

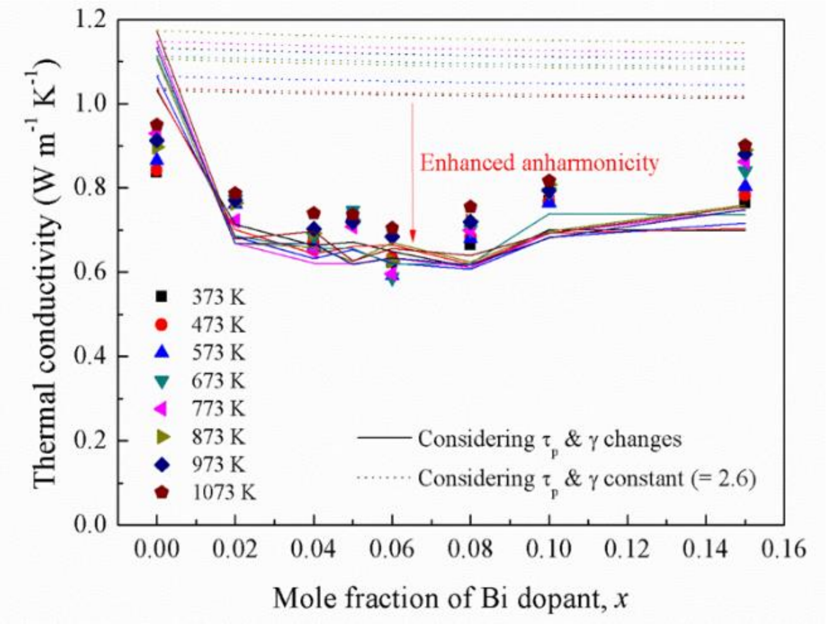

Figure 4.10 Calculated and measured thermal conductivities as a function of the fully dense $(La_{1-x}Bi_x)_2Mo_2O_9$ ($0 \leq x \leq 0.15$) compounds with Bi dopants at various temperatures. Solid symbol: experimentally observed value. Dotted line: calculated value including the effect of substitution. Solid line: calculated value including the effect of substitution and lone pair electrons.

4.4 Conclusions

The effects of Bi substitution on the thermal properties of $La_2Mo_2O_9$ were studied. The solubility limit of Bi in $(La_{1-x}Bi_x)_2Mo_2O_9$ was between $x = 0.15$ and 0.2 from the XRD analysis. DSC measurements revealed that the α-β phase transition was suppressed when $x > 0.02$-0.04. The Bi substitution contributes to the increase in the Grüneisen parameter, which indicates that the anharmonicity increased. The Grüneisen parameter shows a maximum near $x = 0.06$. This behavior agrees with the thermal conductivity, which has a minimum near the same composition. At room temperature, the thermal conductivity decreased by 24% for $x = 0.06$ with respect to non-doped $La_2Mo_2O_9$. The effect of the enhanced anharmonicity induced by Bi substitution on the thermal conductivity was evaluated based on the Klemens-Callaway model using the experimentally determined Grüneisen parameter. In this model, the effect of anharmonicity was considered via phonon-phonon Umklapp scattering. The calculated results captured the behavior of the experimentally obtained thermal conductivity, indicating that the enhanced anharmonicity played an important role in reducing the thermal conductivity. Enhancing the anharmonicity by doping with elements containing LPEs is an effective method to reduce the thermal conductivity of materials.

4.5 References

[1] D.G. Cahill, S.K. Watson, R.O. Pohl, *Phys. Rev. B* **46** 6131 (1992).

[2] E.J. Skoug, D.T. Morelli, *Phys. Rev.* **107** 235901 (2011).

[3] B. Du, K. Chen, H. Yan, M.J. Reece, *Scr. Mater*. **111** 49 (2016).

[4] T. Paul, A. Ghosh, *J. Appl. Phys*. **114** 164101 (2013).

[5] F. Goutenoire, O. Isnard, E. Suard, O. Bohnke, Y. Laligant, R. Retoux, Ph. Lacorre, *J. Mater. Chem.* **11** 119 (2001).

[6] R.D. Shannon, *Acta Crystallogr., Sect. A* **32** 751 (1976).

[7] P. Lacorre, F. Goutenoire, O. Bohnke, R. Retoux, Y. Laligant, *Nature* **404** 856 (2000).

[8] D.S. Tsai, M.J. Hsieh, J.C. Tseng, H.Y. Lee, *J. Eur. Ceram. Soc*. **25** 481 (2005).

[9] V. Voronkova, E. Kharitonova, A. Krasilnikova, *Phys. Status Solidi A* **206** 2564 (2009).

[10] C. Tealdi, L. Malavasi, C. Ritter, G. Flor, G. Costa, *J. Solid State Chem*. **181** 603 (2008).

[11] I.R. Evans, J.A.K. Howard, J.S.O. Evans, *Chem. Mater.* **17** 4074 (2005).

[12] B. Abeles, *Phys. Rev.* **131** 1906 (1963).

[13] G.A. Slack, *Phys. Rev.* **105** 829 (1957).

[14] J. Yang, G.P. Meisner, L. Chen, *Appl. Phys. Lett*. **85** 1140 (2004).

CHAPTER V

Effect of Oxygen Vacancy Arrangement on Thermophysical Properties TiO_{2-x}

In this chapter, the author covers an effect of randomly distributed oxygen vacancies (point defects) and ordered oxygen vacancies (planar defects) on the thermal conductivity in same material (titanium oxide, TiO_{2-x}). The effect of planar defect on the reduction thermal conductivity was expressed using new model of relaxation time for phonon-planar defect scattering (τ_{planar}). Each phonon scattering was clarified by combined theoretical and experimental analysis. The properties such as elastic moduli, Debye temperature, electrical conductivity, and thermal conductivity of the compounds were studied to build empirical thermal conductivity model. The author incorporated the phonon scattering effect of point defects and planar defects into the relaxation time. The obtained results was used for comparison of the various phonon scattering effects on thermal conductivity.

5.1 Introduction

In this chapter, the author covers an effect of alloying, randomly distributed oxygen vacancies, and enhancing anharmonicity on the thermal conductivity in polycrystalline bulk lanthanum molybdate. The properties such as thermal expansion coefficient, heat capacity, elastic moduli, Debye temperature, and thermal conductivity of the compounds were studied to build empirical thermal conductivity model. The author incorporated the effect of alloying, oxygen vacancies, and enhancement of anharmonicity into the relaxation time. The obtained results was used for comparison of the various phonon scattering effects on thermal conductivity.

5.1.1 Associations of oxygen vacancies and planar defects

Oxygen vacancy is assumed to be present as single, unassociated oxygen vacancies are randomly distributed in the crystal structure. Generally, when the fraction of oxygen vacancies relative to the number of atoms in the crystal is small at stable temperature, oxygen vacancy is stable and can exist [1].

For larger concentrations of oxygen vacancy expect that oxygen vacancies starts to interact with each other. The interactions may change the coefficients of activity and formation enthalpies of defects, and they could lead to associations between vacancies which attract each other. Minimization of energy can for large concentrations of vacancy give rise to clusters of oxygen vacancies or oxygen vacancies elimination in lines or planes, so as to form a shear structure [2].

Disorder or order of oxygen vacancies is a matter of a balance between the configurational entropy of the oxygen vacancies and the exothermic enthalpy gained in association of certain oxygen vacancies to form various kinds of larger vacancies agglomerations. Materials with relatively small vacancy concentrations are controlled entropy and consist of randomly distributed oxygen vacancies formation [1]. With increasing vacancy concentration, the enthalpy controls and leads sequentially to formation of larger defect; randomly associated defects or extended defects, and shear planes [1].

5.1.2 Defect Equilibrium

The correlate the equilibrium concentrations of the different defects with temperature, partial pressures of the components in the compound, and other parameters which affect the defect structure. The defect equilibrium will generally be described by the law of mass action. The change in the Gibbs free energy G of a chemical reaction in a closed system is expressed by

$$\Delta G = \Delta H - T\Delta S \tag{5.1}$$

where ΔH is the change of enthalpy for reaction and ΔS is the change of entropy for reaction. In this expression, the reaction will proceed spontaneously as long as $\Delta G < 0$, until G has reached its minimum.

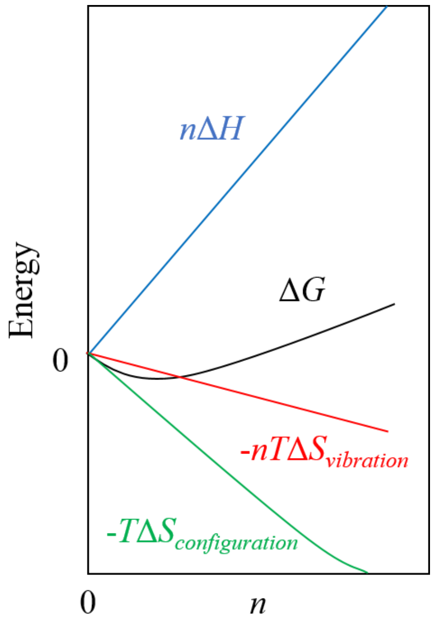

Figure 5.1 Change in Gibbs energy, enthalpy, and vibrational and configurational entropy with the concentration of vacancies in solid.

When vacancies n_v is formed, the enthalpy can be changed as $n_v\Delta H$. This represents the energy cost connected with creating a new empty site. The enthalpy should be one that is valid for ideal dilute solutions of vacancies in the lattice because we are treating with small concentration vacancies. The change in entropy can be divided into two parts: 1) a change in vibrational entropy $\Delta S_{vibration}$ representing the entropy created by vibrations associated with each new vacancy, and 2) a change in configurational entropy $\Delta S_{configuration}$ arising from the distribution from n vacancies among total number of sites. The change in vibrational entropy is connected with the vibrations in the neighbourhood of each vacancy, and the change in total vibrational entropy varies with the concentration of vacancies.

The changes in enthalpy and vibrational entropy are approximately proportional to the concentration of vacancies formed, while the configurational entropy is a more complex function. In Fig. 5.1, the Gibbs free energy change associated with the formation of vacancies can be given by

$$\Delta G = n_v(\Delta H - T\Delta S_{vibration}) - T\Delta S_{configuration} \tag{5.2}$$

In this expression, we can estimate that formation of point defect (randomly distributed oxygen vacancies) or planar defect (ordered oxygen vacancies) will be dominated by concentration of vacancies and given temperature.

5.1.3 Crystal Structure of Rutile Titanium Dioxide

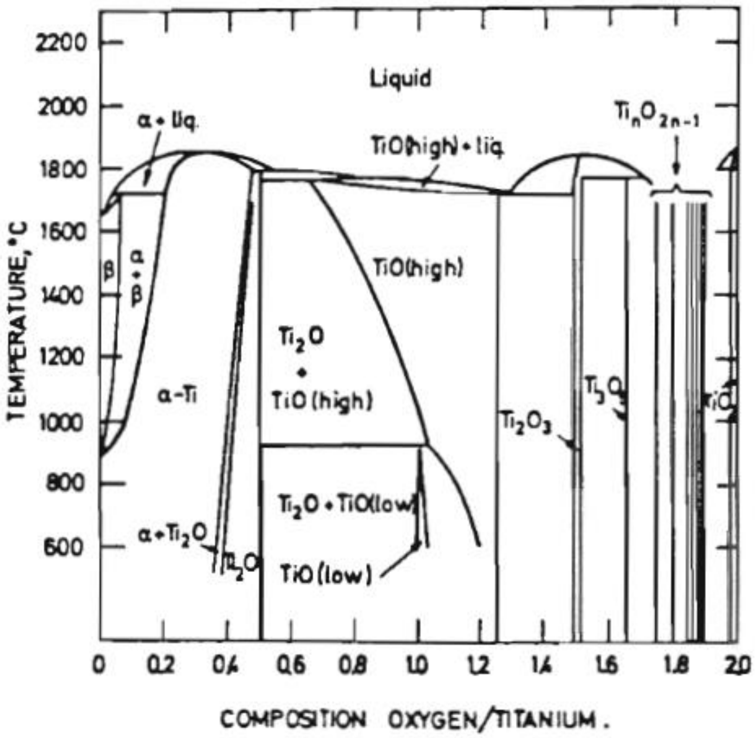

Figure 5.2 Phase diagram of Ti-O [3].

Figure 5.2 shows the phase diagram of Ti-O binary system. Both a wide range of a homologous series of oxides with the composition Ti_nO_{2n-1} and a narrow range of slight difference in stoichiometry between stoichiometric rutile and Ti_2O_3. The different from stoichiometry is accommodated by point defects or associations point defects and planar defects exist.

5.1.3.1 Structure of Stoichiometric Rutile

The TiO_2 has rutile, anatase, brookite, or polymorphic phases. One of phase, rutile is the most stable phase at one atmosphere. Figure 5.3 shows the crystal structure of rutile TiO_2. As shown in Fig. 5.3, the rutile structure consists of rectilinear ribbons of edge-shared TiO_6 octahedra joined by corner-shearing to similar ribbons. Thus the orientations of adjacent ribbons differ by 90°, in which unit cell is tetragonal.

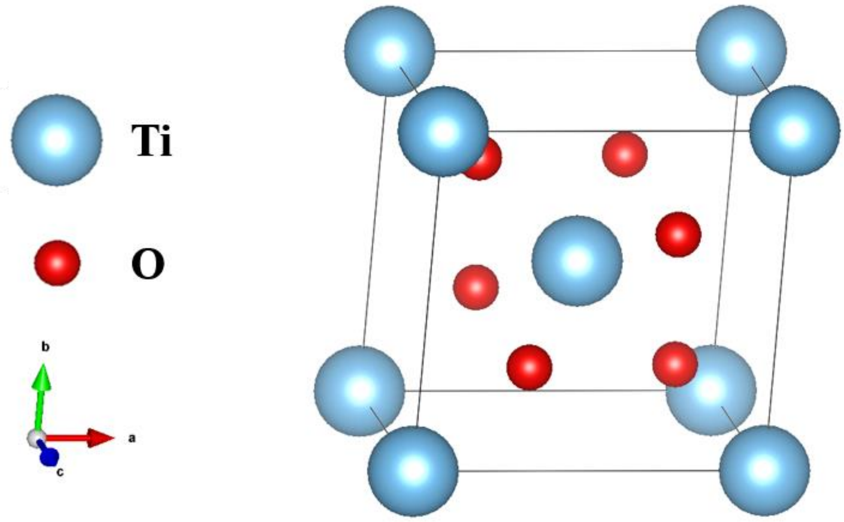

Figure 5.3 Schematic illustration of crystal structures of rutile TiO_2.

5.1.3.2 Structure of Nonstoichiometric Rutile

There are three characterized regions such as point defects, random crystallographic shear planes with point defects, and the homologous Ti_nO_{2n-1} (crystallographic shear planes) as known as Magnéli phase. So TiO_{2-x} has extended defects. The extended defects are planar defects and may be considered to be formed by ordering and elimination of oxygen vacancies along specific crystallographic plane.

According to Bursill and Hyde [4], the planar planes were observed in very small departures from stoichiometry, in which the nominal composition was $TiO_{1.9986}$ at 1270 K. The range of extent of the point defect is not clear. As the concentration of point defects increases, the interaction between them creates extended aggregation of defect. Consequentially, titanium oxides develop crystallographic shear planes in the reduction process. Figure 5.4 shows the schematic illustration of crystal structures of rutile and Magnéli phase. As shown in Fig. 5.4, rutile phase has ordered oxygen and titanium atoms arrangement along the [001] direction. While Magnéli phase has ordered oxygen atoms arrangement along the [001] direction and titanium atomic mismatch on (121) plane, which is defined as planar defect as known as a shear plane [5]. This phenomenon is happened by oxygen vacancies. Since when the oxygen atom jumps from its original position into the formed oxygen vacancy, the arrangement of titanium atoms is disturbed.

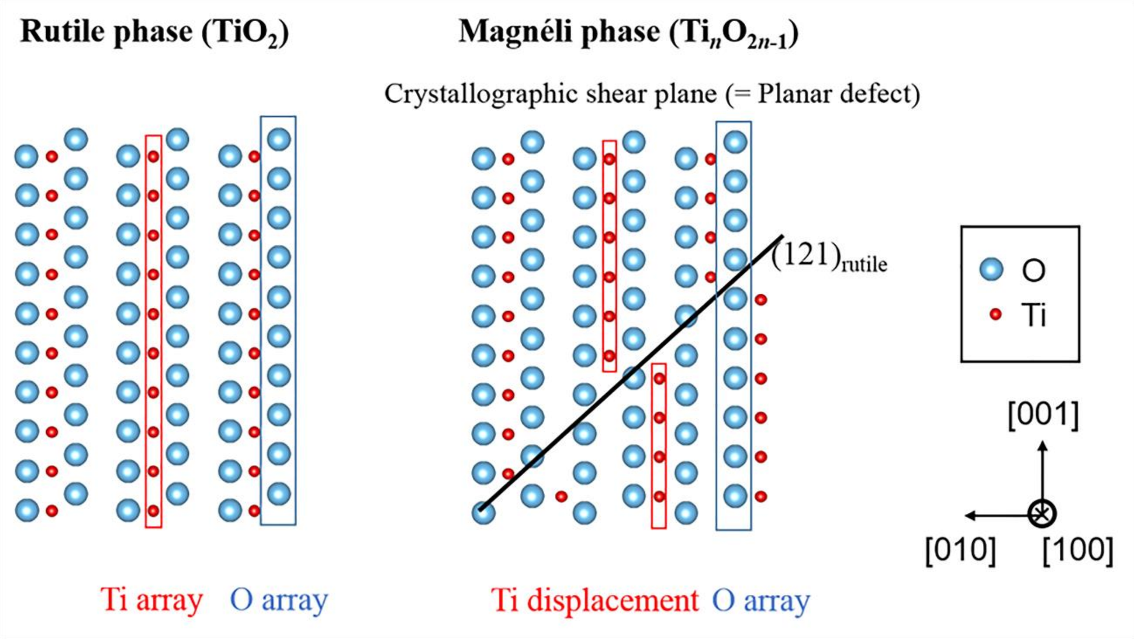

Figure 5.4 Schematic illustration of crystal structures of rutile TiO_2 and Magneli phase Ti_nO_{2n-1}.

5.2 Experimental Procedures

5.2.1. Fabrication of Unquenched TiO_{2-x}

A sample preparation procedure are shown in Fig. 5.5. TiO_2 samples were prepared from TiO_2 powder (Furuuchi Chemical Corp., 99.99%) using spark plasma sintering (SPS–515S, Sumitomo Coal Mining, Japan) for 5min under Ar atmosphere at 1223^{o}K and 80MPa pressure.

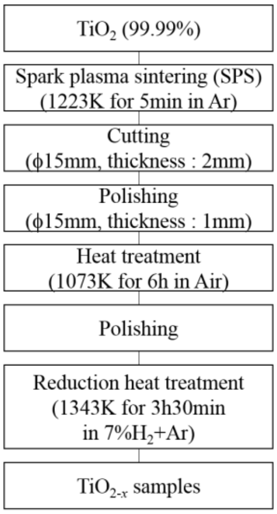

Figure 5.5 Flow chart for preparation of TiO_{2-x}.

During the sintering process, while the temperature was maintained at 1223°K for 1min to eliminate the localized residual stress, the pressure was released as shown in Fig. 5.6.

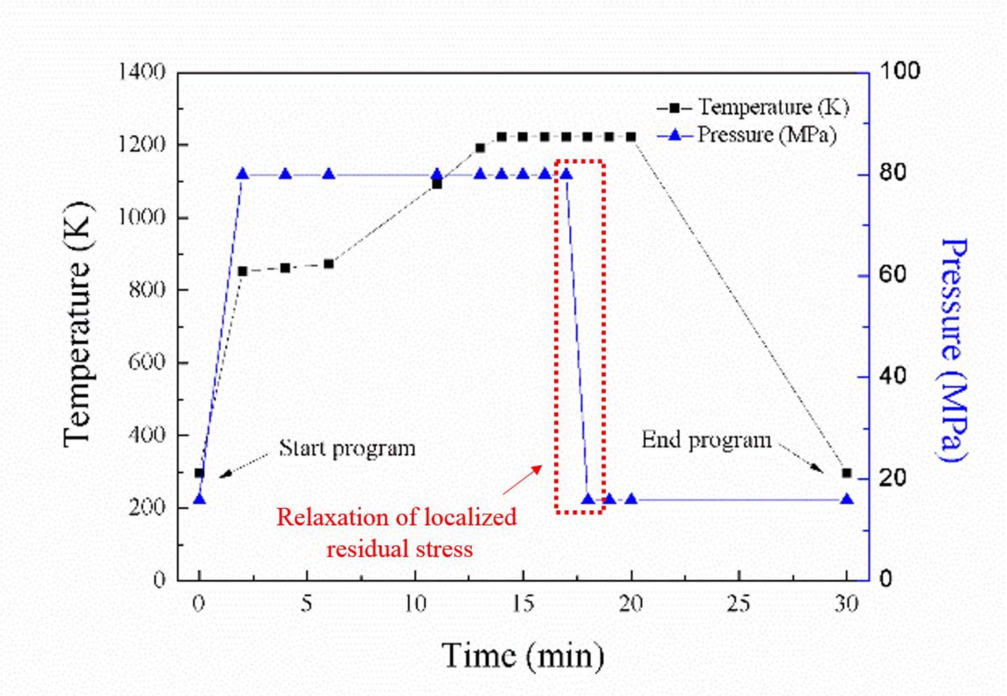

Figure 5.6 Condition of heat treatment by spark plasma sintering for TiO_2 sample.

Before reduction heat treatment was performed, sample was fired to remove residual carbon on the surface. The dense TiO_2 pellets at different temperatures (e.g., 1243, 1273, 1343, and 1423°K) (see Fig. 5.7) followed by the fabrication of non-stoichiometric TiO_{2-x} samples assuming that the deoxidizing of TiO_2 and re-oxidizing of TiO_{2-x} in different heat treatment condition is occurred below equations.

$$TiO_2 + H_{2(g)} \rightarrow TiO_{2-x} + H_2O_{(g)} \uparrow \ \text{(deoxidizing process)} \tag{5.3}$$

$$TiO_{2-x} + \frac{x}{2} O_{2(g)} \rightarrow TiO_2 \ \text{(re-oxidizing process)} \tag{5.4}$$

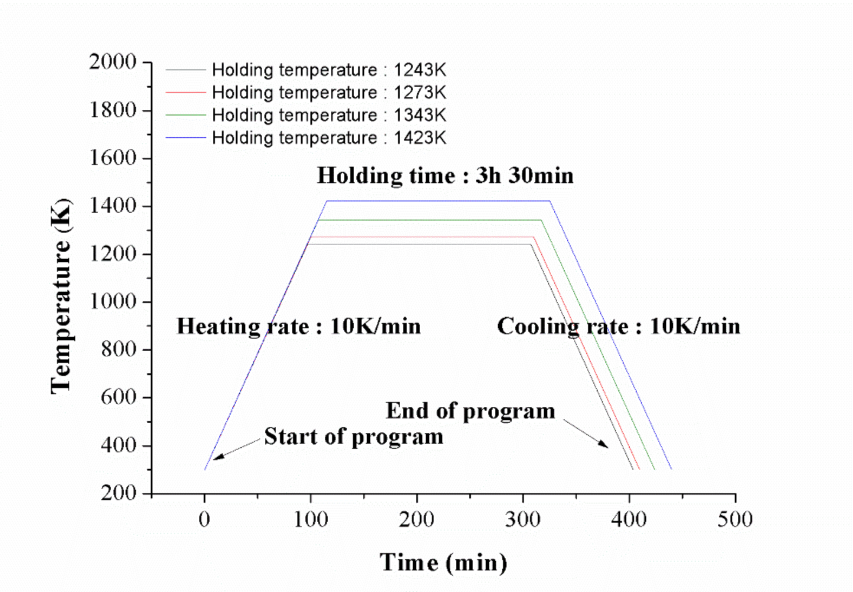

Figure 5.7 Condition of reduction treatment for TiO_{2-x} samples by vacuum furnace.

The sintered TiO_2 samples were heat treated under atmosphere consisting of 7 mol%H_2 in Ar gas flow for 3.5h at various temperatures (e.g., 1243, 1273, 1343, and 1423°K) and then naturally cooled down to room temperature to prepare the unquenched TiO_{2-x} samples with different O/Ti ratios.

5.2.2. Fabrication of Quenched TiO_{2-x}

As the quenched TiO_{2-x} samples, the sintered TiO_2 samples were handled in the same manner. To avoid oxidizing TiO_{2-x} to the entire TiO_2, TiO_{2-x} sample was sealed by silica tube to keep a vacuum state (see Fig. 5.8), and annealed at 1423°K for 24h. Then, they were rapidly cooled by water quenching.

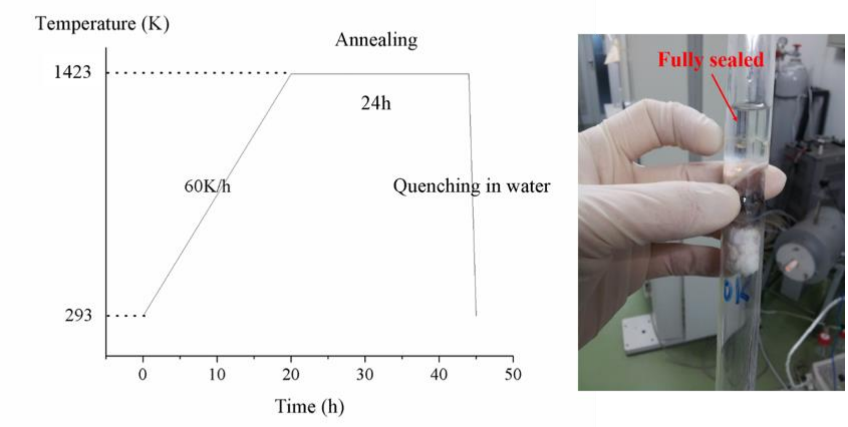

Figure 5.8 Condition of quenching process (left) and illustration of fully sealed sample (right).

5.2.3. Characterization

The stoichiometry of the both unquenched and quenched TiO_{2-x} samples was analyzed by thermogravimetric analysis. By using thermogravimetric differential thermal analyzer (TG–DTA2000SA, NETZSCH), mass difference ΔW was measured when the sample were oxidized to stoichiometric TiO_2. The unquenched TiO_{2-x} powder specimens with weights ranging 12.7 to 30.9 mg were heated at 1423K for 5h at a heating rate of 10 K/min in static air to stoichiometric TiO_2. The O/Ti stoichiometric ratio (2-x) was determined as:

$$\frac{O}{Ti} = 2 - \frac{\Delta W}{M_O}\frac{(2M_O + M_{Ti})}{(W + \Delta W)} \tag{5.5}$$

where M_{Ti} is the titanium molar weight, M_O is the oxygen molar weight, and W is the initial sample weight. Measurements were carried out for unquenched and quenched samples. The observed absolute variations were within 0.03 and 0.02, respectively.

The phase composition and crystal structures of the TiO_{2-x} samples were evaluated as functions of their O/Ti ratios via a powder X-ray diffraction technique using Cu-Kα radiation and a scintillation detector. The data were collected in the 2θ range of 20-60^o at a scan rate of 1^o min^{-1} and step size of 0.01^o. Angular calibration was carried out via the least-squares method of the PDXL software.

The densities of bulk TiO_{2-x} samples were obtained by weights and geometric volumes. The average grain size of samples was obtained by field emission scanning electron microscopy (FE–SEM; JEOL JSM–6500F) and electron backscattering diffraction (EBSD) techniques.

At room temperature, longitudinal and shear sound velocities were measured via an ultrasonic pulse-echo method with a digital storage oscilloscope (TDS2002C, Tektronix). The systematic errors of measuring the longitudinal sound velocity and shear sound velocity were evaluated by examining a standard iron sample and comparing the obtained parameters with the literature [6]. Measurements were carried out three times at different position of samples.

In order to obtain the charge carrier density and mobility, Hall effect was measured by Toyo ResiTest 8340 system at an applied magnetic field of 0.5 T in a van der Pauw geometry. The Hall mobility (μ_H) and carrier concentration (n_H) of TiO_{2-x} were calculated from R_H assuming a single band model and a Hall factor of 1;i.e., $n_H = 1/(R_H e)$ and $\mu_H = R_H/\rho$, where e is the charge of an electron (1.602×10^{-19}C).

Thermal diffusivities were obtained via laser flash method using an LFA457 instrument. Measurements were performed three times over the temperature range from room temperature to 1073K. The thermal diffusivity of a standard graphite sample was measured in the temperature range from room temperature to 1073K to examine systematic error. In order to reduce experimental error, prior to measurement of thermal diffusivity, both faces of sample was coated by graphite using graphite spray because the carbon coating can help improve the laser absorption at the lower surface and increase the intensity of the emissions of the upper surface. The calculated deviations between the NMIJ RM 1201-a and measured values were within 3%.

The thermal conductivity (κ) was calculated from the thermal diffusivity (d), heat capacity (C_p), and sample density (ρ) based on the relationship of $\kappa = dC_p\rho$. The C_p is reported values of specific heat for rutile TiO_2, which is measured by the method of mixtures over the temperature from 298 to 1800K.

5.3 Results and Discussion

Figure 5.9 shows the powder XRD patterns of the unquenched TiO_{2-x} ($2\text{-}x$=2.000, 1.992, 1.985, 1972, and 1.934) specimens. Almost all the peaks are attributed to the Magnéli phase (JCPDS #00-050-0791) not rutile phase (JCPDS #00-021-1276). As O/Ti ratio increases, the measured XRD patterns differed from the spectrum recorded for rutile TiO_2 more significantly and more exactly matched that for Magnéli Ti_9O_{17}. This results suggest that planar defects can be introduced by oxygen vacancies. As shown in Fig. 5.9, while the XRD peaks recorded for the unquenched TiO_{2-x} ($_{2-x}$ =1.992, 1.985, and 1.972) samples originated from both the rutile TiO_2 and Magnéli Ti_9O_{17} phases, the Magnéli Ti_9O_{17} phase was only detected for the unquenched $TiO_{1.934}$ having planar defects. On the contrary, the Magnéli Ti_9O_{17} peaks became smaller or disappeared altogether after annealing and quenching the unquenched TiO_{2-x} samples. The presence of Magnéli Ti_9O_{17} peaks means ordered oxygen vacancies (=planar defects) and the disappeared peaks represents randomly distributed oxygen vacancies (=point defects) as shown in Fig. 5.10. This is because that the oxygen vacancies could be randomly redistributed for annealing process. On the other words, in view point of thermodynamics, since the entropy of point defects is higher than that of planar defects, the randomly distributed oxygen vacancies are stable at high temperature. In the quenched TiO_{2-x} samples, there is no Magnéli Ti_9O_{17} peaks at 2-x = 1.992 and 1.985, which means there is entirely rutile phase. After decreasing the O/Ti ratio, both the rutile TiO_2 phase and Magnéli Ti_9O_{17} phase were present at 2-x = 1.972. Meanwhile, the composition of the quenched $TiO_{1.934}$ was almost identical to that of the unquenched $TiO_{1.934}$ contaning Magnéli Ti_9O_{17} phase. The differences XRD patterns between the unquenched and quenched TiO_{2-x} indicate that the composition of TiO_{2-x} containing low concentration of oxygen vacancies can be controlled by the O/Ti ratio in quenching conditions.

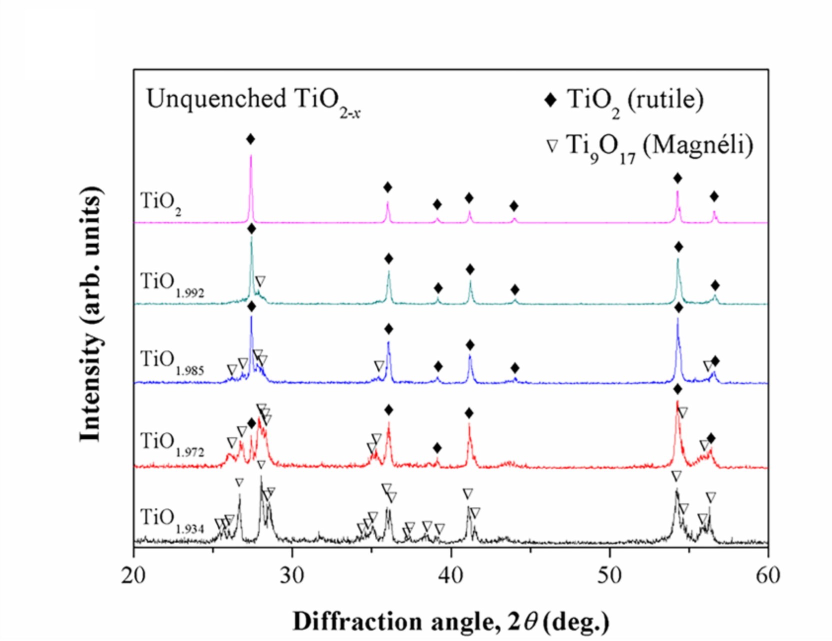

Figure 5.9 XRD patterns of unquenched TiO_2 and TiO_{2-x} (2-x = 1.992, 1.985, 1.972, and 1.934).

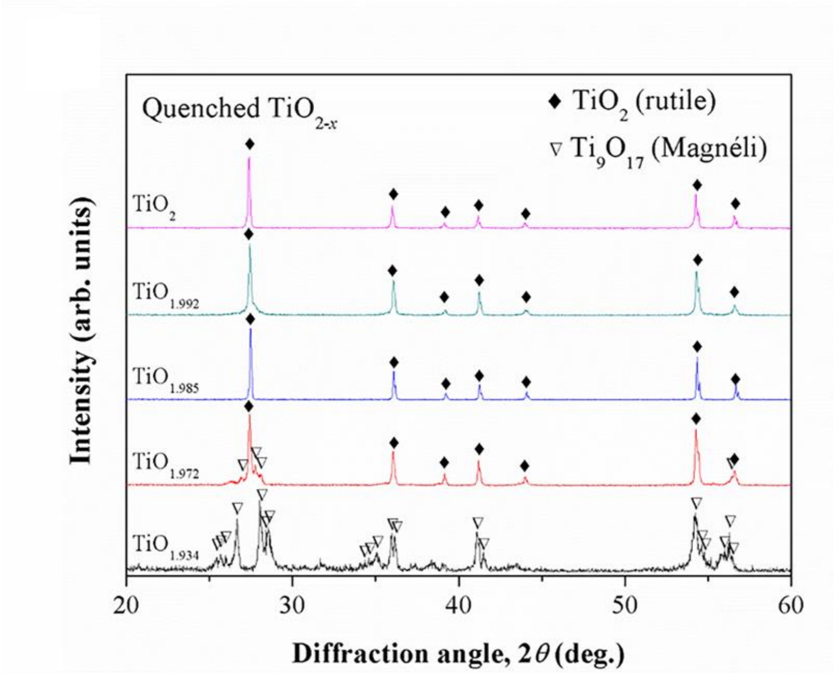

Figure 5.10 XRD patterns of quenched TiO_2 and TiO_{2-x} ($2-x$ = 1.992, 1.985, 1.972, and 1.934).

The phase and main phase introduced by heat and cooling conditions are summarized in Table 5.1.

Table 5.1 Heat treatment and cooling conditions and defect types obtained for the TiO_{2-x} specimens.

Reduction temperature (K)	Annealing temperature (K)	Cooling condition	Main phase	Phases	Defect types
–	–	Unquenched	Rutile	Rutile	Defect-free
–	1423	Quenched	Rutile	Rutile	Defect-free
1243	–	Unquenched	Rutile	Rutile & Magnéli	Point & Planar
1243	1423	Quenched	Rutile	Rutile	Point
1273	–	Unquenched	Rutile	Rutile & Magnéli	Point & Planar
1273	1423	Quenched	Rutile	Rutile	Point
1343	–	Unquenched	Magnéli	Rutile & Magnéli	Point & Planar
1343	1423	Quenched	Rutile	Rutile & Magnéli	Point & Planar
1423	–	Unquenched	Magnéli	Magnéli	Planar
1423	1423	Quenched	Magnéli	Magnéli	Planar

The lattice parameters and sample densities are obtained as following procedures. The theoretical density of the main phase was calculated and compared with the actual density to evaluate the relative density of TiO_{2-x} including both the rutile and Magnéli phases. The obtained relative density was not significantly affected by this assumption, because the deviation between the theoretical densities of the rutile TiO_2 phase (4.250g/cm^3) [7] and Magnéli Ti_9O_{17} phase (4.266g/cm^3) [8] is too small. The main phase of TiO_{2-x} was determined from the intensities of XRD peaks recorded for all specimens. The calculated lattice parameters and relative densities are summarized in Table 5.2 and Table 5.3, respectively.

Table 5.2 Lattice parameters of the main phases obtained for the unquenched and quenched TiO_{2-x} specimens.

O/Ti	Cooling condition	a (Å)	b (Å)	c (Å)	α (°)	β (°)	γ (°)
2.000	Unquenched	4.5925(4)	4.5925(4)	2.9603(5)	90	90	90
2.000	Quenched	4.5917(4)	4.5917(4)	2.9597(6)	90	90	90
1.992	Unquenched	4.5945(7)	4.5945(7)	2.9598(8)	90	90	90
1.992	Quenched	4.5912(5)	4.5912(5)	2.9590(8)	90	90	90
1.985	Unquenched	4.5969(10)	4.5969(10)	2.9625(16)	90	90	90
1.985	Quenched	4.5958(7)	4.5958(7)	2.9611(5)	90	90	90
1.972	Unquenched	5.50(3)	7.12(4)	50.1(3)	66.15(12)	57.33(6)	108.41(10)
1.972	Quenched	4.5965(17)	4.5965(17)	2.9601(12)	90	90	90
1.934	Unquenched	5.54(2)	7.10(3)	50.2(2)	66.51(5)	56.57(7)	108.12(9)
1.934	Quenched	5.53(3)	7.11(4)	50.0(3)	66.51(8)	56.78(9)	108.29(11)

Table 5.3 Theoretical densities of the main phases obtained for the unquenched and quenched TiO_{2-x} specimens.

O/Ti	Cooling condition	Theoretical density (g/cm^3)	% T.D.
2.000	Unquenched	4.25	98.2
2.000	Quenched	4.25	97.9
1.992	Unquenched	4.23	97.6
1.992	Quenched	4.24	96.2
1.985	Unquenched	4.22	95.4
1.985	Quenched	4.23	94.6
1.972	Unquenched	4.29	97.2
1.972	Quenched	4.22	97.3
1.934	Unquenched	4.32	94.3
1.934	Quenched	4.30	92.4

Figure 5.11 (a) and (b) display the EBSD maps and grain sizes of the polycrystalline TiO_2 samples prepared without additional heat treatment and after subsequent annealing and quenching process, respectively. The grain of unquenched and quenched TiO_2 exhibited random orientations, and grain sizes with the corresponding standard deviations were equal to $3\pm1\mu m$ and $5\pm2\mu m$, respectively. This results suggest that the average grain size of quenched TiO_2 was larger than that of unquenched TiO_2.

Table 5.4 Heat treatment and cooling conditions, calculated O/Ti ratios, and grain sizes obtained for the TiO_{2-x} specimens.

Reduction temperature (K)	Annealing temperature (K)	Cooling condition	O/Ti ratio (2-x)	Grain size (μm)
–	–	Unquenched	2.000 ± 0.002	3±1
–	1423	Quenched	2.000 ± 0.003	5±2
1243	–	Unquenched	1.992 ± 0.002	4±1
1243	1423	Quenched	1.992 ± 0.003	6±2
1273	–	Unquenched	1.985 ± 0.002	4±1
1273	1423	Quenched	1.985 ± 0.003	6±2
1343	–	Unquenched	1.972 ± 0.002	4±1
1343	1423	Quenched	1.972 ± 0.003	11±3
1423	–	Unquenched	1.934 ± 0.002	5±2
1423	1423	Quenched	1.934 ± 0.003	16±3

According to Table 5.4, the average grain sizes and geometric standard deviations of the unquenched and quenched $TiO_{1.992}$, $TiO_{1.985}$, $TiO_{1.972}$, and $TiO_{1.934}$ were 4±1μm, 4±1μm, 4±1μm, 5±2μm, 6±2μm, 6±2μm, 11±3μm, and 16±3μm, indicating that the grain sizes of both series was increased with decreasing the O/Ti ratio and after quenching. The change of grain size is related to growth of grain, which is a result of diffusion of atom [9]. The atomic diffusion increased with increasing temperature and decreasing O/Ti ratio. Since increased oxygen vacancies allow lower activation energy for atomic diffusion, the decreased O/Ti ratio would be attributed to accelerate atomic diffusion. A high oxygen vacancies and high annealing temperature correspond to decreasing O/Ti ratio and after quenching.

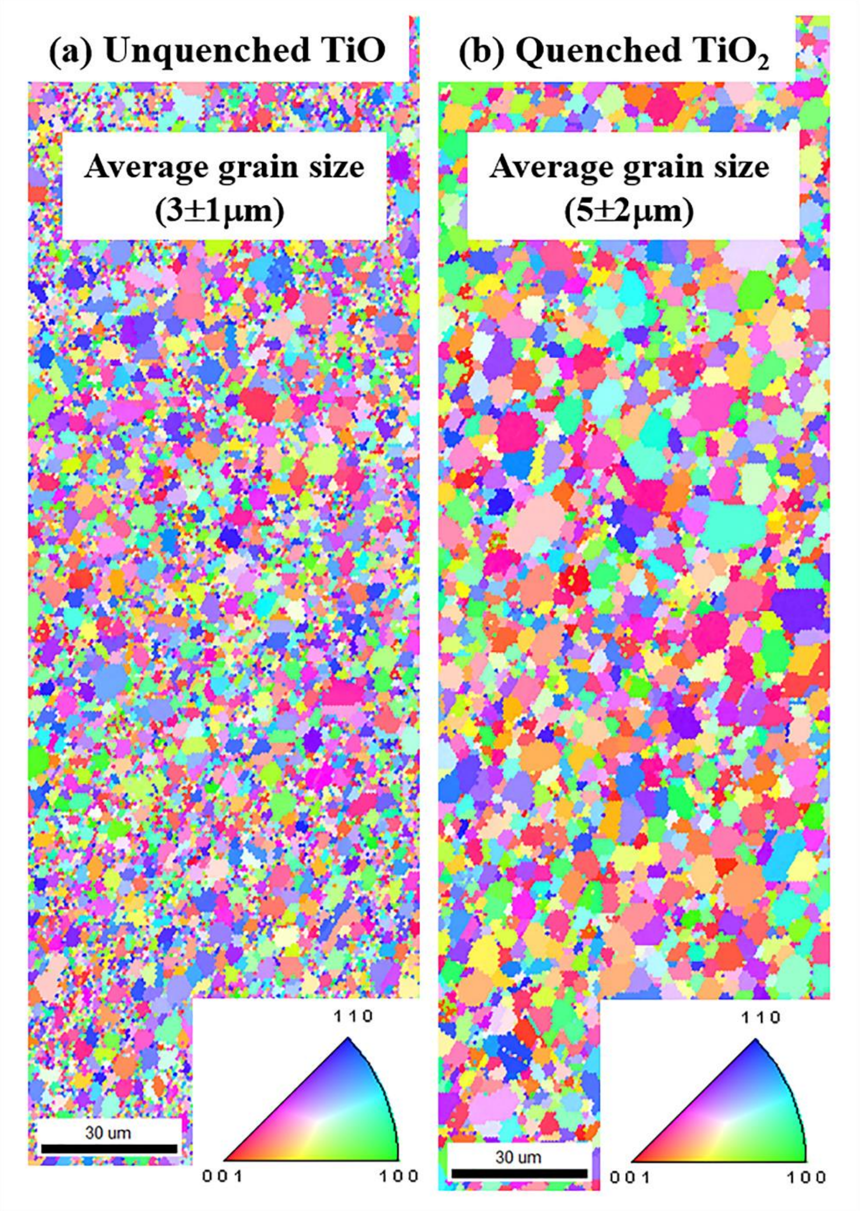

Figure 5.11 EBSD maps obtained for the (a) unquenched and (b) quenched TiO_2.

5.3.1 Elastic properties

The experimentally observed sound velocities and calculated Debye temperature and elastic properties are summarized in Table 5.5 and 5.6. The values of v_L, v_s, B, G, E, β, and θ_D of the studied TiO$_2$ specimens agree well with the published values [10-16].

Table 5.5 Sound velocities and Debye temperature of the unquenched and quenched TiO$_{2-x}$ specimens.

O/Ti	Colling condition	Defect type	Longitudinal sound velocity, V_L (m/s)	Shear sound velocity, V_S (m/s)	Debye temperature, θ_D (K)
2.000	-	Defect-free	9290[21]	5190[21]	778.0[27]-782.5[28]
2.000	Unquenched	Defect-free	9299±5	5204±13	789.8±1.8
2.000	Quenched	Defect-free	9305±5	5220±13	792.1±0.1
1.992	Unquenched	Point & Planar	8702±3	5083±85	768.6±11.7
1.992	Quenched	Point	9009±12	5182±58	784.3±8.1
1.985	Unquenched	Point & Planar	8596±11	5056±15	763.5±2.1
1.985	Quenched	Point	8926±82	5151±48	779.4±9.4
1.972	Unquenched	Point & Planar	8136±16	4941±55	743.8±7.6
1.972	Quenched	Point & Planar	8365±50	5050±32	760.7±0.4
1.934	Unquenched	Planar	7846±2	4767±49	714.7±6.8
1.934	Quenched	Planar	7957±56	4770±42	715.9±9.8

Table 5.6 Elastic moduli of the unquenched and quenched TiO_{2-x} specimens.

O/Ti	Colling condition	Defect type	Bulk modulus, B (GPa)	Shear modulus, G (GPa)	Young's modulus, E (GPa)	Compressibility, β (GPa^{-1})
2.000	-	Defect-free	211.0[22]- 212.0[23]	112.0[24]- 113.0[23]	290.0[25]	0.0047[26]
2.000	Unquenched	Defect-free	210.7±1.0	113.4±1.0	288.4±1.0	0.0048±0.0003
2.000	Quenched	Defect-free	210.7±0.2	114.0±0.1	289.8±0.1	0.0048±0.0001
1.992	Unquenched	Point & Planar	172.7±4.8	108.1±3.6	268.4±6.2	0.0058±0.0002
1.992	Quenched	Point	183.8±2.4	108.8±4.5	272.6±4.5	0.0056±0.0007
1.985	Unquenched	Point & Planar	166.5±1.3	106.9±0.6	264.2±1.0	0.0060±0.0001
1.985	Quenched	Point	181.1±23.7	108.4±2.0	271.2±10.4	0.0056±0.0008
1.972	Unquenched	Point & Planar	140.3±1.9	101.9±2.3	246.0±3.7	0.0071±0.0001
1.972	Quenched	Point & Planar	151.8±2.4	107.9±3.8	261.3±6.9	0.0066±0.0001
1.934	Unquenched	Planar	130.0±2.5	94.5±2.0	228.2±3.4	0.0077±0.0003
1.934	Quenched	Planar	139.7±3.8	93.2±1.7	217.8±1.8	0.0101±0.0003

Figure 5.12 shows the v_B of the unquenched and quenched TiO_{2-x} samples plotted depending on O/Ti ratios. In both types of samples, the values v_B decreased as O/Ti decrease. At the same values of O/Ti, however, a small discrepancy was observed between unquenched and quenched TiO_{2-x}. While the v_B of the unquenched TiO_2 and $TiO_{1.934}$ were almost same with quenched TiO_2 and $TiO_{1.934}$, respectively, the magnitudes of unquenched $TiO_{1.992}$, $TiO_{1.985}$, and $TiO_{1.972}$ specimens were 2.1-2.3% lower than those for the quenched samples with the same compositions, which would be attributed to the presence of different defects types. The results indicates that the observed 2% reduction in the sound velocity induced by planar defects would be attributed to a 2% reduction in the thermal conductivity based on kinetic theory for phonon:$\kappa = 1/3vCl$, where v is the phonon velocity, C is the phonon heat capacity, and l is the phonon mean free path). Thus, the effect induced by planar defects on the average sound velocity is relatively small.

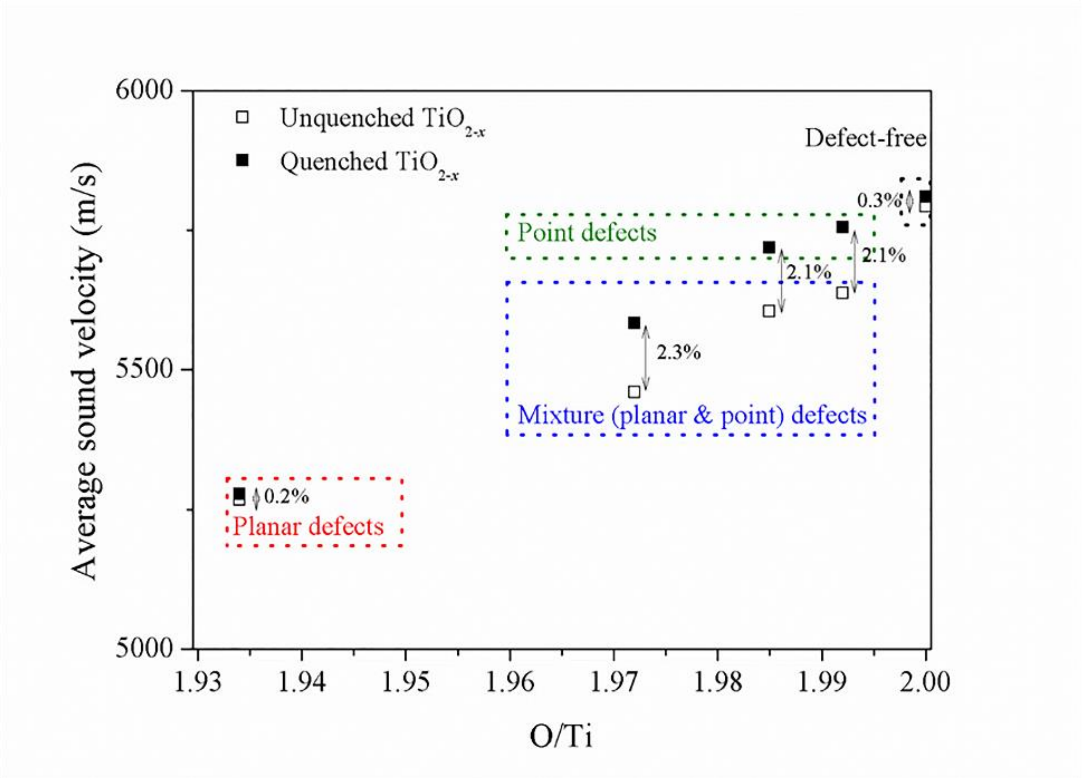

Figure 5.12 Average sound velocities for the unquenched and quenched TiO_2 and TiO_{2-x} ($2-x$ = 1.992, 1.985, 1.972, and 1.934).

5.3.2 Electrical properties

The carrier densities and mobilities of both series TiO_{2-x} sample are shown in Fig. 5.13 (a) and (b). The carrier concentration was increased as O/Ti ratio decrease regardless of the defect type because oxygen vacancies dominate it. And there is no significant differences in the carrier mobility between point and planar defects, which indicates almost equal effects on the carrier mobility. In case of $TiO_{1.934}$ with planar defect, 33% change of carrier mobility was observed. This result is closely related to the grain size; unquenched $TiO_{1.934}$ is ~3times smaller than quenched $TiO_{1.934}$. Thus larger grain size of quenched $TiO_{1.934}$ would be the cause of the higher carrier mobility in $TiO_{1.934}$ having planar defects due to weakened carrier scattering at the grain boundaries. Figure 5.13 (c) shows the O/Ti ratio dependence electrical conductivity of TiO_{2-x} at room temperature. The electrical conductivity was increased as O/Ti decrease due to increasing carrier density despite the large amount of oxygen vacancy.

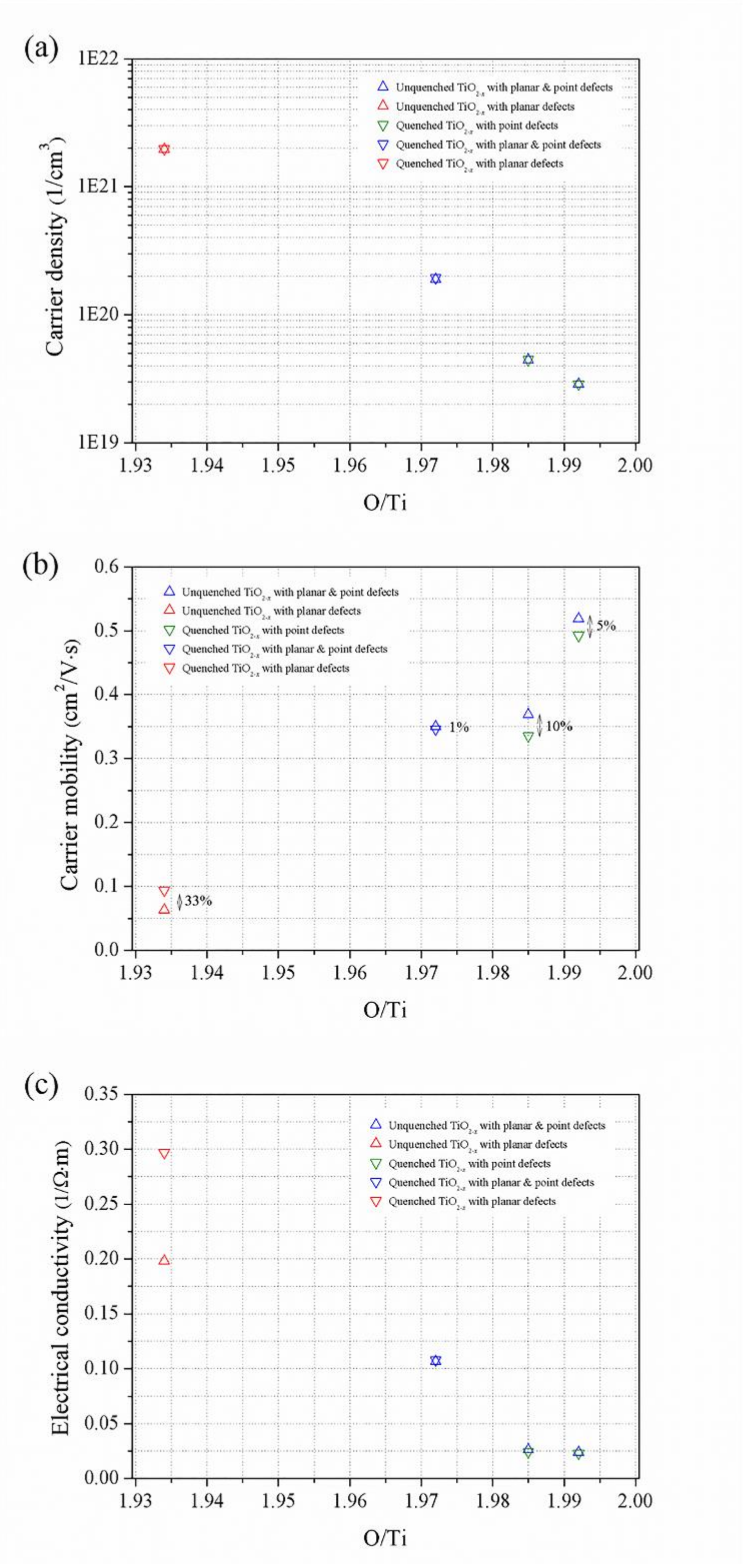

Figure 5.13 (a) Density of carrier, (b) mobility of carrier, and (c) electrical conductivity of the unquenched and quenched TiO_{2-x} ($2-x = 1.992$, 1.985, 1.972, and 1.934) as a function of the O/Ti ratio.

5.3.3 Thermal properties

Figure 5.14 and 5.15 shows the temperature dependent thermal conductivity of the both series of unquenched and quenched TiO_{2-x} (2-x = 2.000, 1.992, 1.985, 1.972, and 1.934) specimens. The thermal conductivities were corrected to 100% of the theoretical density by the Maxwell relation because the relative densities of the studied samples were 92-98%. The corrected thermal conductivities of the quenched and quenched TiO_2 samples were somewhat higher than those published by Harada et al [5]. This is because average grain sizes in present study were larger than the reference [5] because of the different preparation methods. The large grain sizes produce the higher thermal conductivity of the TiO_2 due to the weak phonon-grain boundary scattering. The thermal conductivities of non-stoichiometric TiO_{2-x} samples corresponded to the sum of lattice (κ_L) and electrical (κ_e) thermal conductivity. The magnitude of κ_e is related to the electrical conductivity (σ) by the Wiedemann-Franz law, $\kappa_e = \sigma LT$, where L is the Lorenz number ($2.44 \times 10^{-8}\ W\Omega\mathrm{K}^{-2}$). As shown in Fig. 5.14 and 5.15, the thermal conductivities of the both unquenched and quenched TiO_2 were dependent on T. The temperature dependent thermal conductivity of the unquenched TiO_{2-x} was decreased as oxygen vacancy concentration increase and reached a constant. Especially, the temperature dependent thermal conductivities of quenched $TiO_{1.992}$ and $TiO_{1.985}$ samples were more sensitive to temperature than those of the quenched samples having same compositions. This results suggest that the temperature dependent thermal conductivity of TiO_{2-x} was affected not only the amount of oxygen vacancy, but also by the defect type. In case of amorphous materials, the mean free path is as short as the atomic distance, independent of thermal conductivity. The thermal conductivity of Magnéli phase has temperature independence behavior like amorphous materials. That is, the Magnéli phase could be attributed to change effective phonon scattering center; since planar defects limit the phonon mean free path, the phonon-phonon Umklapp scattering seem to be disappeared or become relatively small.

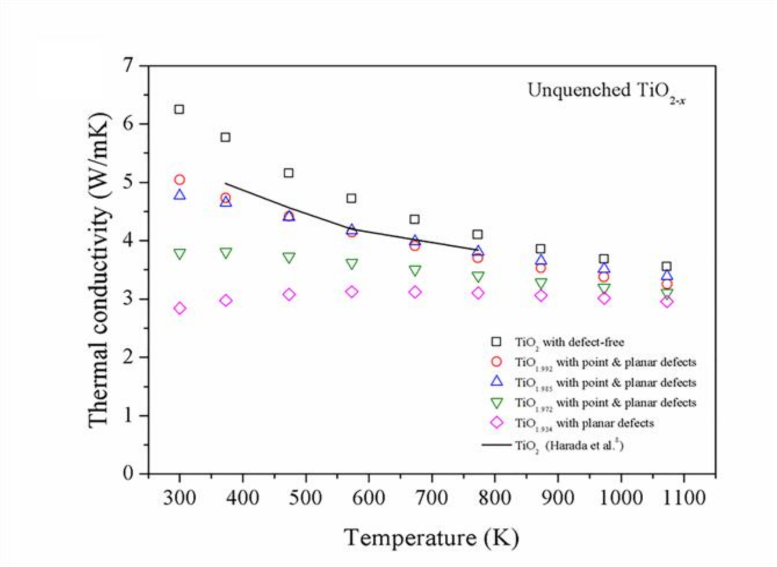

Figure 5.14 Thermal conductivities of the unquenched TiO_2 and TiO_{2-x} ($2-x$ = 1.992, 1.985, 1.972, and 1.934) samples plotted as functions of temperature.

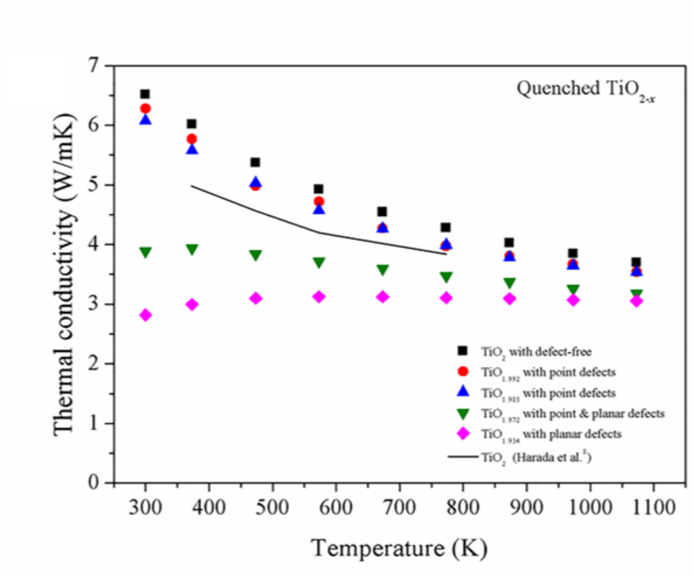

Figure 5.15 Thermal conductivities of the quenched TiO_2 and TiO_{2-x} ($2-x$ = 1.992, 1.985, 1.972, and 1.934) samples plotted as functions of temperature.

The unquenched $TiO_{1.992}$ and $TiO_{1.985}$ specimens containing point and planar defects as well as the quenched $TiO_{1.992}$ and $TiO_{1.985}$ specimens including only point defects were investigated to compare the effects induced by point and planar defects on the phonon scattering. The maximum κ_e of TiO_{2-x} was $2.17 \times 10^{-6}\ \mathrm{Wm^{-1}K^{-1}}$, which was calculated for the $TiO_{1.934}$ sample containing planar defects, and the electron contribution to the thermal conductivity was much smaller than the phonon contribution. That is, the electrical thermal conductivity was negligible as compared to the lattice thermal conductivity. Therefore, the total thermal conductivity was considered as lattice thermal conductivity in this work. The magnitude of thermal conductivity of the samples including point defects (randomly distributed oxygen vacancies) was estimated by the empirical thermal conductivity model based on Klemens-Callaway model, which is based on the Boltzmann phonon transport equation and relaxation time approximation, assumed that all phonon scattering processes were represented by the frequency-dependent relaxation time. Also the phonon-oxygen vacancies scattering was equivalent to phonon-defect scattering. Hence, the phonon scattering induced by the defects was calculated by taking into account the missing masses and linkages calculated for oxygen vacancies and the host lattice.

The total relaxation time is given by:

$$\tau_{total}{}^{-1} = \tau_U{}^{-1} + \tau_P{}^{-1} + \tau_B^{-1} \tag{5.6}$$

$$\tau_U{}^{-1} = B_U T \omega^2 \exp(-\theta/3T) \tag{5.7}$$

$$\tau_P{}^{-1} = A\omega^4 \tag{5.8}$$

$$\tau_B{}^{-1} = v_B/l_{gb} \tag{5.9}$$

$$B_U \approx \hbar\gamma^2/M{v_B}^2\theta \tag{5.10}$$

The parameter *A* is described below; τ_U, τ_p, and τ_B are the relaxation times of phonon-phonon Umklapp scattering, phonon-point defect scattering, and grain boundary scattering, respectively. Moreover, l_{gb} is the average diameter of grains, In this work, the magnitude of B_U was determined as $\gamma = 1.4$ [17], which was previously reported for defect-free TiO_2.

For point-defect scattering:

$$A = \frac{\Omega_0}{4\pi v_B^3}\Gamma_M \tag{5.11}$$

Since phonon scattering entirely occurs due to the oxygen vacancies, the mass perturbation of cation sites is constant. For the TiO_{2-x} compound composed of the sub-lattice and vacancies, the scattering strength Γ_M can be written as:

$$\Gamma_M = x(1-x)\left(\frac{2M+M_O}{M}\right)^2 \tag{5.12}$$

where *x* is the concentration of point defects, and M_O is the mass of the oxygen atom. The average atomic mass calculated for unit cell M is equal to

$$M = \frac{M_{Ti}+(2-x)M_O}{3} \tag{5.13}$$

Here M_{Ti} is the average atomic mass of Ti sites.

The measured and estimated thermal conductivities of the quenched and quenched $TiO_{1.992}$ and $TiO_{1.985}$ samples were shown in Fig. 5.16. The theoretical thermal conductivities of both samples followed the trend measured thermal conductivities above 773 K regardless of the annealing and quenching processing. The estimated thermal conductivities of the quenched $TiO_{1.992}$ and $TiO_{1.985}$ samples including only point defects agree well with the measured values. However, thermal conductivities of the unquenched samples containing both point and planar defects with same compositions exhibited significant discrepancies between the estimated and measured values in the temperature range below 773 K (~θ_D). Such relatively large discrepancies could be attributed to the effect induced by planar defects. From the results, the following conclusions can be drawn. i) The planar defects in the unquenched $TiO_{1.992}$ and $TiO_{1.985}$ samples including both point and planar defects plays an important role in the phonon scattering process at $T < \theta_D$, which decreases the thermal conductivity of sample and thus produces a deviation between the estimated and measured values. ii) At $T > \theta_D$, since the phonon-phonon Umklapp scattering process becomes very strong and may dominate over other scattering processes, the point or planar defects have little impact on the phonon-defect scattering process.

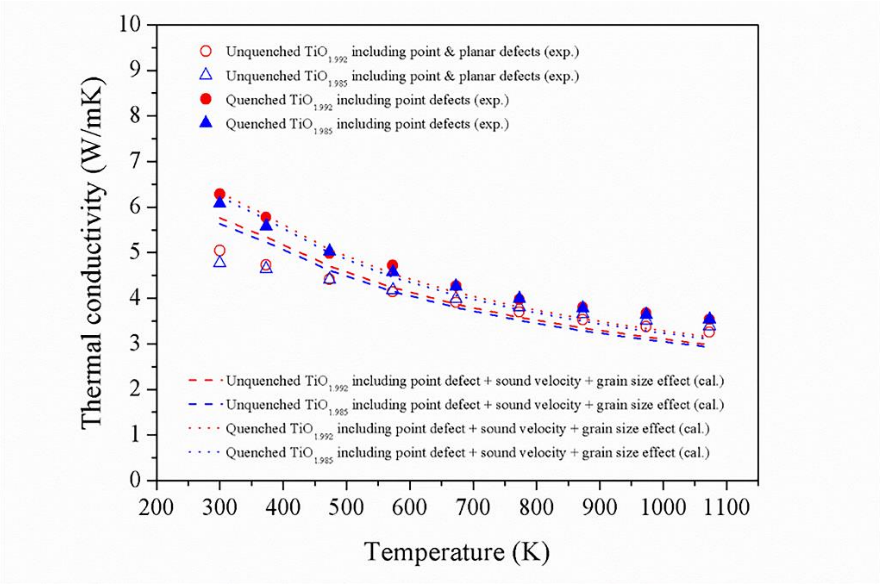

Figure 5.16 Experimental and calculated thermal conductivities of the unquenched and quenched TiO_{2-x} ($2-x$ = 1.992 and 1.985) specimens plotted as functions of temperature.

Figure 5.17 shows the room temperature thermal conductivities of the quenched and quenched TiO_2 and TiO_{2-x} samples depending on O/Ti ratio. As shown in Fig. 5.17, thermal conductivity was decreased as O/Ti ratio decrease. It noted that since the measurements reveal higher values of thermal conductivity for samples with small grain in both quenched and unquenched samples, the grain boundary scattering process seems to be only a minor effect. This tendency is the different compared to many other recent studies on oxides. The thermal conductivity of unquenched $TiO_{1.992}$ and $TiO_{1.985}$ specimens including both point and planar defects were lower by 20% and 22% than the magnitudes of the quenched $TiO_{1.992}$ and $TiO_{1.985}$ samples containing point defects, respectively. These results clearly indicate that planar defects produce a stronger effect on the phonon scattering process comparing with point defects.

The room temperature thermal conductivities of the unquenched and quenched TiO_{2-x} samples were calculated by the empirical thermal conductivity model based on Klemens-Callaway model. The estimated and measured thermal conductivities were shown in Fig. 5.17 (b) and (c). The estimations exhibited larger discrepancy with the measured values as O/Ti ratio decrease. The theoretical thermal conductivities of the quenched TiO_{2-x} including only point defects agree well with the measured values, which means the theoretical model was able to describe the effects of the scattering of phonon-point defect and phonon-grain boundary and sound velocity caused by the reduction thermal conductivity with high accuracy. In contrast, the measured thermal conductivities of the TiO_{2-x} samples including planar defects exhibited much larger deviations from the theoretical data. Besides the differences became larger with decreasing O/Ti, which would be attributed to the effect of planar defects on the thermal conductivity. It noted that a larger fraction of phonons are scattered by planar defects comparing with point defects; thus thermal conductivity of TiO_{2-x} strongly depends on the amount of planar defects.

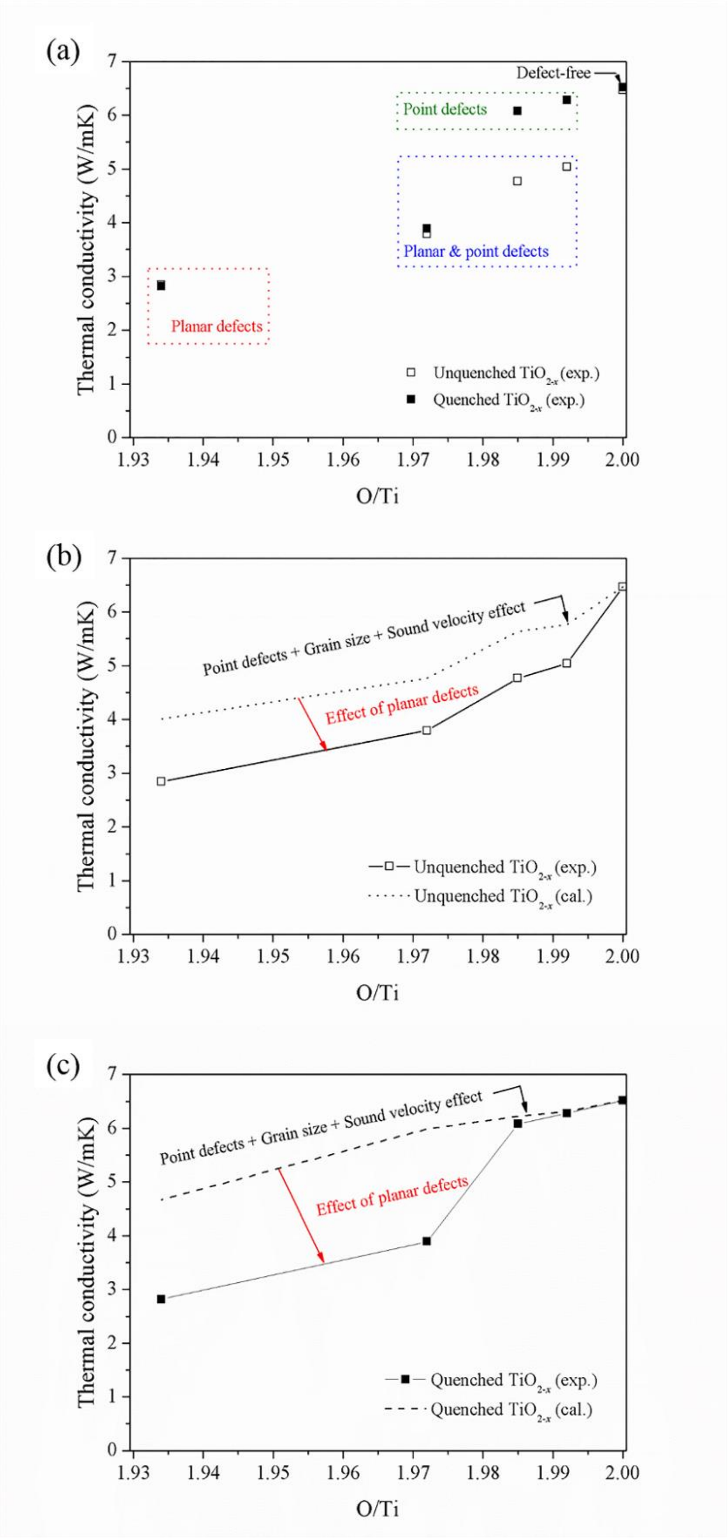

Figure 5.17 O/Ti ratio dependences of the (a) measured thermal conductivities of the unquenched and quenched TiO_2 and TiO_{2-x} ($2-x$ = 1.992, 1.985, 1.972, and 1.934) specimens, and calculated thermal conductivities of the (b) unquenched and (c) quenched TiO_{2-x} samples at room temperature.

In order to estimate the phonon scattering of planar defects, I made an assumption that planar defects is a high concentration of oxygen vacancies because the planar defects originate from the oxygen vacancies. The relaxation time of planar defect τ_{planar} can be expressed as

$$\tau_{planar}{}^{-1} = F \times \tau_{point}{}^{-1} \tag{5.14}$$

where F is the adjustable parameter. The thermal conductivity was reproduced by Eq. (5.14) as shown in Fig. 5.18. The calculated results captured the behavior of the experimentally obtained thermal conductivity of unquenched TiO_{2-x}. The obtained F was 1.49.

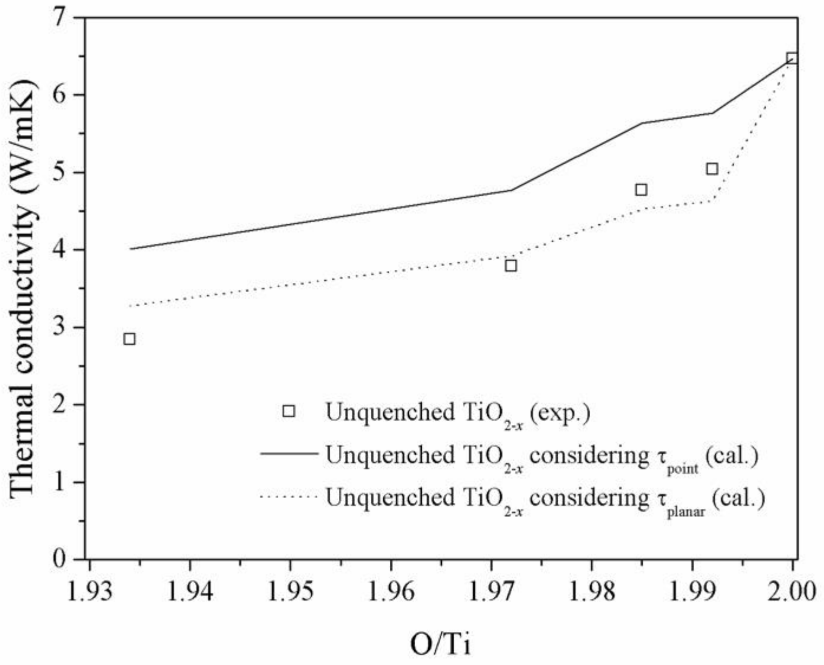

Figure 5.18 O/Ti ratio dependence of thermal conductivity of unquenched TiO_{2-x}: measured value (unfilled square), calculated value considering relaxation time for point defect (solid line) and for planar defect (dot line).

This relaxation time approximation is a new approach for planar defects scattering. The newly proposed relaxation time of phonon-planar defect scattering gives prediction on the model such as estimating reduction thermal conductivity. For instance, the thermal conductivities of Ga_2Te_3 were unexpectedly low due to planar defects [18]. We build the empirical thermal conductivity model based on Klemens-Callaway model to clarify whether or not term of relaxation time for phonon-planar defect scattering is an appropriate for material including planar defects. In present study, thermal conductivity of Ga_2Te_3 with planar type vacancy is considered to that of In_2Te_3 with planar type vacancy because Ga and In are same group in the periodic table which has similar physical characteristics.

The total relaxation time for In_2Te_3 with point type vacancy can be expressed as ${\tau_{total}}^{-1} = {\tau_U}^{-1} + {\tau_{In\,vacancy}}^{-1}$, where τ_U and $\tau_{In\,vacancy}$ are the relaxation times of phonon-phonon Umklapp scattering and phonon-In^{3+} cation vacancy scattering, respectively. The relaxation time of phonon-In^{3+} cation vacancy scattering is ${\tau_{In\,vacancy}}^{-1} = A\omega^4$. Parameter A is described by:

$$A = \frac{\Omega_0}{4\pi v_B^3}\Gamma \tag{5.15}$$

where Ω_0 and v_B are the atomic volume and average sound velocity of In_2Te_3 [19] and Γ_M is the phonon scattering parameter. Then, the scattering parameter can be written by considering as $In_2VA_1Te_3$:

$$\Gamma \approx \Gamma_M = \frac{1}{3}\left(\frac{\bar{M}_{In-site}}{\bar{M}}\right)^2 \tag{5.16}$$

where $\bar{M}$ is the total average atomic mass, $\bar{M}_{In-site}$ is the average atomic mass on the In-sub-lattice. The relaxation time of Umklapp scattering is given by

$${\tau_U}^{-1} = B_U T\omega^2 \exp(-\theta/3T) \tag{5.17}$$

$$B_U \approx \frac{\hbar\gamma^2}{M v_B^2 \theta} \tag{5.18}$$

where M is the average mass of all atoms. The γ is an adjustable parameter as compared to experimentally observed thermal conductivity of In_2Te_3 with point type vacancy.

The total relaxation time for Ga_2Te_3 with planar type vacancy can be expressed as ${\tau_{total}}^{-1} = {\tau_U}^{-1} + {\tau_{Planar}}^{-1}$, where τ_U and τ_{planar} are the relaxation times of phonon-phonon Umklapp scattering and phonon-planar defect scattering, respectively. The relaxation time of phonon-planar defects scattering is ${\tau_{planar}}^{-1} = F \times {\tau_{oxygen}}^{-1}$. The parameter F is 1.49. The relaxation time of phonon-oxygen vacancies scattering is ${\tau_{oxygen}}^{-1} = A\omega^4$. Parameter A is described by:

$$A = \frac{\Omega_0}{4\pi v_B^3}\Gamma_M \tag{5.19}$$

where Ω_0 and v_B are the atomic volume and average sound velocity of In_2Te_3 [19], respectively. The calculation of the scattering coefficient for a compound composed of several sub-lattices is more complicated. For a ternary compound composed of three sub-lattices $U_{x_1}, V_{y_1}, W_{z_1}$, which corresponds to In_2,VA_1,Te_3, Γ_M is given by:

$$\Gamma_M = \frac{x_1}{(x_1+y_1+z_1)}\left(\frac{\bar{M}_U}{\bar{M}}\right)^2 \Gamma_M(U) + \frac{y_1}{(x_1+y_1+z_1)}\left(\frac{\bar{M}_V}{\bar{M}}\right)^2 \Gamma_M(V) + \frac{z_1}{(x_1+y_1+z_1)}\left(\frac{\bar{M}_W}{\bar{M}}\right)^2 \Gamma_M(W) \quad (5.20)$$

where $\overline{M_U}$, $\overline{M_V}$, and $\overline{M_W}$ are average masses at the *U*-, *V*-, and *W*-sites, respectively. Since phonon scattering entirely occurs due to the In^{3+} vacancies, the mass perturbation of Te^{2-} anion sites is constant. For the $In_2VA_1Te_3$ compound composed of the In^{3+} sub-lattice and vacancies, the total scattering strength Γ_M represents the scattering strength caused by the mass for each site and can be written as:

$$\Gamma_M = \frac{x_1}{(x_1+y_1+z_1)}\left(\frac{\bar{M}_U}{\bar{M}}\right)^2 \Gamma_M(U) + \frac{z_1}{(x_1+y_1+z_1)}\left(\frac{\bar{M}_W}{\bar{M}}\right)^2 \Gamma_M(V) \quad (5.21)$$

The VA_1 is 1/3 vacancy in cation sites. Plus, Plus, mass perturbation of In^{3+} vacancies are considered as that of oxygen vacancies to express in terms of $\tau_{Planar}{}^{-1}$. Thus, similar to oxygen vacancies scattering, Γ_M can be written as:

$$\Gamma_M = \frac{1}{3}\frac{z_1}{(x_1+y_1+z_1)}\left(\frac{2M+M_{In\,vacancy}}{M}\right)^2 \quad (5.22)$$

where $M_{In\,vacancy}$ is the mass of the missing indium atom. The average atomic mass calculated for unit cell M is equal to

$$M = \frac{2M_{In}+M_{In\,vacancy}}{6} \quad (5.24)$$

From Eq. (5.14), Eq. (5.22) is given by

$$\Gamma_M = \frac{1}{3}\frac{z_1}{(x_1+y_1+z_1)}\left(\frac{2M+M_{In\,vacancy}}{M}\right)^2 \times F \quad (5.25)$$

Figure 5.19 shows the estimated thermal conductivity of In_2Te_3 with point and planar type vacancy together with the experimentally observed thermal conductivity. As shown in Fig. 5.19 as dotted line, the estimated thermal conductivity for In_2Te_3 with point type vacancy, which considers both phonon-phonon Umklapp scattering and phonon-point type In vacancy scattering mechanisms, agrees well with the measured thermal conductivity. A reasonable fit to the experimental data was achieved considering the uncertainty involved in determining the γ, which value is 1.91. The calculation curve, including the effect of planar defect scattering with considering the phonon-phonon Umklapp scattering, is shown in Fig. 5.19 as solid line. The calculated thermal conductivities conform well to the trend of experimentally observed thermal conductivity, even though we did not use any fitting parameters. The obtained results were used in the summary sections for comparing effect of each scattering process on reduction in thermal conductivity.

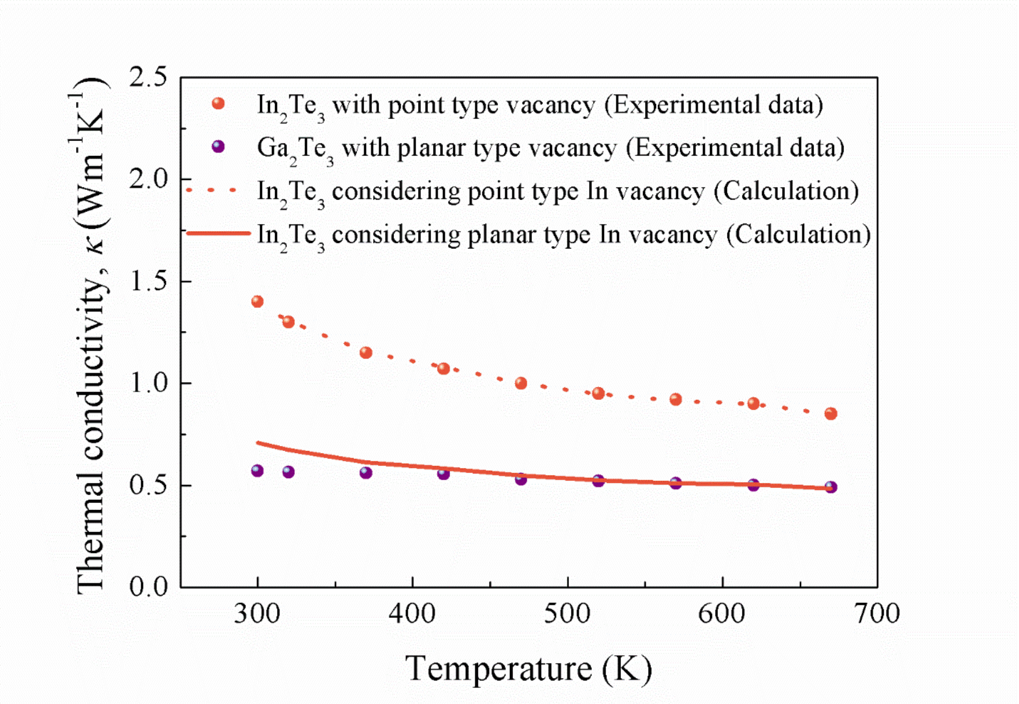

Figure 5.19 Measured thermal conductivities Ga_2Te_3 with planar type vacancy and In_2Te_3 with point type vacancy and calculated thermal conductivities In_2Te_3 with point or planar type vacancy at various temperatures. Solid symbol: experimentally observed value. Dotted line: calculated value including the effect of phonon-phonon Umklapp scattering and phonon-point type In vacancy scattering (${\tau_U}^{-1} + {\tau_{point\ type}}^{-1}$). Solid line: calculated value including the effect of phonon-phonon Umklapp scattering, phonon-point type In vacancy scattering, and phonon-planar type In vacancy scattering (${\tau_U}^{-1} + {\tau_{planar\ type}}^{-1}$).

5.4 Conclusions

The correlation between the thermal conductivity and the defect type in TiO_{2-x} ($2-x$ = 2.000, 1.992, 1.985, 1.972, and 1.934) including point (randomly distributed oxygen vacancies) and planar defects (ordered oxygen vacanacies) was studied as a function of the O/Ti ratio. Two series of the TiO_{2-x} samples having point or planar defects were prepared by different heat treatment procedures. The average sound velocity of the TiO_{2-x} ($2-x$ = 1.992 and 1.985) samples having planar defects was lower than value obtained for the specimens having point defects by about 2% at room temperature. However, the thermal conductivity of the TiO_{2-x} ($2-x$ = 1.992 and 1.985) samples having planar defects was approximately 22% lower than that of the TiO_{2-x} ($2-x = 1.992$ and 1.985) specimens having point defects, suggesting that strong phonon scattering induced by planar defects might be attributed to the significant reduction in thermal conductivity. On the contrary, the carrier mobility of TiO_{2-x} having planar defects was similar to that of TiO_{2-x} having point defects, indicating that the effect of planar defects on the carrier mobility was almost equivalent to the effect produced by point defects. In order to clarify the effect of planar defects on the phonon scattering processes, the thermal conductivities of two different types of TiO_{2-x} (including both point and planar defects) were analyzed using the empirical thermal conductivity model based on Klemens-Callaway model, which took into account the effects of point defects, grain size, and sound velocity. The estimated thermal conductivity of the TiO_{2-x} specimen with randomly distributed oxygen vacancies was in agreement with experimentally observed thermal conductivity. In contrast, the observed thermal conductivity of TiO_{2-x} having planar defects was much lower than the estimated thermal conductivity. Thus, the results of theoretical estimations suggest that planar defects scatter phonons in the TiO_2 lattice more effectively than point defects. A model for relaxation time of the phonon-planar defects scattering rates successfully fits the data containing planar defects.

5.5 References

[1] J.S. Andersson, B. Collén, U. Kuylenstierna, *Acta Chem Scand.* **11** 1641 (1957).

[2] J.S. Anderson, B.G. Hyde, *J Phys Chem Solid.* **28** 1393 (1967).

[3] R.R. Merritt, B.G. Hyde, *Proc. R. Soc. London, Ser. A* **274** 627 (1973).

[4] L.A. Bursill, B.G. Hyde, *Proc. R. Soc. London, Ser. A*, **375** 105 (1981).

[5] S. Harada, K. Tanaka, H. Inui, *J Appl Phys.* **108** 083703 (2010).

[6] D.L. Lide. CRC Handbook of Chemistry and Physics. 71st ed. Boca Raton, FL: CRC Press; 1990–1991.

[7] H.E. Swanson, H.F. McMurdie, M.C. Morris, *Natl. Bur. Stand. (U.S.) Monogr.* **25** 188 (1969).

[8] M.E. Bowden, G.V. White, I.W.M. Brown, *Powder Diffraction.* **11** 60 (1996).

[9] S. Shukla, S. Seal, R. Vij, *Nano let*. **3** 397 (2003).

[10] R.K. Verma, *J Geophys Res.* **65** 757 (1960).

[11] L.C. Ming, M.H. Manghnani, *J Geophys Res Solid Earth.* **84** 4777 (1979).

[12] D.G. Isaak, J.D. Carnes, O.L. Anderson, *Phys Chem Miner*. **26** 31 (1998).

[13] E. Shojaee, M.R. Mohammadizdeh, *J Phys Condens Matter.* **22** 015401 (2010).

[14] G.J. Yang, C.J. Li, Y.Y. Wang, *Mater Lett*. **62** 1670 (2008).

[15] G.A. Samara, P.S. Peercy, *Phys Rev B*. **7** 1131 (1973).

[16] A.Y. Wu, R.J. Sladek, *Phys Rev B*. **25** 5230 (1982).

[17] P.G. Klemens, *Physica B Condens Matter.* **263–264** 102 (1999).

[18] K. Kurosaki, H. Matsumoto, A. Charoenphakdee, S. Yamanaka, M. Ishimaru, Y. Hirotsu, *App. Phys. Lett*. **93** 012101 (2008).

[19] O. Madelung, *Semiconductors: Data Handbook* (Verlag Berlin Hendelberg, Springer, 2004).

CHAPTER VI

Summary and Conclusions

In the present study, impact of various way on phonon scattering process is investigated; oxygen vacancies, planar defects, and lone pair electrons through bulk compounds (e.g., $(La_{1-x}Ba_x)_2Mo_2O_{9-\delta}$, unquenched TiO_{2-x}, quenched TiO_{2-x}, $(La_{1-x}Bi_x)_2Mo_2O_9$). In order to capture each scattering rate, I build empirical thermal conductivity model based on Klemens-Callaway model, which represents the phonon scattering processes by frequency-dependent relaxation times with the Debye phonon approximation and several other assumptions. The purpose of this study is the modification of oxides for applications, such as refractory, thermal barrier coating, and thermoelectric conversion. The systematic analysis of the properties and new model of estimation for phonon scattering offer possibilities for those application field.

Thermophysical properties of barium and bismuth doped lanthanum molybdate and reduced titanium oxide were systematically evaluated and analyzed using empirical thermal conductivity model. The results that were obtained this study are summarized as follow:

(1) In chapter III, thermal conductivity was decreased with Ba substitution. The thermal conductivity of Ba-doped $La_2Mo_2O_9$ was decreased with increasing Ba concentration. Oxygen vacancies induced by different charge balance between La^{3+} and Ba^{2+} contribute to phonon scattering. The 13% reduction of thermal conductivity caused by Ba doping was mainly attributed to the phonon-oxygen vacancies scattering, while the mass perturbation due to Ba atom has little impact on phonon scattering (see Fig. 6.1).

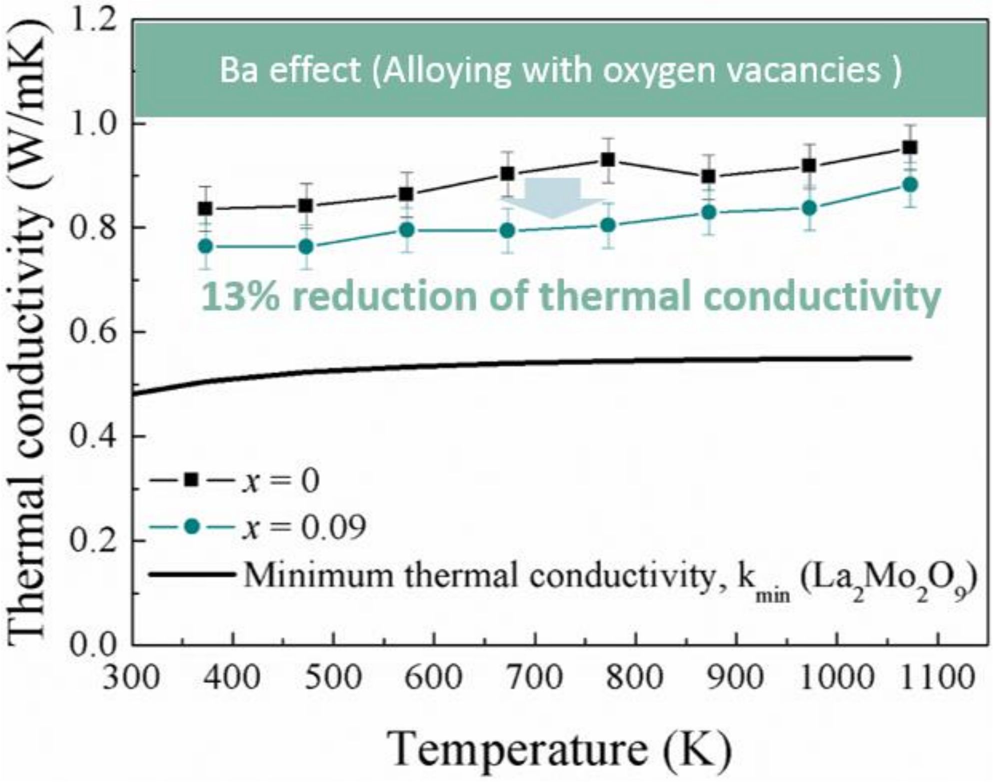

Fig. 6.1 Effect of Ba dopant on thermal conductivity in $(La_{1-x}Ba_x)_2Mo_2O_{9-\delta}$.

(2) In chapter IV, thermal conductivity was greatly decreased by Bi substitution. The Bi substitution contributes to the significant increase in thermal expansion coefficient, resulting in large Grüneisen parameter, which represents high anharmonicity. The enhanced anharmonicity induced by Bi^{3+} having lone pair electrons produces strong phonon scattering. The effect of enhancement of anharmonicity can be considered as phonon-phonon Umklapp scattering process. The 36% reduction of thermal conductivity caused by Bi doping was mainly attributed to the strong phonon-phonon Umklapp scattering, leading to a nearly minimum thermal conductivity (see Fig. 6.2), whereas the mass perturbation induced by Bi atom has little impact on phonon scattering. Enhancing the anharmonicity by substitution with Bi elements containing lone pair electrons is an effective method to reduce the thermal conductivity and almost reach minimum thermal conductivity.

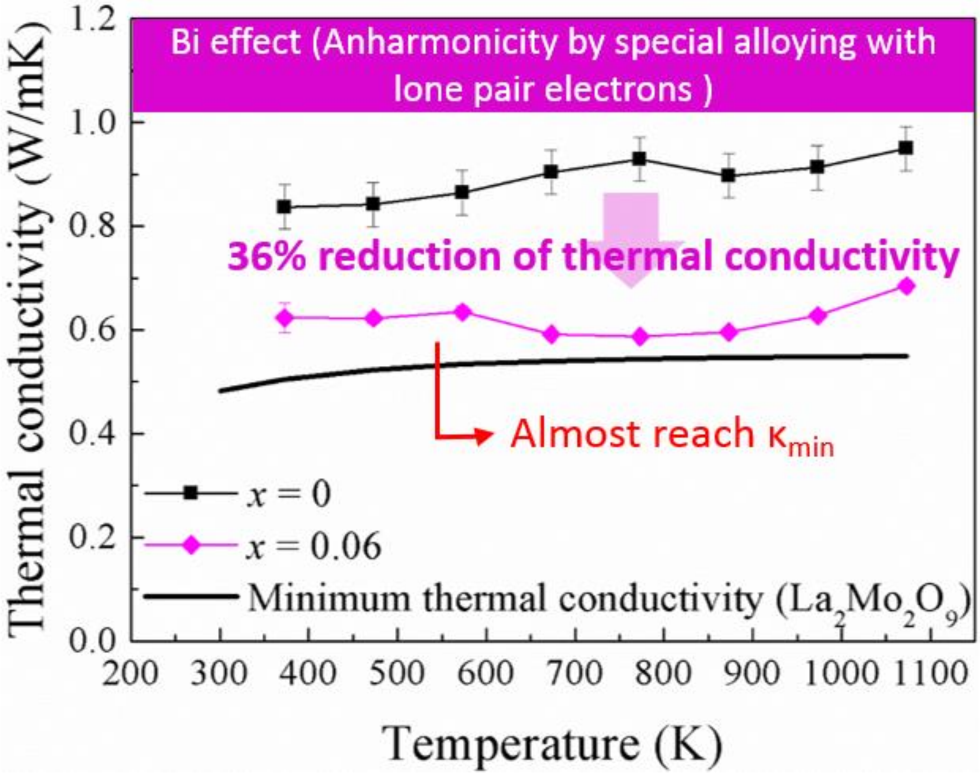

Fig. 6.2 Effect of Bi dopant on thermal conductivity in $(La_{1-x}Bi_x)_2Mo_2O_9$.

(3) In chapter V, thermophysical properties of titanium oxide including two types of defects was systematically evaluated and analyzed by empirical thermal conductivity model. The composition of TiO_{2-x} containing low concentration of oxygen vacancies was controlled by the O/Ti ratio and quenching conditions. The electrical conductivity was increased by concentration of oxygen vacancies. However, thermal conductivity strongly depends on defect type (e.g., point defect, planar defect). Thermal conductivity of TiO_{2-x} strongly depends on the concentration of planar defects. Planar defects more effectively reduce thermal conductivity than point defects and thermal conductivity of TiO_2 was 57% reduction thermal conductivity by planar defects (see Fig. 6.3).

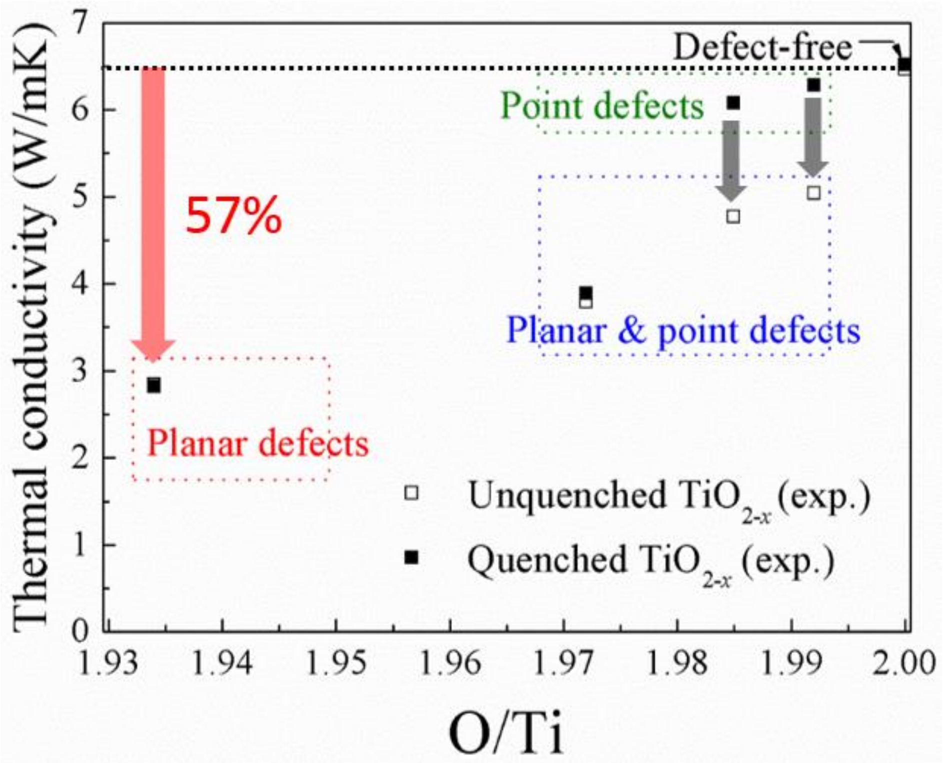

Fig. 6.3 Effect of planar defects on thermal conductivity in TiO_{2-x}.

In order to compare each scattering rate, the studied various scattering sources (e.g. Bi and Ba substitution, randomly distributed oxygen vacancies, ordered oxygen vacancies, enhancing anharmonicity by lone pair electrons) are applied to same material ($La_2Mo_2O_9$). As has been discussed in chapter III and IV, C_v and v were almost constant regardless of each scattering sources. Hence, thermal conductivity (κ) can be determined by relaxation time depending on different phonon scattering mechanisms in accordance with the formula $\kappa = 1/3C_v v^2\tau$. In Fig. 6.4, thermal conductivity of $La_2Mo_2O_9$ was calculated assuming total relaxation time as five ways: each effect of relaxation time such as Ba substitution τ_{Ba} ($\tau_{total} = \tau_{Ba}$), Bi substitution τ_{Bi} ($\tau_{total} = \tau_{Bi}$), randomly distributed oxygen vacancies (point defects) τ_{point} ($\tau_{total} = \tau_{oxygen}$), ordered oxygen vacancies (planar defects) τ_{planar} ($\tau_{total} = \tau_{Planar}$), and changing in anharmonicity induced by lone pair electrons τ_{LPE} ($\tau_{total} = \tau_{LPE}$) using Klemens-Callaway model.

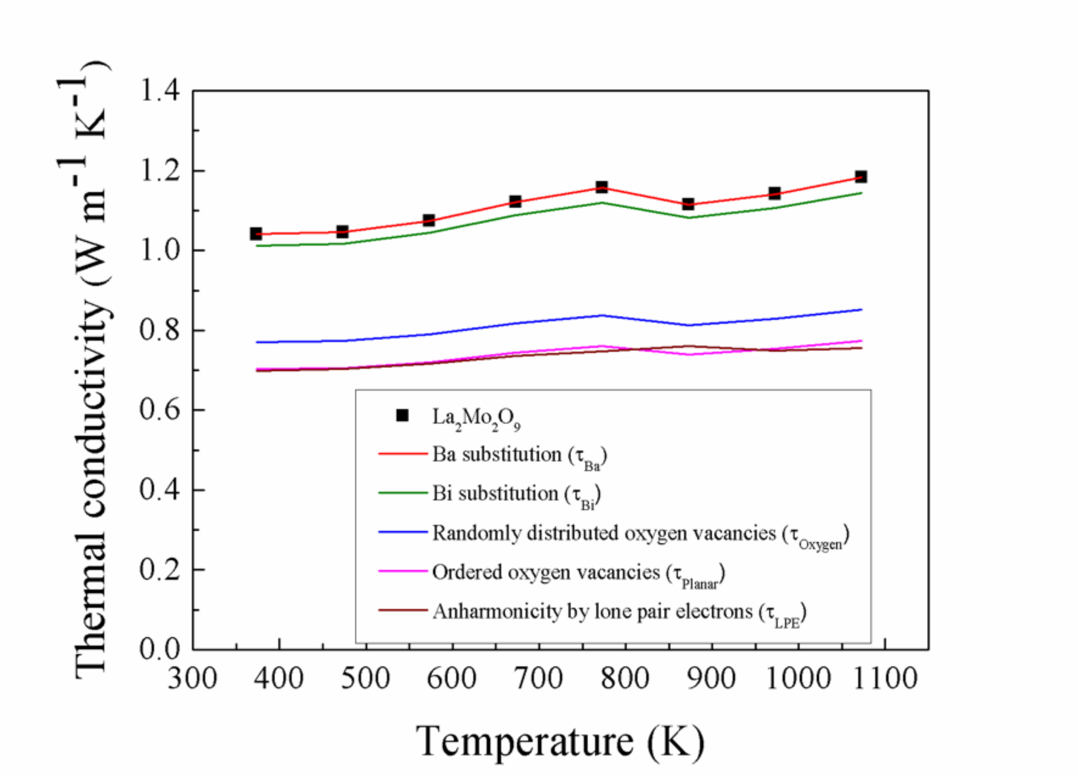

Figure 6.4 Comparison of the various phonon scattering effects on thermal conductivity of $La_2Mo_2O_9$ in the whole measured temperature ranges.

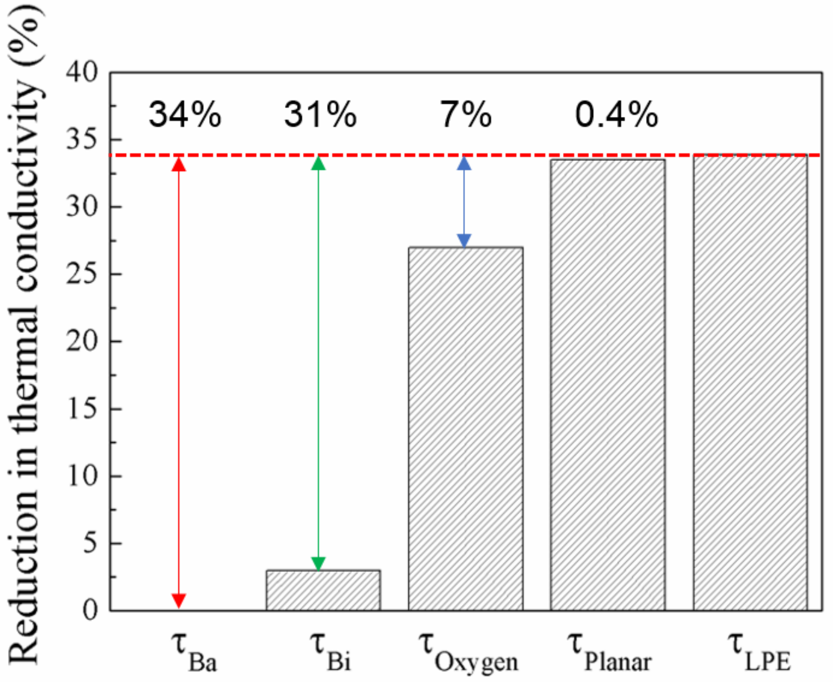

Figure 6.5 Comparison of the various phonon scattering on reduction in thermal conductivity of $La_2Mo_2O_9$.

The average reduction in thermal conductivity of each effect was calculated as compared to $La_2Mo_2O_9$ in temperature range from 373 to 1073K as shown in Fig. 6.5. The contributions of each phonon scattering (e.g., τ_{Ba}, τ_{Bi}, τ_{point}, τ_{planar}, τ_{LPE}) effect to reduction of the thermal conductivity were 0.002, 3, 27, 34, and 34%, respectively. The most effective phonon scattering source was enhancing anharmonicity induced by lone pair electrons. Interestingly, the effects of planar defects and enhancing the anharmonicity by lone pair electrons on reduction thermal conductivity are almost equal.

In conclusion, the phonon scattering source due to enhancing anharmonicity induced by lone pair electrons leads to nearly the minimum thermal conductivity. The strength of phonon-planar defects (ordered oxygen vacancies) scattering source is similar with enhancing anharmonicity induced by lone pair electrons. The low thermal conductivity induced by enhancing anharmonicity can apply to refractory, thermal barrier coating, and thermoelectric designs for the development of high-performance materials.

RESEARCH ACHIEVEMENTS

List of Publications

Research Articles

1. Effect of Ba concentration on phase stability and mechanical and thermal properties of $La_2Mo_2O_9$.
   Journal of the European Ceramic Society **37**, 281-288 (2017).
   KyungMin Ok, Yuji Ohishi, Hiroaki Muta, Ken Kurosaki, and Shinsuke Yamanaka.

2. Effect of point and planar defects on thermal conductivity in TiO_{2-x}.
   Journal of the American Ceramic Society **101**, 334-346 (2018).
   KyungMin Ok, Yuji Ohishi, Hiroaki Muta, Ken Kurosaki, and Shinsuke Yamanaka.

3. Bi-doped lanthanum molybdate: Enhancing the anharmonicity and reducing the thermal conductivity using Bi^{3+} with lone pair electrons.
   Ceramics International (under review).
   KyungMin Ok, Yuji Ohishi, Yusuke Mitazono, Hiroaki Muta, Ken Kurosaki, and Shinsuke Yamanaka.

List of Presentations

International Conference

1. Reduction of thermal conductivity in $La_2Mo_2O_9$ by substitution of Bi dopant.
   3rd International Conference on Smart Materials and Structures, Orlando, USA, March 20-22, (2017).
   KyungMin Ok, Yuji Ohishi, Hiroaki Muta, Ken Kurosaki, and Shinsuke Yamanaka.

Domestic Conference

1. Effect of Ba concentration on phase stability, mechanical and thermal properties of $La_2Mo_2O_9$.
   The Ceramic Society of Japan Annual Meeting, Okayama University, Okayama, Japan,

August 10-11, (2015).

KyungMin Ok, Yuji Ohishi, Hiroaki Muta, Ken Kurosaki, and Shinsuke Yamanaka.

ACKNOWLEDGEMENTS

I would like to express my deepest gratitude to my supervisor, Associate Professor Dr. Hiroaki Muta for his excellent guidance, caring, patience and providing me with an excellent atmosphere for doing research which kept me motivated throughout my PhD. I am also thankful for Associate Professor Dr. Ken Kurosaki. He gave me many helpful guidance and great advices on the present thesis. My sincere thank is expressed to the thesis committee, Professor Dr. Kitada Takanori and Professor Dr. Yamamoto Takao for their helpful suggestions on the present thesis.

I would also like to thank my secondary supervisor Assistant Professor Dr. Yuji Ohishi, who inspired and guided me through my PhD research. I am deeply grateful for countless discussions he had with me with patience. He taught me how to apply what I have learned to explore and understand the unknown world; he educated me how to think deeply from the fundamentals of materials science and capture the physical picture behind the observations. By writing scientific papers with him, I learned from him on the way of structuralizing the content in an academic style and his rigorousness is highly respected. I'll always keep in mind that "simple is best".

I am truly thankful for Professor Dr. Shinsuke Yamanaka, who is previous supervisor. He persuasively conveyed an interest in my work, and I am grateful for my inclusion in his research group.

I am thankful to Dr. Guanghe Li, Dr. Sungho Choi, Dr. Masaya Kumagai, Mr. Jungmin Kim, and Mr. Xie Jun for kind discussion and support of experiment.

I would especially like to thank to Mr. Yusuke Mitazono, who was my research partner. He was help to my start in the lab. We had a discussion about solving the research or academic problem about thermal transport of materials as well as $La_2Mo_2O_9$. Without his help, I would not have complete my PhD.

My thankfulness is also extended to all members in the Yamanaka Laboratory for their helpful advice and encouragement in the life of a Ph.D. student.

My deep gratitude goes to my parents, Yangpyo Ok and Myungsuk Kim. They give me never-ending care and understanding, while leaving me with great freedom of achieving my dreams. Without their love, I could not have gone so far.

At the end I would like to express appreciation to my beloved future wife Sihyun Kim who was always my support in the moments when where was no one to answer my queries. Without any doubt, I dedicate this thesis to my family.

February 2018

KyungMin Ok